NON-DESTRUCTIVE EXAMINATION OF STONE MASONRY HISTORIC STRUCTURES – QUANTITATIVE IR THERMOGRAPHY AND ULTRASONIC TESTING

A THESIS SUBMITTED TO
THE GRADUATE SCHOOL OF NATURAL AND APPLIED SCIENCES
OF
MIDDLE EAST TECHNICAL UNIVERSITY

BY

SELEN AKEVREN

IN PARTIAL FULFILLMENT OF THE REQUIREMENTS
FOR
THE DEGREE OF MASTER OF SCIENCE
IN
BUILDING SCIENCE
IN
ARCHITECTURE

FEBRUARY 2010

Approval of the thesis:

NON-DESTRUCTIVE EXAMINATION OF STONE MASONRY HISTORIC STRUCTURES – QUANTITATIVE IR THERMOGRAPHY AND ULTRASONIC TESTING

submitted by **SELEN AKEVREN** in partial fulfillment of the requirements for the degree of **Master of Science in Architecture Department, Middle East Technical University** by,

Prof. Dr. Canan Özgen _____
Dean, Graduate School of **Natural and Applied Sciences**

Assoc. Prof. Dr. Güven Arif Sargın _____
Head of Department, **Architecture**

Asst. Prof. Dr. Ayşe Tavukçuoğlu _____
Supervisor, **Architecture Dept., METU**

Examining Committee Members:

Prof. Dr. Emine N. Caner Saltık _____
Architecture Dept., METU

Asst. Prof. Dr. Ayşe Tavukçuoğlu _____
Architecture Dept., METU

Assoc. Prof. Dr. Arda Düzgüneş _____
Architecture Dept.,METU

Levent Tosun, M.Sc. _____
Architecture Dept., METU

Assoc. Prof. Dr. İsmail Özgür Yaman _____
Civil Engineering Dept., METU

Date: February, 5th 2010

I hereby declare that all information in this document has been obtained and presented in accordance with academic rules and ethical conduct. I also declare that, as required by these rules and conduct, I have fully cited and referenced all material and results that are not original to this work.

Name, Last Name: Selen Akevren

Signature :

ABSTRACT

NON-DESTRUCTIVE EXAMINATION OF STONE MASONRY HISTORIC STRUCTURES – QUANTITATIVE IR THERMOGRAPHY AND ULTRASONIC TESTING

Akevren, Selen

M.Sc., Department of Architecture, in Building Science

Supervisor: Asst. Prof. Dr. Ayşe Tavukçuoğlu

February 2010, 126 pages

The *in-situ* examination of historical structures for diagnostic and monitoring purposes is a troublesome work that necessitates the use of non-destructive investigation (NDT) techniques. The methods of quantitative infrared thermography (QIRT) and ultrasonic testing have distinct importance in this regard. The key concern of the study was developing the *in-situ* use of QIRT for assessment of stone masonry wall sections having different sublayer(s) and failures. For that purpose, the non-destructive *in-situ* survey composed of QIRT and ultrasonic testing was conducted on a 16^{th} century monument, Cenabi Ahmet Paşa Camisi, suffering from structural cracks, dampness problems and materials deterioration. The combined use of these two methods allowed to define the thermal inertia characteristics of structural cracks in relation to their depth. The temperature evolution in time during the controlled heating and cooling process was deployed for the cracks/defects inspection. The superficial and deep cracks were found to have different thermal responses to exposed conditions which made them easily distinguishable by QIRT analyses. The depth of cracks was precisely estimated by the *in-situ* ultrasonic testing data taken in the indirect transmission

mode. The inherently good thermal resistivity of the wall structure was found to have failed due to entrapped moisture resulting from incompatible recent plaster repairs. The IRT survey allowed to detect the wall surfaces with different sublayer configurations due to their different thermal inertia characteristics. The knowledge and experience gained on the experimental set-ups and analytic methods were useful for the improvement of *in-situ* applications of QIRT and ultrasonic testing.

Keywords: Quantitative IR Thermography, Ultrasonic Testing, Thermal Inertia Characteristics, Non-destructive Defect Analysis, Stone Masonry Historic Structures

ÖZ

TARİHİ TAŞ YAPILARIN TAHRİBATSIZ YÖNTEMLERLE İNCELENMESİ: NİCEL KIZILÖTESİ ISIL GÖRÜNTÜLEME VE ULTRASONİK MUAYENE

Akevren, Selen

Yüksek Lisans, Mimarlık Bölümü, Yapı Bilimleri

Tez Yöneticisi: Yrd. Doç. Dr. Ayşe Tavukçuoğlu

Şubat 2010, 126 sayfa

Tarihi yapıların yerinde/arazi ortamında muayenesi ve takibi, kapsamlı birçok çalışmayı gerektirir. Bu çalışmalarda kızılötesi ısıl görüntüleme ve ultrasonik muayene gibi tahribatsız yöntemlerin kullanılması tercih edilmelidir. Çalışmanın ana amacı, kızılötesi ısıl görüntülemenin arazi ortamında kullanımını geliştirmek; birçok katmandan oluşan tarihi taş duvarlardaki sorunların yapıya zarar vermeden ayrıntılı biçimde incelenmesini mümkün kılmaktır. Bu amaçla, yapısal çatlaklar, nem problemleri ve malzeme bozulmaları gibi önemli sorunları olan Cenabi Ahmet Paşa Camisi (16yy, Ankara), kızılötesi ısıl görüntüleme ve ultrasonik muayene yöntemlerinden oluşan tahribatsız bir arazi çalışması ile incelenmiştir. Kızıl ötesi ısıl görüntüleme ile ultrasonik muayene yöntemlerinin ortak kullanımı, farklı derinliklerdeki yapısal çatlakların belirleyici/ayırıcı ısıl niteliklerini keşfetmeye imkan vermiştir. Duvar yüzeyleri ve bu duvarlarda mevcut olan çatlaklar/bozulmalar, peşpeşe çekilen ısıl görüntüler ile analiz edilmiş; ortamın ısınması ve soğuması ile birlikte yüzey sıcaklıklarındaki değişimler zamana bağlı olarak takip edilmiştir. Farklı derinliklerdeki çatlakların, ısınma ve soğuma koşullarıyla dengeye gelme hızları arasında farklılıklar bulunmuş; kızıl ötesi ısıl görüntüleme ile farklı derinliklerdeki çatlakların ayırt edilebileceği anlaşılmıştır.

Kagir yapıdaki derin çatlakların gerçek derinlikleri/uzantıları, duvar yüzeyine paralel alınan ultrasonik hız ölçümleriyle belirlenmiştir. Su buharı geçirimsiz sıvalarla yapılan son dönem onarımları, yapı duvarında nem sorununa neden olmuş; aslen iyi ısı yalıtım niteliklerine sahip olan tarihi yapı duvarının ısıl direnci düşmüştür. Kızılötesi ısıl görüntüleme analizleri, farklı ısıl atalet özelliklerine sahip katmanlardan oluşan farklı duvar kesitlerinin belirlenmesine imkan vermektedir. Deney düzenekleri ve analiz yöntemleri üzerine edinilen bilgi ve deneyim, tarihi yapıların yerinde muayenesi ve kontrolü amaçlı kızılötesi ısıl görüntüleme ve ultrasonik muayene yöntemlerinin yaygınlaştırılması ve bu yöntemlerin geliştirilmesi bakımından son derece yararlı olmuştur.

Anahtar Kelimeler: Nicel Kızılötesi Isıl Görüntüleme, Ultrasonik Muayene, Isıl Eylemsizlik Karakteri, Tahribatsız Sorun Analizi, Tarihi Taş Yapılar

To My Family

ACKNOWLEDGMENTS

First of all, I would like to thank my supervisor Asst. Prof. Dr. Ayşe Tavukçuoğlu for her endless support, encouragement, sacrifices and unbelievable effort throughout the study.

I am thankful to Dr. Ermanno Grinzato at Consiglio Nazionale delle Ricerche, CNR-ITC (Italy), for his advices and suggestions throughout the investigation and analyses. I would also like to thank Prof. Dr. Emine N. Caner-Saltık, the head of the Materials Conservation Laboratory at METU Department of Architecture, for her encouragement and support during the study.

I am also grateful to Mete, Şenay and Duygu, the project assistants of the Materials Conservation Laboratory for their support during the *in-situ* study.

I would also like to thank the General Directorate of Pious Foundations (Vakıflar Genel Müdürlüğü) for permission to use the measured drawings of Cenabi Ahmet Paşa Camisi as well as written documents about the structure and to the SAYKA Mimarlık Company and its manager, Conservation Architect Mrs. Saadet Sayın, for their assistance during the *in-situ* survey and literature supply.

I am also grateful to my department manager Mrs. Bilge Küçük for overlooking to my endless studies during working hours and to my colleagues for their tolerance in this respect.

Lastly, although this is not enough to define my feelings and thanks to them, I would like to thank my family: my parents, Sevgi and Ahmet, my sister Ece and my fiancé Serkan for their emotional and loving support during my study as well as throughout my life.

TABLE OF CONTENTS

LIST OF TABLES

TABLES

LIST OF FIGURES

FIGURES

LIST OF ABBREVIATIONS

NDT	Non-Destructive Testing
QIRT	Quantitative Infrared Thermography
IRT	Infrared Thermography
IR	Infrared
UPV	Ultrasonic Pulse Velocity
I	Thermal inertia
e	Thermal effusivity, W $s^{-1/2}m^{-2}K^{-1}$
T	Temperature, ˚C
ρ	Density, kg m^{-3}
$ø$	Porosity, %
c	Specific heat, J $kg^{-1}K^{-1}$
VHC	Volumetric Heat Capacity, J $m^{-3}K^{-1}$
k	Thermal conductivity, W $m^{-1}K^{-1}$
ε	Emissivity
α	Thermal diffusivity, m^2 s^{-1}
R	Thermal resistance, m^2K W^{-1}
R_T	Total thermal resistance, m^2K W^{-1}
R_{si}	Inside surface thermal resistance, m^2K W^{-1}
R_{so}	Outside surface thermal resistance, m^2K W^{-1}
l	Thickness, m
U	Thermal transmittance, W $m^{-2}K^{-1}$
MoE	Modulus of elasticity
µm	Micrometer
kW	Kilowatt
PT	Pulse Thermography
LT	Lock-in Thermography
MT	Modulated lock-in Thermography
PPT	Pulse Phase Thermography

ΔT	Temperature difference, °C
R_W	Rate of warming up
R_C	Rate of cooling down
R^2	Correlation coefficient

CHAPTER 1

INTRODUCTION

In this chapter are presented the argument and objectives of the study on which the thesis is based. A brief overview of procedure is followed by a section describing the disposition of the remaining chapters.

1.1 Argument

Historical structures are valuable documents that present the achievements of the past in terms of architectural, constructional technologies and functional systems. It is essential to keep their authenticity and to provide their survival for posterity. This requires comprehensive studies for their maintenance and conservation, to be done by a multidisciplinary team including conservation architects, engineers, scientists, specialists, *etc*.

Many historical buildings are suffering from serious problems; such as moisture, thermal, structural failures in the exposed weathering conditions. These problems affect the health of historic structures and their materials. The correct diagnosis of the problems and their reasons is therefore important to eliminate, or at least to minimize the damaging effects of the weathering conditions. In other words, the diagnostic studies have vital importance to define the problems and then to establish programs for maintenance and conservation purposes. Here, the use of non-destructive investigation techniques is significant for such diagnostic studies, especially for *in-situ* surveys.

In-situ examination of historical structures is a troublesome work that necessitates the use of non-destructive investigation (NDT) techniques. Such methods allow evaluation of existing condition for building materials without any destructive and intrusive effect upon the building itself (Meola, Carlomagno and Giorleo, 2004; Maldague, 2001). The use of quantitative infrared thermography (QIRT) together with ultrasonic pulse velocity (UPV) measurements has a distinct importance in that regard. These methods allow the evaluation and monitoring of historical structures in relation to materials failure, thermal and moisture problems, cracks and compatibility of recent interventions while the buildings themselves remain intact (Grinzato, Bressan, Marinetti, Bonacina and Bison, 2002b; Grinzato, Marinetti, Bison and Concas, 2004; Kandemir Yucel, Tavukçuoğlu and Saltık, 2007; Tavukçuoğlu, Cicek and Grinzato, 2008; Grinzato, Cadelano, Bison and Petracca, 2009).Comprehensive studies are, therefore, needed to improve those NDT methods for the *in-situ* evaluations, to train specialists and to make its use widespread in historic structures.

Wall sections having different sublayer(s), moisture content and defects, such as material failures and cracks, are expected to exhibit different thermal inertia characteristics during heating/cooling conditions (Tavukçuoğlu, *et al*., 2008; Grinzato, Bison and Marinetti, 2002a; Maierhofer, Brink, Röllig and Wiggenhauser, 2002; Wiggenhauser, 2002; Maldague, 2001; Titman, 2001). Such characteristics can be precisely and practically measured by QIRT, by processing surface temperature data to find out the warming up/cooling down rate of the target area as a function of time. The increase or decrease in those rates under the same climatic conditions should be due to changes in materials and/or wall section capacity to absorb and/or release heat. In other words, how easily heat can be absorbed or released by the wall surface. This study is focused on establishing a technique by using that information, which can only be achieved by QIRT, for the *in-situ* thermal monitoring of wall surfaces.

Cracks are one of the common defects observed in masonry structures, having a certain structural significance since some of them may be an indication of instability of the structure. Some others may have a little effect on the stability while

accelerating the degree of weathering factors since they cause thermal bridge, moisture and air leakages. It is a necessity to examine the cracks in terms of direction, extent, width, depth, and alignment for a period in order to find out whether they are stable or altering in size (active) and to discover their main reason(s) (Sowden, 1990; Eldridge, 1976). The *in-situ* monitoring of the cracks should be done preferably by NDT methods, such as ultrasonic testing and QIRT. There are some studies using ultrasonic testing method for the assessment of cracks, especially on the estimation of depth of a crack, in stone masonry structures (Christaras, 1999; Kahraman, Soylemez and Fener, 2008). The number of studies on the assessment of cracks by infrared imaging remains, however, rather limited (Grinzato, *et. al*. 2009). There is need of more comprehensive studies dealing with the quantitative assessment of structural cracks in terms of depth and activeness, by the joint use of IRT and ultrasonic testing. Therefore, the potentials and limits of those methods should be well-understood for the *in-situ* assessment of structural crack(s) in terms of thermal behaviour and ultrasonic characteristics.

A non-destructive study is conducted on the 16th century Ottoman mosque, Cenabi Ahmet Paşa Camisi (mosque) located in Ankara. It is unique stone masonry structure built by Mimar Sinan; a well-known architect of period (Boztepe, 1987; Başkan, 1993). It still keeps its original architecture and building technologies, reflecting the achievements of the past. It is now suffering from structural cracks occurred in recent years (Çetin and Canbay, 2008), dampness problems and material deteriorations. The correct diagnosis of its problem(s) is essential to keep healthy boundary conditions for the structure itself and its historic materials, in other words, for its survival. Considering all above, that structure was selected as the case study to be examined by *in-situ* QIRT and ultrasonic testing.

1.2 Objectives

There is the lack of knowledge and experience on the *in-situ* applications of quantitative infrared thermography for building diagnostics. This study involves the *in-situ* examinations for a stone masonry historic structure. In this regard, this study was expected to presenting the studies basically in terms of establishing experimental set-ups on site and analytic methods for the quantitative analysis of *in-situ* infrared and ultrasonic data.

The particular objectives of the study were to improve the *in-situ* use of quantitative infrared thermography and ultrasonic testing for diagnostic and monitoring studies, with an emphasis on:-

- the assessment of structural cracks at a stone masonry structure in terms of depth and activeness and the identification of the thermal inertia characteristics of cracks in relation to the depth and moisture content;
- compatibility assessment of plaster repairs at a historic stone masonry structure in relation to the moisture and thermal failures;
- identification of historic wall painting layer and presence of historic plaster layer(s) hidden behind the fine coats recently done;
- the determination of thermal inertia characteristics for the stones in relation to dampness problems.

The experiences achieved during the *in-situ* studies were evaluated in terms of potentials and restrictions of QIRT and ultrasonic testing methods as well as the contribution of their joint-use. It was expected that this knowledge would be useful for the improvement of *in-situ* surveys.

In brief, the Cenabi Ahmet Paşa Camisi, which suffers from serious problems, such as structural cracks, thermal and moisture problems and improper recent repairs, was examined to achieve the knowledge and experience based on the objectives mentioned above. This study was expected to share that information in order to

improve the conscious use of infrared thermography for the diagnostic and monitoring studies in the field of conservation and to establish a base for the training of the prospective specialists/researchers interested in quantitative infrared thermography.

1.3 Procedure

The study was carried out in three steps. As a first phase, introductory information about the mosque was gathered; the present condition of the mosque was observed *in-situ*, a literature survey about the structure, its history, interventions underwent in time *etc*. was carried out; measured drawings and written documents about the examined mosque were accessed from the General Directorate of Pious Foundations. The literature review was extended to cover methodology to understand the working principles of these techniques for the analyses of data collected *in-situ*.

Then after the evaluation of the collected information, *in-situ* studies were continued for 18 months. During these studies, three different NDT methods, IRT, ultrasonic testing and mapping of visual decay forms were used on the selected areas of structure. The data of ambient temperature and relative humidity were also collected throughout the study period by data loggers placed at four directions of monument in both interiors and exteriors.

Finally, the data collected *in-situ* were analysed to obtain the results. For IRT analyses, professional programs were used and the data was interpreted together with the graphs that were built up in the M.S. Office Excel program. Ultrasonic testing data was also converted to the graphs to be discussed. Moreover, maps of visual decay forms were prepared to support the other NDT methods. All results were evaluated together to determine the condition of structure.

1.4 Disposition

The study is presented in five chapters, of which this introduction is the first.

In the second chapter, literature survey is given on the thermo-physical and physico-mechanical properties of building materials that are the basic principles of NDT methods used during the study. It continues with the description of infrared thermography and ultrasonic testing; their application areas, general principles, their types and the usage of methods for the assessment of building failures together with the mapping of visual decay forms. General information is also given about the examined historic masonry structure.

The material of the study, Cenabi Ahmet Paşa Camisi is described in more detail in the third chapter, including its present condition and the problems affect the building. The non-destructive methods conducted on Cenabi Ahmet Paşa Camisi are also presented in this chapter.

In the fourth chapter, the results obtained from *in-situ* studies are compiled and presented with relevant figures, charts, tables and drawings.

These results are discussed in the fifth chapter. They are evaluated in terms of assessment of structural cracks, compatibility assessment of recent repairs, identification of historic wall painting layer and assessment of historic plaster layers hidden behind the recent repairs, thermal inertia characteristics of stones in relation to dampness problems and evaluation of non-destructive investigation methods used *in-situ*. Chapter ends with a conclusion about the study as a whole and suggestions on further research.

CHAPTER 2

LITERATURE REVIEW

This chapter covers reports in the literature directly or indirectly concerning the study owing to their diversity, these have been compiled under six subheadings as below:

- thermo-physical properties of materials establishing their thermal inertia characteristics; and some basic thermo-physical properties of building materials used in masonry structures;
- physico-mechanical properties of materials and their relation with ultrasonic values;
- use of quantitative infrared thermography for failure assessment;
- use of ultrasonic testing method for failure assessment;
- mapping of visual decay forms; and
- descriptive information on the case study: Cenabi Ahmet Paşa Camisi.

2.1 Thermo-Physical Properties of Materials Establishing Their Thermal Inertia Characteristics

Here, some basic thermo-physical parameters of materials, such as density, porosity thermal conductivity, thermal diffusivity, thermal effusivity, specific heat, *etc*, were explained in few sentences and their relation/contribution to the thermal inertia and thermal insulation characteristics of building materials were discussed. These are significant parameters for the detection of thermal failures during the infrared thermography examinations.

Thermo-physical properties are characteristics that control the diurnal, seasonal, or climatic surface and subsurface temperature variations (or thermal curves) of a material (http://en.wikipedia.org/wiki/Thermophysics). The most important thermo-physical property is "thermal inertia", which is a bulk material property related to thermal conductivity and volumetric heat capacity (http://en.wikipedia.org/wiki). It is also a measure of the thermal mass and the velocity of the thermal wave which controls the surface temperature of a material. Under the exposed diurnal temperature variations (or thermal curves), the surface temperature of a material with low thermal inertia changes significantly during the day, while the surface temperature of a material with high thermal inertia does not change rapidly (http://en.wikipedia.org/wiki/Volumetric_heat_capacity; Maldague, 2001; Goulart, 2004). In other words, a higher value of the volumetric heat capacity means a longer time for the system to reach equilibrium. The thermal inertia of a material (I) is defined as the square root of the product of the material's bulk thermal conductivity and volumetric heat capacity, where the latter is the product of density and specific heat capacity (http://en.wikipedia.org/wiki/Volumetric_heat_capacity; Maldague, 2001: 333):

$$I = (k\rho c)^{1/2} \tag{1}$$

where, k is the thermal conductivity (W $m^{-1}K^{-1}$), ρ is the density (kg m^3) and c is the specific heat (J $kg^{-1}K^{-1}$).

In infrared thermography applications, deriving and understanding the thermal inertia of the surface can help to characterize the building materials and to examine some features of their surfaces (Grinzato, Vavilov and Kauppinen, 1998; Avdelidis and Moropoulou, 2003b, Balaras and Argiriou, 2002).

Thermal effusivity (e) of a material is a measure of its ability to exchange thermal energy with its surroundings (http://en.wikipedia.org/wiki/Thermal_effusivity). It defines the capacity of materials to absorb and/or release heat; in other words, how

much heat can be absorbed or released by the material (Goulart, 2004). In thermodynamics, the thermal effusivity of a material is defined as the square root of the product of the material's thermal conductivity and its volumetric heat capacity, which is the same formula defined for the measure of thermal inertia. It is expressed in $W\ s^{-1/2}m^{-2}K^{-1}$ (Goulart, 2004). The higher thermal conductivity and specific heat storage capacity signal the higher effusivity (Goulart, 2004). If two semi-infinite bodies initially at temperatures T_1 and T_2 are brought in perfect thermal contact, the temperature at the contact surface T_m will be calculated by using the initial temperatures of bodies and their relative effusivities as shown in the following Equation (2) (http://en.wikipedia.org/wiki/Thermal_effusivity):

$$T_m = T_1 + (T_2 - T_1)\frac{e_2}{(e_2 + e_1)} \tag{2}$$

where, T_1 is the initial temperature of semi-infinite body, T_2 is the initial temperature of another semi-infinite body, e_1 is the effusivity of semi-infinite body, e_2 is the effusivity of another semi-infinite body.

The Wikipedia Encyclopedia (2010) defines thermal mass, sometimes known as the thermal flywheel effect, is a concept that provides "inertia" against temperature fluctuations. It is also called as thermal capacitance or heat capacity, which defined as the capacity of a body to store heat. When outside temperatures are fluctuating throughout the day, a large thermal mass within the insulated portion of a house can serve to flatten out the daily temperature fluctuations, since the thermal mass will absorb heat when they are hotter than the mass, and give heat back when the surroundings get cooler. If the body consists of a homogeneous material, the thermal mass is simply the mass of material times the specific heat capacity of that material. It is typically measured in units of $J°C^{-1}$ or $J\ K^{-1}$. Heat capacities for bodies made of many materials can be calculated by the sum of heat capacities for their pure components. The properties required for good thermal mass are high specific heat capacity and high density.

The parameters of **time lag** and **decrement** are in relation with the thermal inertia (Ropelewski and Neufeld, 1999). As authors explain, time lag is the time difference between the exterior and interior wall surfaces to reach the peak temperature. When the wall is heated from one side, the other side of wall becomes warmer with a time lag. Decrement means the relative decrease in fluctuation of the interior surface temperature with time. These parameters are different for each material type because of their different thermal inertia characteristics and they depend upon a complex interaction between the density, specific heat, thermal conductivity and thickness of building materials.

Thermal inertia characterisations are mainly defined with three thermo-physical parameters which are density, specific heat and thermal conductivity. Therefore, thermal inertia of a material should be evaluated by considering those parameters. For the higher heat storage capacity, the materials should have high density, high thermal capacity and also high thermal conductivity (Goulart, 2004).

Density (ρ) is the mass of material for a unit volume, expressed in kg m^{-3} (Hens, 2007: 111). There is an inverse proportion between the density and thermal performance; material with high density has also high thermal conductivity which means poor thermal resistance (Goulart, 2004). Density can be calculated by using the Equation (3) given below (http://en.wikipedia.org):

$$\rho = \frac{e^2}{kc} \tag{3}$$

where, e is the thermal effusivity (W $s^{-1/2}m^{-2}K^{-1}$), k is the thermal conductivity (W $m^{-1}K^{-1}$) and c is the specific heat (J $kg^{-1}K^{-1}$).

Porosity ($\varnothing$) is the ratio of the pore volume to the volume of mass and expressed by the percentage of volume (Hens, 2007: 112; Maldague, 2001: 240). Generally, materials with high porosity have less dense and also have lower thermal conductivity (Özkahraman, *et al*., 2004) which means that they can behave as a

thermal insulation material; in addition to that, size of pores is a significant factor since bigger pores conduct more heat (Singh, Sinha and Singh, 2007).

Specific heat (*c*) represents the amount of heat that is necessary to increase the temperature of a unit quantity of a substance by one unit, expressed in J $kg^{-1}K^{-1}$ (http://en.wikipedia.org). In particular phase, specific heat capacity is constant for any substance (Goulart, 2004). Specific heat can be calculated by using the Equation (4) given below (http://en.wikipedia.org):

$$c = \frac{e^2}{k\rho} \tag{4}$$

where, *e* is the thermal effusivity (W $s^{-1/2}m^{-2}K^{-1}$), *k* is the thermal conductivity (W $m^{-1}K^{-1}$) and ρ is the density (kg m^3).

Volumetric heat capacity (*VHC*) is defined in Wikipedia Encyclopedia (2010) as the ability of a given volume of a substance to store internal energy without a phase change while undergoing a given temperature change. The difference of volumetric heat capacity and specific heat capacity is that, *VHC* depends on the volume of the material, while the specific heat is based on the mass of the material (http://en.wikipedia.org). *VHC* is found by multiplying the specific heat by the density of the substance (http://en.wikipedia.org; Goulart, 2004) as shown in Equation (5):

$$VHC = c\rho \tag{5}$$

where, *c* is the specific heat (J $kg^{-1}K^{-1}$) and ρ is the density (kg m^3).

Thermal conductivity (*k*) is the rate of heat flow passing through a unit area of a homogeneous material having a unit thickness when temperature difference is occurred between two sides of material, expressed in W $m^{-1}K^{-1}$ (Goulart, 2004;

Maldague, 2001: 238; Hall, v.1, 1994: 29; Strother and Turner, 1990: 4). Thermal conductivity of good thermal insulators are lower than 1 Wm^oC^{-1}, while the materials having thermal conductivity greater than 100 Wm^oC^{-1} are considered as good thermal conductors (Maldague, 2001: 43). Therefore, when compared with metals, building materials like stone, brick or mortar have low thermal conductivity which results in a slow response to temperature changes (Wiggenhauser, 2002). Materials with high density have high thermal conductivity which improves the heat storage capacity of materials (Singh, *et al*., 2007; Goulart, 2004; Özkahraman, Selver and Işık, 2004). Thermal conductivity is calculated by using the Equation (6) given below (Grinzato, Bison, Marinetti and Vavilov, 1994):

$$k = \frac{e^2}{c\rho} \tag{6}$$

where, e is the thermal effusivity ($W\ s^{-1/2}m^{-2}K^{-1}$), c is the specific heat ($J\ kg^{-1}K^{-1}$) and ρ is the density ($kg\ m^3$).

Emissivity (ε) is the ability of examined material to emit energy from its surface (Avdelidis and Moropoulou, 2003b). Emissivity value for a material is obtained by the ratio of radiant energy emitted from the surface of material to the energy emitted by blackbody at a given temperature (Goulart, 2004; Maldague, 2001: 31; Hall, v.1, 1994: 30). Emissivity is a significant property for thermographic surveys since infrared camera detects the radiation emitted by material surface (Avdelidis, *et al*., 2003b; Balaras and Argiriou, 2002). It is a unitless quantity with variation between the values zero and one. The number of zero is the value for perfect reflector material which is mirror while blackbody is perfect emitter with the emissivity value of one (http://www.websters-online-dictionary.org). Avdelidis, *et al*. (2003b) and Balaras, *et al*. (2002) emphasize the emissivity values of different materials and the factors affecting the emissivity of materials. As the authors note that building materials such as stone, concrete or plaster have high emissivity values, they are usually higher than 0.8, whereas polished metal surfaces have lower emissivity values, that is less than 0.5, therefore metals act as a mirror and radiant energy is not emitted efficiently, so it

is difficult to measure temperatures of metallic surfaces. Investigated materials can exhibit different emissivity values according to the temperature, the wavelength as well as their texture and composition (whether they are polished, metallic, non-metallic or not).

Thermal diffusivity (α) is the ratio between thermal conductivity and the volumetric heat capacity, expressed in $m^2 s^{-1}$ (Goulart, 2004; Strother and Turner, 1990: 247). It also designates how easily a material undergoes the variations in temperature and how rapidly heat flows within the structure. It defines the way of transmitted heat from surface to the material section (Goulart, 2004), that is why it affects the surface temperature (Bray and McBride, 1992: 629) and this feature makes diffusivity a good indicator for the decay of materials (Grinzato, Bison and Marinetti, 2002a; Bison, Marinetti, Mazzoldi and Bressan, 2002). Higher thermal diffusivity provides lower thermal gradient at the surface of materials (Bray, *et al*., 1992: 629). Additionally, the materials with high thermal conductivity and low heat storage capacity have high thermal diffusivity (Goulart, 2004) as shown in the Equation (7) given below (Strother and Turner, 1990: 247; Goulart, 2004; Grinzato, *et al*., 2002a; http://en.wikipedia.org):

$$\alpha = \frac{k}{c\rho} \tag{7}$$

where, k is the thermal conductivity ($W\ m^{-1}K^{-1}$), c is the specific heat ($J\ kg^{-1}K^{-1}$) and ρ is the density ($kg\ m^3$).

Thermal resistance (R) is the property of material or air that resists the heat transfer, expressed in $m^2K\ W^{-1}$ (Goulart, 2004; Strother and Turner, 1990: 291). There is an inverse proportion between thermal conductivity and thermal resistivity, but on the contrary a direct proportion is seen between thermal resistivity and material thickness; in other words, if the thickness of material is larger and the heat flow is lower, thermal resistivity will be higher (Goulart, 2004; Hall, v.1, 1994: 29). Thermal

resistance can be calculated by using the Equation (8) given below (TS 825, 2008; Hall, v.1, 1994: 29; Strother and Turner, 1990: 291):

$$R = \frac{l}{k} \tag{8}$$

where, l is thickness of material (m) and k is the thermal conductivity (W $m^{-1}K^{-1}$).

Total thermal resistance (R_T) is the sum of individual thermal resistances for the materials in building section as well as interior and exterior air layers adjacent to the surfaces (TS 825, 2008; TS EN ISO 6946, 2007; Goulart, 2004; Hens, 2007; Strother and Turner, 1990). It is calculated by using the Equation (9) given below (TS 825, 2008; TS EN ISO 6946, 2007):

$$R_T = R_{si} + R_1 + R_2 + ... + R_n + R_{so} \tag{9}$$

where, R_{si} is the inside surface thermal resistance ($m^2K\ W^{-1}$), R_1, R_2, R_n are the thermal resistance of structural component ($m^2K\ W^{-1}$) and R_{so} is the outside surface thermal resistance ($m^2K\ W^{-1}$).

Thermal transmittance (U) is the rate of heat flow through a building component and it is the reciprocal of total thermal resistance ($1/R_T$) which is expressed by W $m^{-2}K^{-1}$ (Goulart, 2004; Hens, 2007; Strother and Turner, 1990). In fact, thermal transmittance is a measure to identify insulation quality of investigated material, because smaller U value means that heat flow is less through the material, so better insulation is provided (Hens, 2007: 82). Acceptable U value for the walls given in TS 825 (2008) for quality construction of buildings situated in Ankara is 0.50 W $m^{-2}K^{-1}$. This value was used to understand the thermal insulation characteristics of assumed tuff masonry wall sections given in Appendix C.

The thermal transmittance, *U* value, through the wall, roof or floor section at steady state conditions is calculated by using the Equation (10) given below (TS 825, 2008; Hall, v.1, v.3, 1994; TS EN 1745, 2004; TS EN ISO 6946, 2007):

$$U = \frac{1}{R_{si} + \frac{l_1}{k_1} + ... + \frac{l_n}{k_n} + R_{so}} \tag{10}$$

where, R_{si} is the inside surface thermal resistance (m^2 K W^{-1}), R_{so} is the outside surface thermal resistance (m^2 K W^{-1}), l_n is the thickness of materials (m), k_n is the thermal conductivity of materials (W $m^{-1}K^{-1}$).

Thermo-physical properties of some building materials are compared with each other under the subheading given below:

Thermo-Physical Properties of Building Materials Used in Masonry Structures

The data on basic physical and thermal properties of building stones and contemporary masonry materials, obtained from literature, were summarized in Table 2.1, in order to better understand their thermal insulation characteristics and their contribution to the overall thermal performance of structures. The tuff and andesite stones, the construction materials of the Cenabi Ahmet Paşa Camisi, were compared with the other masonry materials, such as historic brick and brick mortar forming the historic brick dome structure of 15^{th} century hamam structure and light weight masonry blocks preferred for contemporary wall construction. These materials were chosen for comparison due to their good thermal performance. Porous and less porous stones were also compared with each other in terms of bulk density, effective porosity and thermal conductivity properties.

Erdoğan (1986) studied on the physical properties of different kinds of tuffs in Nevşehir-Ürgüp region and he found that Nevşehir tuffs are the materials having low density, high porosity and low thermal conductivity. Their density, porosity and

thermal conductivity values were in the range of 1080 kg m^{-3} - 1850 kg m^{-3}, 18.38 – 43.16% and 0.28 W $m^{-1}K^{-1}$ - 0.73 W $m^{-1}K^{-1}$, respectively. However, the low thermal conductivity value of tuff stone increases in the presence of moisture which means that tuff loses its desirable thermal properties (Erdoğan, 1986). Thermal expansion coefficients of tuffs are higher than those of other lightweight construction materials (Erdoğan, 1986) which make the tuff more easily decayed under the exposure of thermal variations (Galan, 1991).

The historic brick and brick masonry mortars forming the historic dome structure of a hamam structure had satisfactory thermo-physical characteristics to establish good thermal performance for this particular structure, having very hot and humid indoors (Çiçek, 2009). Tuffs seemed to have similar thermal characteristics with those historic brick and brick mortar.

The aerated concrete masonry blocks have thermal conductivity values in the range of 0.15 W $m^{-1}K^{-1}$ and 0.23 W $m^{-1}K^{-1}$ (Andolsun, 2006). Tuffs seemed to be denser and more thermal conductive than aerated concrete blocks. However, tuffs seemed to have similar thermal conductivity values with the hand-made and factory bricks used in contemporary structures due to their good thermal performance (TS 825, 2008).

The tuffs have thermal conductivity values in the range of 0.28 W $m^{-1}K^{-1}$ and 0.73 W $m^{-1}K^{-1}$ while the travertine, limestone, granite, marble and sandstone, being less porous than tuffs, have the thermal conductivity values 1.60, 2.70, 2.79, 2.80 and 2.90 W $m^{-1}K^{-1}$, respectively (Table 2.1). When compared with the less porous stones, the tuffs seemed to have inherently good thermal insulation characteristics due to their highly porous and low thermal conductivity values and contribute to the overall thermal performance of masonry walls (Özkahraman and Bolattürk, 2006).

Andesite seems to differ than the other less porous stones, cited in Table 2.1. Although being dense, it seems to be more porous and less thermal conductive than travertine, limestone, granite, marble and sandstone, which may contribute to the overall thermal performance of historic masonry walls.

Table 2.1 The bulk density, porosity and thermal conductivity values of different building materials and the sources from which the values were cited.

Material	**Bulk density, ρ kg m^{-3}**	**Porosity, $ø$ %**	**Thermal Conductivity, k W m^{-1}K^{-1}**	**Source**
Kavak tuff (Nevşehir, Turkey)	1510	28.46	0.50	Erdoğan, 1986
Karadağ tuff (Nevşehir, Turkey)	1850	18.38	0.73	Erdoğan, 1986
Tuff (Kanto, Japan)	1450	41.32		Matsukura and Hirose, 1999
Tuff (Isparta, Turkey)	1400	40	0.40	Özkahraman and Bolattürk, 2006
Andesite (Kyushu, Japan)	2710	18.29		Matsukura and Hirose, 1999
Andesite	2240	16	0.64	Özkahraman, Selver and Işık, 2004
Andesite (Isparta, Turkey)	2280	7.77		Uğur, Demirdağ and Yavuz, 2010
Historic brick (Yalınayak Bath, Turkey)	1310	47.6	0.56±0.002	Caner Saltık, *et al*., 2005
Historic brick (Çukur Bath, Turkey)	1470	39.8	0.53±0.01	Esen, *et al*., 2004
Historic brick (Hersekzade Paşa Bath, Turkey)	1520	38.9	0.60±0.04	Caner Saltık, *et al*., 2003
Historic brick mortar (Yahşi Bey Bath, Turkey)	1550	38.1	0.67±0.02	Caner Saltık, *et al*., 2003
Historic brick mortar (Yahşi Bey Bath, Turkey)	1520	38.3	0.50±0.01	Caner Saltık, *et al*., 2003
Autoclaved aerated concrete (G2-infill material)	400	78	0.15	Andolsun, 2006
Autoclaved aerated concrete (G4-load bearing material)	600	69	0.23	Andolsun, 2006
Contemporary brick	1400		0.58	TS 825, 2008
Contemporary brick	1600		0.68	TS 825, 2008
Contemporary brick	1800		0.81	TS 825, 2008
Travertine (Bucak, Turkey)	2550	2.3	1.60	Özkahraman, Selver and Işık, 2004

Table 2.1 The bulk density, porosity and thermal conductivity values of different building materials and the sources from which the values were cited (continued)

Material	**Bulk density, ρ kg m^{-3}**	**Porosity, $ø$ %**	**Thermal Conductivity, k W m^{-1}K^{-1}**	**Source**
Limestone (Burdur, Turkey)	2690	1.82	2.70	Özkahraman, Selver and Işık, 2004
Granite (Abukuma, Japan)	2670	1.51		Matsukura and Hirose, 1999
Granite (Barre, USA)	2630		2.79	Incropera and Dewitt, 1990
Marble (Halston, USA)	2680		2.80	Incropera and Dewitt, 1990
Marble (Afyon, Turkey)	2702	0.26		Uğur, Demirdağ and Yavuz, 2010
Sandstone (Berea, USA)	2150		2.90	Incropera and Dewitt, 1990
Sandstone (Cerro Coronado, Spain)	2350	13-15		Galan, Carretero and Mayoral, 1999

2.2 Physico-Mechanical Properties of Materials and Their Relation with Ultrasonic Values

There is a relation with the physical, thermal, mechanical properties of materials with ultrasonic velocities. Porosity is inversely proportional with the ultrasonic pulse velocity and uniaxial compressive strength; in other words, if a material has high porosity, its ultrasonic velocity and uniaxial compressive strength will be lower (Sousa, Rio, Calleja, Argandona and Rey, 2005). On the other hand, stones with the same porosity can have different ultrasonic velocity values as well; since the microfracture network inside the material affects the velocity (Sousa, *et al*., 2005). In fact, pores and cracks cause discontinuity in the stone which results in the decreasing of ultrasonic velocity and increasing breakability under compression (Sousa, *et al*., 2005). Apart from porosity, thermal conductivity is in relation with the uniaxial compressive strength, but this time they are directly proportional. Uniaxial compressive strength increases with the increase of thermal conductivity (Singh, *et al*., 2007; Özkahraman, *et al*., 2004).

Modulus of elasticity (*MoE*) is one of the physico-mechanical properties of stones that expresses their deformation ability (Christaras, Auger and Mosse, 1994). According to Christaras, *et al*. (1994), it is obtained from applied axial compressive stresses and resulting axial strains. That property is significant to estimate the elastic response of the material to the stresses that is occurred during the construction or after the construction. *MoE* can be determined by using ultrasonic velocity tests.

2.3 Use of Quantitative Infrared Thermography for Failure Assessment

Infrared thermography (IRT) is a non-contact technique that is produced a map showing the distribution of surface temperature (Meola, *et al*., 2004; Bray and McBride, 1992: 635). It can also be described as a non-destructive and non-invasive measurement technique that measures infrared radiation emitted from surface of material and then produces the thermal image of examined area in colours corresponding to temperature scale (Tavukçuoğlu, Düzgüneş, Caner-Saltık and Demirci, 2005).

Maldague (2001) explains the meaning of thermography as a term. As the author notes *thermography* is the combined use of the words, *thermo* and *graphy*, where *thermo* means surface temperature and *graphy* means the distribution. Thus, infrared thermography is the contact-free technique that measures the temperature distribution on the surface of material.

2.3.1 Fields of use

There is a wide application area of infrared thermography, such as military, industry, architecture, engineering, medicine, meteorology and environment sectors (Titman, 2001; Meola, Maio, Roberti and Carlomagno, 2005). Infrared thermography is used to;

- identify material anomalies (Titman, 2001),
- detect the defects on buildings, like thermal bridges, air leakage, moist areas, heat losses and thermal insulation problems (Ocana, Guerrero and Requena, 2004; Titman, 2001; Moropoulou, Avdelidis, Delegou and Koui, 2001; Grinzato, Vavilov and Kauppinen, 1998),
- identify the surface and subsurface defects (Meola, 2007b),
- detect moisture in porous materials (Meola, 2007b; Moropoulou, *et al*., 2001)
- evaluate the surface treatments applied on historic buildings (Moropoulou, *et al*., 2001),
- control the success of interventions (Titman, 2001; Meola, 2007b),
- test the roof performance (Giovanni and Meola, 2002),
- detect the delaminations of plaster, the presence of wooden framework under plaster (Wiggenhauser, 2002),
- assess the drainage systems (Tavukçuoğlu, *et al*., 2005),
- investigate the sublayers of masonry structures (Sowden, 1990: 68),
- realize different thermal behaviour characteristics of construction materials for historical buildings (Ocana, *et al*., 2004).
- survey the entire building in a short period of time (Balaras and Argiriou, 2002; Bray and McBride, 1992: 643)
- clarify the heating, ventilating, air-conditioning installations (Balaras and Argiriou, 2002),
- identify the problems of electrical and mechanical installations (Balaras and Argiriou, 2002).

As stated, historical structures are one of the application areas of IRT. Monuments are suffering from many problems such as moisture, cracks, different types of material deterioration *etc*. which are occurred in time because of environmental conditions, thermal or mechanical stresses *etc*. At that point, it is significant to detect the defects at an early stage to decrease the effects of it on monument and also to understand the reasons of decays, both of which can be answered by thermographic survey (Giovanni, *et al*., 2002). Thus, IRT is a helpful technique for the maintenance of cultural heritages. Many researches are done by using IRT on monuments. Some

of which are published by Avdelidis and Moropoulou (2003b), Çiçek (2009), Dişli (2008), Grinzato, *et al.* (2004), Grinzato, *et al.* (2002a), Grinzato, *et al.*, (2002b), Grinzato, *et al.* (1998), Kandemir Yucel, *et al.*, (2007), Meola (2007b), Meola, *et al.*, (2005), Tavukçuoğlu, *et al.*, (2008), Tavukçuoğlu, *et al.*, (2005) and Tavukçuoğlu and Caner-Saltık (1999).

Apart from the defect detection, thermography gives possibility to discover the hidden sublayers and/or architectural elements, such as arches, windows, voids, smokestacks, chains, underneath the plaster layer of historical structures (Grinzato, *et al.*, 2002a). These studies are of vital importance to achieve data/knowledge buried within an historic structure while they could not be observed visually (Grinzato, *et al.*, 2002a).

2.3.2 General principles of IRT

Infrared thermography technique turns the emission pattern of an object into a visible image (Meola, *et al*., 2005; Balaras and Argiriou, 2002). Human eye is only able to receive the emissions in the visible wavelength. In the electromagnetic spectrum, infrared radiation is located between visible and microwaves regions; comprising the wavelength from 0.75 to 10 μm (Ocana, *et al*., 2004). Radiation is detected in the 'thermal' part of the infrared spectrum, typically in the 3–5 or 8–14 μm windows which are short and long wavelengths (Ocana, *et al*., 2004; Titman, 2001). Titman (2001) explains the application areas of these wavelengths for thermographic surveys. As author notes, the cameras being sensitive to the short wave band can be effectively-used at indoor surveys and outdoor surveys after the sunset. However, under the solar energy, surveys in shorter wave band can be used only for qualitative evaluations. This is due to the difficulty of these cameras in measuring the real surface temperatures under the solar exposure. When the material is under the solar energy, radiated energy by the material is mixed with the reflected energy. Longer wave band is mostly preferable for outside applications; because it is less affected by

solar reflection (Ocana, *et al*., 2004; Avdelidis, Moropoulou and Theoulakis, 2003a). Long wavelength cameras also work well at ambient temperature and they can detect even the small temperature differences (Ocana, *et al*., 2004).

All materials having temperature above zero emits infrared energy and the temperatures of materials increase according to their absorption capacity of infrared radiation (Ocana, *et al*., 2004 and Avdelidis, *et al*., 2003b). Infrared camera detects the emitted, transmitted and reflected radiation by object into a thermal image with different colours (Figure 2.1). It means that thermographic camera measures the radiation of materials, not the temperatures (Ocana, *et al*., 2004 and Avdelidis, *et al*., 2003b). However, the radiation has a direct relation with the temperature and also emissivity. If the temperature of an object is higher than another, it emits more IR radiation (Balaras and Argiriou, 2002); but it is not forgotten that high reflectance property of the materials with low emissivity causes the mistakes on temperature, because they reflect the solar radiation and they seem warmer than as they are; so to get rid of these mistakes, the survey can be done from different locations of studied object and at different times (Ocana, *et al*., 2004). Another precaution is to use a reference emitter; a material with a known emissivity can be helpful to understand the emissivity values of investigated materials (Avdelidis, *et al*., 2003b). It should be kept in mind that correction of emissivity is necessary to obtain correct temperature data (Avdelidis, *et al*., 2003b). Apart from the emissivity and reflectance, there are other factors that affect the IR measurement; such as ambient temperature, atmospheric particles (gas and vapour molecules or solid particles), wind speed and the distance and angle of camera from the studied object (Balaras, *et al*., 2002). Calibration of the system by simulating real conditions is necessary to include these parameters (Meola, *et al*., 2005).

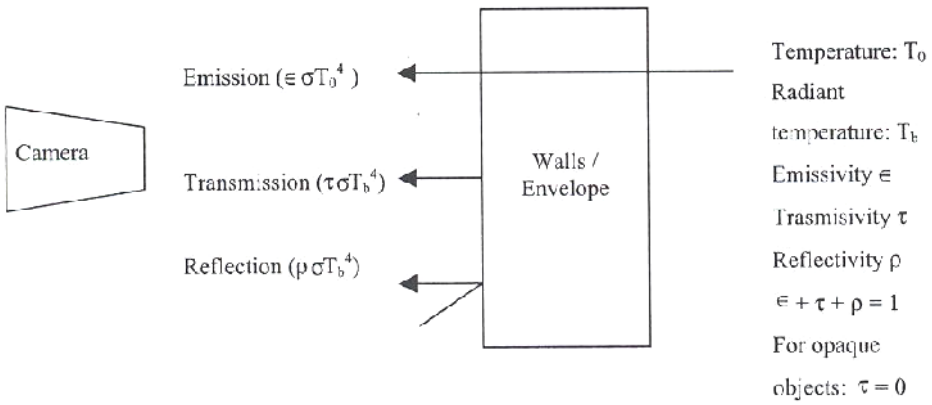

Figure 2.1 Emission, transmission and reflection are the components of radiation detected by infrared camera (Ocana, *et al*., 2004: 516)

In some situations, thermal imaging may not be appropriate. For instance, high winds can limit the outdoor surveys. Wind can reduce the effectiveness of surveys due to surface temperature shear effects (Titman, 2001; Avdelidis, Moropoulou and Theoulakis, 2003a). Likewise, rain may lead to cool the surface, thus masking thermal effects from below the surface; also standing water on roof should be avoided (Titman, 2001). In addition to wind and rain, some materials with good refractory properties, like cladding tile or mosaics hinder thermal transmission through to the substrate, especially in the shorter wave band, and restrict the effectiveness of some building envelope surveys (Titman, 2001). Moreover, Perspex and glass are seen opaque in infrared wavelengths which is important when considering surveying a structure from an adjacent building, from a vehicle or from the air (Titman, 2001).

During the inspection of a building envelope by Using IR thermography, one has to be aware of the physical phenomena taking place and how the outdoor environment interacts with the indoors (Balaras, *et al*., 2002). As Balaras, *et al*. (2002) and Goulart (2004) mention, temperature of external building surfaces increase during the day due to absorption of the incident solar radiation. As a result of the temperature difference between the inner and outer wall surfaces, heat is conducted through the wall. At night, heat is dispersed from the exterior wall surface to the

lower temperature environment by radiation. In order to avoid the temperature increase as a result of the incident solar radiation, IR measurements should be performed at night or during a cloudy day, with low wind speeds to minimise convective heat losses (Balaras, *et al*., 2002; Titman, 2001). After sunset, heating operating in buildings provides thermal gradient between internal and external wall surfaces (Titman, 2001). It is necessary for the heating to be switched on for a few hours prior to the survey to allow a temperature difference to develop through the walls and roof (Titman, 2001). For optimum results, all solar effects should be disappeared and temperature difference between two sides of the wall should have stabilised (Titman, 2001). Such surveys are best carried out between autumn and spring to reduce the solar effects and the evening may be suitable (Titman, 2001). During summer months, study may be done much later, even just before dawn (Titman, 2001). However, in the summer, it is difficult to provide the necessary thermal gradient between inside and outside of the building (Titman, 2001).

Titman (2001) explains three types of conditions that are necessary for thermography to be useful. These conditions are heat/cold source, thermal gradient and induced heating. If a spot temperature difference is observed on the surface of examined area, as a heating or cooling, it designates the location of problematic area. Defects closer to the surface can be detected easily. Moreover, if the thermal gradient through an element of a structure is stabilized and there is no significant fluctuation in thermal conductivity of the materials within the element, the surface temperature over the warm or cool face should be constant. Material omission or local damage within the element, lead to variations in conductivity which causes fluctuations of surface temperature. Induced heating is based on to heat up or cool down the surface to detect the subsurface material anomalies or defects. When the surface is heated up or cooled down, changes in surface temperature depend on the thermal resistance of anomalies, so it becomes possible to differentiate the detection by using surface temperature. Problems like voids or additions cause detectable temperature difference while tight cracks and some additions like grease in epoxy structures do not change the overall thermal characteristics of tested object (Bray and McBride, 1992: 629).

The surface temperature variations on thermal images can be analysed both qualitatively and quantitatively. Qualitative analyses have high level of capability to increase the understanding of examined areas (Magnani and Silva, 2007). But for some cases, quantitative analyses can be necessary; this method can be used to determine the thermo-physical properties of materials (Magnani and Silva, 2007). For quantitative evaluation, many parameters, such as ambient temperature, humidity, distance from target and emissivity become significant; because they are needed to be entered into the software for accurate measurement (Titman, 2001).

2.3.3 Active thermography

Active thermography is based on energy transfer from warmer to cooler areas during warming up or cooling down periods of an examined area (Tavukçuoğlu, *et al*., 2005). During the survey, a heat pulse is applied to the surface and then surface temperature is monitored by infrared camera in heating and/or cooling conditions to analyse the sequential IR images quantitatively (Wiggenhauser, 2002; Maldague, 2001: 343) (Figure 2.2). This technique is suitable for the characterization of nonmetallic materials (Maierhofer, *et al*., 2002) and for the detection of defects in building envelope (Grinzato, *et al*., 1998). Defected area has different thermal behaviour than the sound material during the heating or cooling period because of its different heat capacity or diffusivity which makes it possible to clarify the defects (Grinzato, *et al*., 1998). Homogeneous heating should be applied to the examined surface to avoid false alarms (Grinzato, *et al*., 2002a). Natural heating (solar radiation) or artificial source like halogen lamps can be used for that purpose. Although it can change according to the season and latitude of the survey site; solar heating for a few minutes is enough to heat 2 or 3cm thick plaster layer of a surface (Grinzato, *et al*., 2002a). It is also possible to heat 2cm thick plaster with 4 kW halogen lamps in 10 minutes; but the time, energy and thickness of heated layer depend on the material properties (Grinzato, *et al*., 2002a).

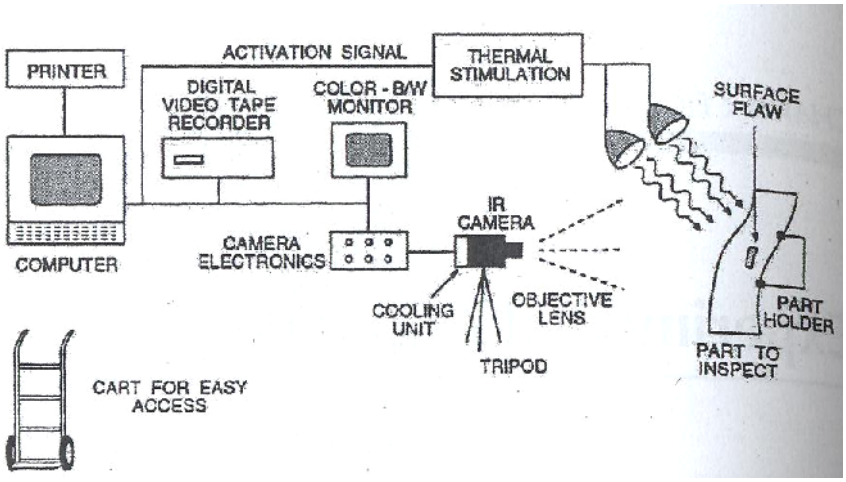

Figure 2.2 Schematic view of experimental setup for active thermography; examined surface is heated while infrared camera recording image and IR images are controlled from the computer (Maldague, 2001: 266)

Under the same heating condition, the defects closer to the surface and/or larger defects reached to the maximum temperature difference quickly (Cheng, Cheng and Chiang, 2008). In general, the IR images provide clear indication of the subsurface defects; but it is difficult to identify the defects having area smaller than 5x5cm and larger cover thickness than 3cm (Cheng, Cheng and Chiang, 2008). Voids can also be detected by active thermography. The shallow voids have enough thermal gradient after short cooling down time while the deeper voids appear after waiting for longer times (Maierhofer, *et al*., 2002). Subsurface deficiencies can be identified clearly during the cooling process of several minutes (Wiggenhauser, 2002); Meola, *et al*., 2005).

Active thermography techniques, which are pulse thermography (PT), lock-in thermography (LT) and pulse phase thermography (PPT) were summarized below:

Pulse thermography is the technique that is performed by monitoring the surface temperature evolution of uniformly heated object during the heating and cooling conditions (Meola, *et al*., 2005; Maldague, 2001; Sakagami and Kubo, 2002). Abnormal behaviour of this temperature indicates subsurface defects (Maldague, 2001). The material temperature changes rapidly after the initial thermal perturbation

since the thermal front propagates, by diffusion, under the surface and also because of radiation and convection losses (Maldague, 2001). The existence of a defect causes reduction of the diffusion rate so that when observing the surface temperature, defects are noticed as areas of different temperatures with respect to surrounding sound area once the thermal front has reached them (Maldague, 2001). Deeper defects will be observed later than the superficial ones with reduced contrast (Meola, *et al*., 2005; Maldague, 2001). There are two different modes of PT which are transmission and reflection (Meola, *et al*., 2005; Giovanni, *et al*., 2002). In transmission mode, infrared camera and heat source are placed opposite sides of examined object, while the reflection mode is the condition that infrared camera and heat source are on the same side of the object (Meola, *et al*., 2005; Giovanni, *et al*., 2002). Generally reflection mode is preferred; because to reach two sides of examined material is not always possible (Meola, *et al*., 2005; Giovanni, *et al*., 2002). However, this heating/cooling approach can be harmful for the valuable frescoes (Giovanni, *et al*., 2002).

Lateral heating thermography is a technique that is applied with a moving heat source to overcome the problem of non-uniform heating (Giovanni, *et al*., 2002). Its distance from the specimen surface, its speed, exposure time as well as its passage number in front of the surface become significant for the evolution of data collected from experiment (Giovanni, *et al*., 2002) .

Lock-in thermography is an active thermography technique where a periodic heat wave is applied to the specific area (Wiggenhauser, 2002). The system collects the IR images for a period and then makes comparison between their temperatures computing amplitude and phase angle of the sinusoidal wave pattern at each point and so the resulting image may be an amplitude image or a phase image (Meola, *et al*., 2005) Depth of defect is observed by using the frequency and the phase of temperature modulation on examined surface (Wiggenhauser, 2002). In contrast to PT, it is convenient to use LT for the researches of mosaics, frescoes or paintings since it is not sensitive to non-uniform heating and local emissivity variation (Meola, *et al*., 2005) and since it is operated within very low increase of surface temperature

(Giovanni, *et al*., 2002). This technique also gives information about the material composition (Giovanni, *et al*., 2002).

Within the **modulated lock-in thermography (MT)**, a phase angle value may be associated to specific characteristic of materials like density, porosity, hardness *etc*.; that is why MT can be used for the characterisation of many materials in different fields (Meola, *et al*., 2004). MT is capable to discriminate the similar materials and this feature can be advantageously exploited to evaluate modifications that occur in material characteristics as consequence of ageing, or exposure to adverse environmental conditions (Meola, *et al*., 2004).

Pulse phase thermography (PPT), is another active thermography technique. In PPT, the surface is heated in pulse mode like in PT and then the results are presented in terms of phase (amplitude) images like LT (Meola, *et al*., 2005). Similar to PT, survey on valuable artworks by using PPT should be done carefully; because while PPT gives more information about the problems in depth, it needs more temperature difference with the ambient temperature which means that the surface of material is heated much more than other techniques. (Giovanni, *et al*., 2002)

2.3.4 Passive thermography

Passive thermography is a kind of analysis method that measures the heat flux generated by natural boundary conditions (Grinzato, *et al*., 2002a) (Figure 2.3). Monitoring is done for diagnostic purposes, to detect irregularities (Avdelidis, *et al*., 2003b). By the help of high thermal inertia characteristics of materials, thermal differences on surface can be examined by IRT (Grinzato, *et al*., 2002a, Moropoulou, *et al*., 2001). Thermal bridges and defects behave as heat sources which make them to be seen clearly if enough temperature difference is provided (Grinzato, *et al*., 1998). Moisture can also be detected by variation in heat conductivity which again causes temperature difference between dry and moist material (Wiggenhauser, 2002,

Moropoulou, *et al*., 2001). Problematic areas can be identified from thermographic image analysis, furthermore, results of cleaning operations can be followed and performance of intervention can be assessed by passive thermography (Moropoulou, *et al*., 2001).

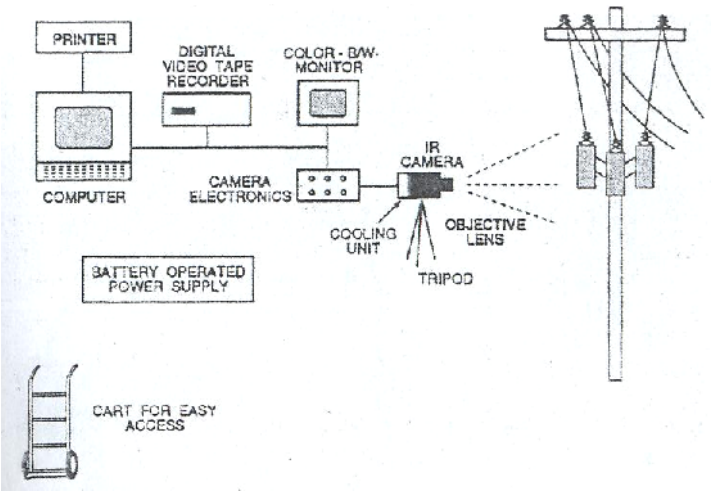

Figure 2.3 Schematic view of experimental setup for passive thermography; infrared camera recorded the IR images as a result of thermal gradient between the examined object and environmental condition (Maldague, 2001: 267)

2.3.5 Assessment of building failures by QIRT

IRT is applied commonly for the investigation of building envelope; walls and roofs. Anomalies such as missing, damaged, misplaced or saturated thermal insulation as well as air leakages around the openings are seen as warmer areas on the exterior surfaces and colder areas on the interior surfaces if there is enough thermal difference between inside and outside of a structure and if interior is hotter than the exterior (Titman, 2001). The results of *in-situ* IR studies can change in different seasons. If the outdoor survey on site is done in winter, thermal bridges are noticed as light patches due to the high temperature of interior; heat losses from interior cause a temperature increase (Balaras and Argiriou, 2002). It is the same for the

indoor study in summer. But this time, absorbed solar energy by the exterior wall surface provides the visibility of heat losses (Balaras and Argiriou, 2002).

Moisture problem of structures can be investigated by IRT. This method is used to detect the location of wet areas, its shape and changes in time. (Avdelidis, *et al*., 2003a, Ocana, *et al*., 2004, Tavukçuoğlu, *et al*., 2005, Titman, 2001, Wiggenhauser, 2002). In the existence of entrapped moisture, thermal conductivity of porous material increases and thermal resistance decreases and then a kind of thermal bridge is occurred which means that it can be detected by IRT easily (Tavukçuoğlu, *et al*., 2005). Thermal behaviour of damp areas is explained by Titman (2001). As the author states, if the layers of a material below the surface are saturated while the top surface is dry, saturated layers should act as a heat sink during the daytime. Thus, the surface over sound areas will be warmer than the surface over moist areas and the temperature of sound surface will increase throughout the day. As a result of that, thermography provides to observe the water or moisture in porous materials as cold patches (Tavukçuoğlu, *et al*., 2005) and the visibility of moist areas can be enhanced by heating the surface due to high heat capacity of water (Grinzato, *et al*., 1998). After sunset, warmer condition of surfaces over sound areas may continue for a few hours; but after a while, the surface over saturated layers may get warmer (Titman, 2001). Additionally, the appearance of moisture depends on air temperature and relative humidity levels (Grinzato, *et al*., 2002a).

Balaras and Argiriou (2002) emphasize the importance of IR for roof inspection. Existence of water on roof can cause serious damages such as reduction in the thermal effectiveness of insulation, membrane deterioration, additional load to the building and damages on interior surfaces. Thermography provides to determine the locations of problematic areas on roof as colder areas. But in winter, moisture leaks and water damages on roof are detected with high temperature because of damp insulation. Heat transfer coefficient changes totally as a result of dampness of insulation.

Roughness is a kind of deterioration and it is seen commonly on materials of historical structures. If the roughness of a material is much, intensity will become higher while thermal effusivity will be lower that causes a rapid increase on surface temperature; as a result of that material will be observed warmer (Avdelidis, *et al*., 2004)

Meola, *et al*. (2005) describe how the defects become visible by thermography. Deep defects do not appear in compact form; on the contrary thermal dispersion is noticed because of the increase in thickness. In other words, the deeper the defect, the thicker the material. Additionally, defects under the porous plaster layers are not observed clearly while it is easier to see the defects under compact plasters. Thermal conductivity of compact plaster is higher than the conductivity of air, but the pores filled with air in porous plaster reduce its thermal conductivity; thus air prevent the visibility of defects.

2.4 Use of Ultrasonic Testing Method for Failure Assessment

The ultrasonic or ultrasound terminology is used for the high-frequency sound waves which mean higher frequency than the range of human heard (Meola, Maio, Roberti and Carlomagno, 2005; Bray, *et al*., 1992: 18). If it is thought that audible frequency range is between 20 and 20.000 Hz (Paik, Lee and Abidi, 2008), 20.000 Hz is the lower end of ultrasonic range while the upper end of this range is not well-defined (Bray, *et al*., 1992: 18). Ultrasonic testing method has portable instruments which give chance to apply this inexpensive technique easily during the *in-situ* surveys; but the thing that has to be considered is the calibration of instrument and evaluation of the results (Bray, *et al*., 1992: 18). For this reason, ultrasonic testing method needs specialist for the studies. When compared with IRT, ultrasound inspection is not a fast technique. Some studies on concrete using ultrasonic testing showed that precise data could not be achieved to identify the size or location of small defects, especially

in thin layers of concrete. On the other hand, structural heterogeneity of materials can be evaluated precisely at thicker samples (Meola, *et al*., 2005).

2.4.1 Fields of use

The ultrasonic testing is a useful technique especially for the examination of stones in terms of their elasticity, anisotropy, mechanical strength and state of deterioration (Christaras, 1999). This technique allows to assess the soundness of stones to identify the presence of any discontinuity and/or material failure, such as voids and fracture zones (Bray, *et al*., 1992: 278; Kahraman, *et al*., 2008). It is also useful to follow and examine the changes in some basic physico-mechanical properties of stones in relation to moisture content, weathering and loading in compresion (Christaras, 1999; Kahraman, *et al*., 2008).

2.4.2 General principles of ultrasonic testing

The ultrasonic method works on the basis of sound waves travelling inside the solid materials (Meola, *et al*., 2005; Bray, *et al*., 1992: 253). A beam of ultrasonic energy is launched inside the material by exciting, with a high-voltage pulse, a piezo-electric crystal contained in a transducer, which is called transmitter probe, in contact with the material (Meola, *et al*., 2005). The energy transmission between probes are affected from the local variation of material characteristics, this variation causes difference on the speed of waves on measured area that gives information about the material characteristics like density, stiffness, porosity *etc* (Meola *et al*., 2005). The propagating of ultrasound wave in humid or rainy condition is fast whereas the speed of wave decreases in air (Paik, *et al*., 2002).

2.4.3 Ultrasonic testing methods

Ultrasonic pulse velocity measurement can be performed in three different ways, which are direct, semi-direct and indirect methods (Kahraman, *et al*., 2008; Meola, *et al*., 2005). As it is seen in Figure 2.4, in direct method, transmitter and receiver are placed on opposite surfaces of tested object to measure the transit time. The two transducers are arranged at a 90º angle in semi-direct transmission mode, while they are placed on the same surface of the specimen tested in indirect measurement method and the points of receiver arranged are changed along a specific line (Meola, *et al*., 2005; Christaras, 1999). Especially the last method is applicable for the *in-situ* studies (Christaras, 1999) and a single probe can be used instead of two different transmitter and receiver probes in indirect method (Meola, *et al*., 2005). Another thing that has to be considered is that the surfaces of probe and tested material have to be totally in contact with each other to get the correct data. A coupling liquid or gel is also used on surfaces of probes to provide the good contact (Meola, *et al*., 2005).

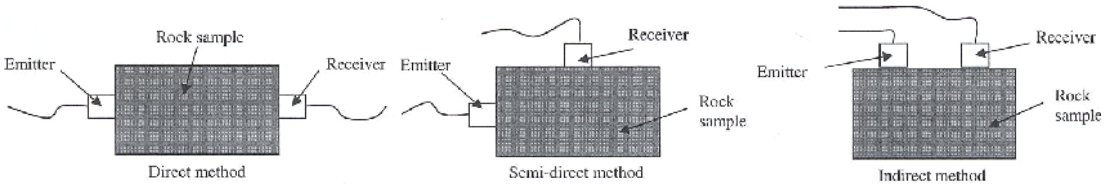

Figure 2.4 Schematic views direct, semi-direct and indirect methods of ultrasonic measurements (Kahraman, *et al*., 2008: 12)

Lemoni and Christaras (1999) compare direct and indirect methods. According to the authors, the direct transmission mode is the most satisfactory method, because the direction of waves is normally parallel to the transducers. Thus, when the transducers are on opposite sides of the material, the propagation of pulses will be quicker and pulse velocity will be higher than the results of the indirect method. The statistical

analysis on concrete done by Turgut and Kucuk (2006) reveals that the average value of direct UPV is 9% and 4% higher than the average of indirect UPV in the casting direction and indirect UPV in the horizontal direction, respectively. Direct and indirect UPV values of autoclaved aerated concretes were measured by Grinzato, Bison and Tavukçuoğlu (2009). Direct UPV values for the autoclaved aerated concrete in the dimensions of 5cmx5cmx5cm were found to be 1863m/s±79 m/s; while the indirect UPV values for the sound surfaces of samples in the dimensions of 5cmx5cmx20cm were lower with the average value of 722m/s±69 m/s. The indirect transmission arrangement is less sensitive than the direct method since the layer close to the surface affects the pulse velocity measurements and waves prefer the shortest way to reach the receiver, so the ultrasonic wave can prefer to travel close to surface (Lemoni and Christaras, 1999). That is why the presence of any anomaly at deeper layers may not be detected with the indirect measurements.

2.4.4 Assessment of building failures by ultrasonic testing in indirect transmission mode

Indirect UPV measurement is used for several purposes. One of them is the estimation of weathering depth at the surface of material. The graph of transit time as a function of the distance between the centers of transducers gives information about the depth of weathering (Lemoni and Christaras, 1999). For sound material, slope on the graph should be constant since the travelling speed of waves in material is constant (Meola, *et al*., 2005). But if there is a change on the slope, it signals the difference in pulse velocity that is occurred because of weathering (Christaras, 1999). Velocity close to the surface is lower than the velocity value of deeper layers (Christaras, 1999). The expected slopes in the existence of weathering condition are shown in Figure 2.5. The thickness of weathered surface layer can be estimated by using the Equation (11) given below (Christaras, 1999: 134):

$$D = \frac{Xo}{2}\sqrt{\frac{Vs - Vd}{Vs + Vd}} \tag{11}$$

where *D* represents the depth of weathering (mm), *Xo* is the distance at which the change of slope occurs (mm), *Vs* is pulse velocity in the sound rock (km/s) and *Vd* symbolises pulse velocity in the damaged rock (km/s).

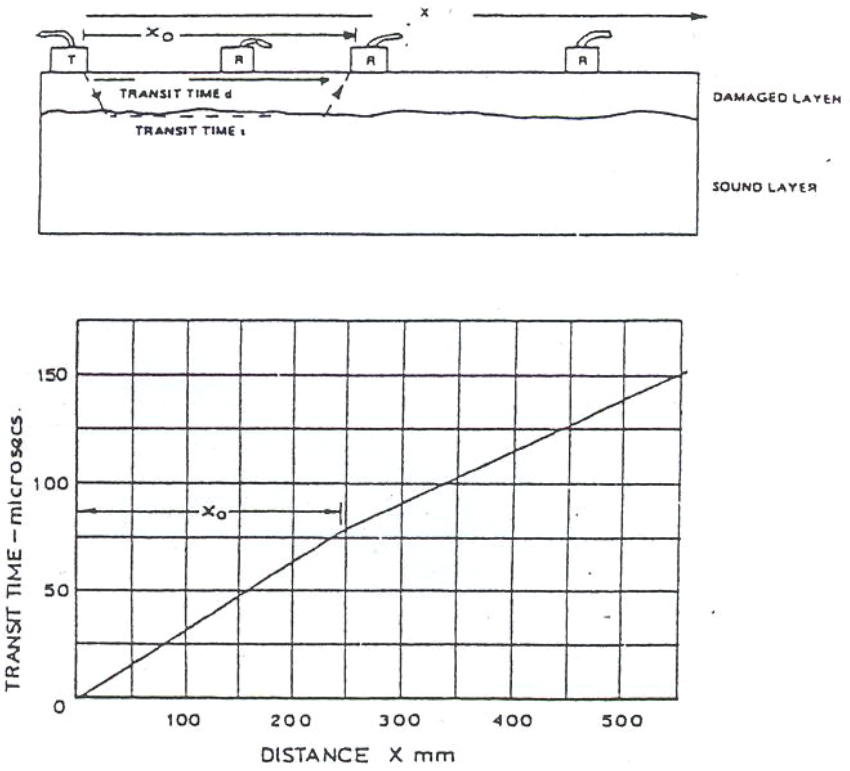

Figure 2.5 Schematic diagram of indirect measurement method (at the top) showing the depth of damaged layer and transit time versus distance graph of the same case (at the bottom) showing the difference on slope as a result of damage (Christaras, 1999: 134)

Apart from weathering depth measurement, another investigation area of indirect transmission mode is the evaluation of the consolidation success. After treatment, consolidation depth can be estimated to understand the effectiveness of intervention. If the consolidation is successful, a line without any displacement should be seen in the graph of transit time as a function of distance (Christaras, 1999). However, non-

consolidated or damaged zones cause displacement of regression line and the slope of regression line changes according to the thickness of damage (Christaras, 1999).

The third application area of indirect UPV measurement is the estimation of crack depth. For this purpose, transmitter and receiver are placed on two different sides of crack as shown in Figure 2.6. Like the consolidation evaluation, displacement of regression line is assessed to estimate the depth of crack (Christaras, 1999). This estimation can be calculated by using the following equation (Christaras, 1999: 135):

$$h = \frac{L}{2}\left(\frac{T_2}{T_1} - \frac{T_1}{T_2}\right) \tag{12}$$

where h is the crack depth (mm), L is the distance between the centers of transmitter and the crack (mm), T_n is the transit time (μs).

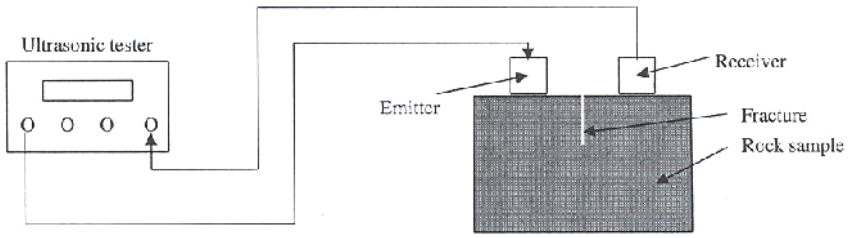

Figure 2.6 Schematic view of pulse velocity measurement by using indirect method for the crack depth estimation (Kahraman, *et al*., 2008: 13)

There is an inverse relation between the pulse velocity and fracture depth, which means that pulse velocity decreases when the fracture depth increases (Kahraman, *et al*., 2008). Weathered state of stones can also be evaluated by using UPV measurements; decline in pulse velocity value signals that the condition of material is not good (Snethlage and Ettl, 1996). Moreover, types of rocks affect the slope of regression line. While igneous rocks have the highest slope, metamorphic rocks have the lowest (Kahraman, *et al*., 2008).

2.5 Mapping of Visual Decay Forms

Mapping of visual decay forms is the description, documentation or presentation of weathering state of the stones (Fitzner, Heinrichs and Kownatzki, 1995: 42). It is the first step of *in-situ* studies (Tavukçuoğlu, *et al*., 1999). Mapping can be prepared for a stone surface or a façade or for the whole facades of a building (Fitzner, *et al*., 1995: 42). Different stone types and weathering forms are symbolized with different schemes and colors which make it possible to get an idea about the distribution of stone types or damage extension qualitatively as well as to obtain the data of them quantitatively (Fitzner, 2004 and Fitzner, Heinrichs and Kownatzki, 1992).

The necessity of mapping is explained by Fitzner, (2004), Fitzner, *et al*. (1995:41) and Tavukçuoğlu, *et al*. (1999). According to them, many historical buildings made from stone are damaged in time. These damages can be as a result of natural weathering processes, influences of pollution, insufficient maintenance, modified utilization, application of sensible materials or inappropriate conservation. In this respect, the purpose of mapping is to understand the reason of deterioration and their mechanisms as well as to determine the weathering state of natural stones. The correct definition of problems and detailed information about the weathered state are significant for the correct maintenance of structures that emphasizes the importance of mapping. It also provides to predict the activities of stones that can be seen in future, because it is possible to see the weathering forms, intensity, their extent and the distribution of damages from mapping (Fitzner, 2004 and Fitzner, *et al*., 1992).

Evaluation of weathering forms can be done for different aspects. For instance, mapping form developed by Fitzner is classified into four titles with several subtitles; the main groups are *loss of stone material, discoloration/deposits, detachment and fissure/deformation* (Fitzner, *et al*., 1995: 44, 46, 49, 51). Each decay form can be also categorized according to degree of damage; like *very severe decay, severe decay, medium decay* and *slight decay* (Tavukçuoğlu, *et al*., 1999; Fitzner, *et al*., 1995). These damage maps are significant since they reveal the urgency of

intervention whether the structure needs an intervention in a short period of time or it has time for the complete long term examination (Fitzner, 2004, Fitzner, *et al*., 1995: 72 and Fitzner, *et al*., 1992).

Tavukçuoğlu, *et al*. (1999) point out the use of mapping of visual decay forms together with the thermal images of building surfaces. Since surface temperature changes as a consequence of different problems, combined use of these two non-destructive methods gives information about the types of deterioration, their distribution and extension in the structure and the reasons of these deteriorations.

2.6 Cenabi Ahmet Paşa Camisi

Cenabi Ahmet Paşa Camisi is a 16th century structure built by Mimar Sinan (Esen, 2008; Başkan, 1993: 7) when Cenabi Ahmet Paşa was the "Anadolu Beylerbeyi" in Ankara (Boztepe, 1987: 34). As it is shown in Figure 2.7, the mosque is situated in a courtyard which is located between Ulucanlar and Uzunkavak Streets in Ankara (Esen, 2008; Boztepe, 1987: 6). The mosque forms a complex together with a fountain and the tombs of Cenabi Ahmet Paşa and Azımi in the courtyard (Esen, 2008; Başkan, 1993: 7; Boztepe, 1987: 6). Boztepe (1987: 37) defines the building as a classical Ottoman mosque because of its square plan covered by a single dome (Figure 2.8). Besides the plan and dome; its symmetric settlement, south orientation, unique entrance on north side and portico in front of the entrance are all characteristics of the 'single unit Ottoman mosques' (Boztepe, 1987: 37).

Boztepe (1987: 18, 23) and Başkan (1993: 9, 21) explain the architectural properties of Cenabi Ahmet Paşa Camisi. As they mentioned, the tuff walls of building were made of cut stone while the dome was made of brick and covered with lead. The windows of first, second and third rows had pointed arches and these were built with red and white stones seen from outside.

The structure was repaired several times for centuries and these interventions underwent in time caused the structure to lose most of its original wall paintings. At 1940's, the interior surfaces of the walls renewed with cement-lime based plaster and paint, and then repainted with the layers of gypsum coat and plastic paint at 1992 (Esen, 2008; Kökdemir and Dirican, 2008) (Figure 2.9). There were only few remains of old wall painting left in the structure. Kökdemir and Dirican (2008) reported some spot analyses on the layer composition of painted wall surfaces and the results of these analyses have shown the presence of original/historical plaster and wall painting layers hidden behind the recently repaired surfaces (Figure 2.10). For instance, the decoratively-painted surfaces above the first-layer windows had two layers of historical plasters underneath the recent gypsum coat and decorative wall painting (Kökdemir and Dirican, 2008). However, the white painted wall surfaces with plastic paint, alternatively painted arch surfaces above the first-layer windows and strip-like decorative wall paintings surrounding the second-layer windows had renewed sublayers, such as cement-lime based plaster of 1940's underneath the recent gypsum coat and wall painting (Kökdemir and Dirican, 2008) (Figures 2.9 and 2.11).

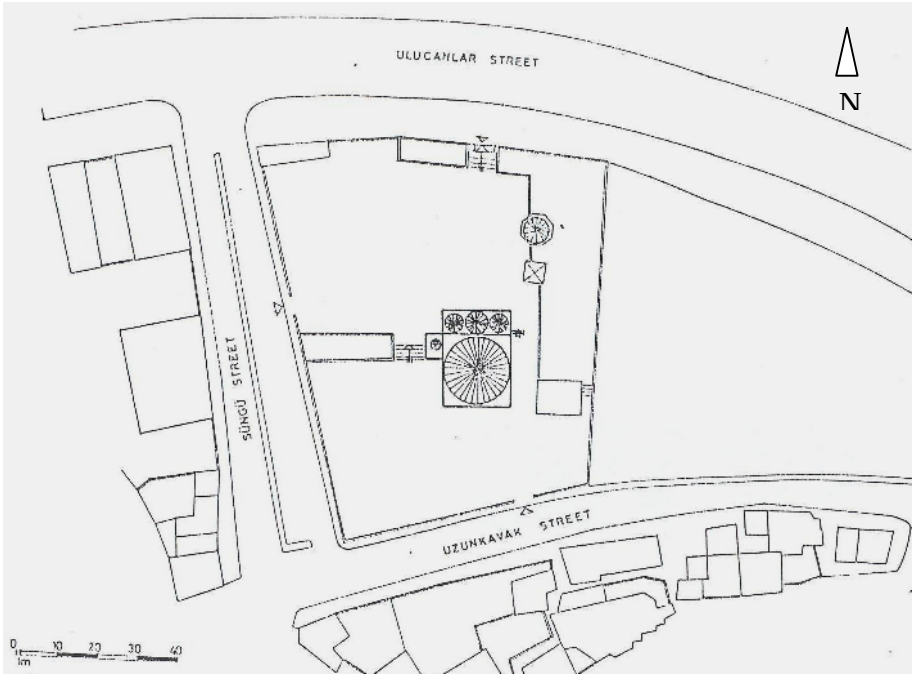

Figure 2.7 Site plan of Cenabi Ahmet Paşa Camisi (Boztepe, 1987: 7)

Figure 2.8 Ground level plan of Cenabi Ahmet Paşa Camisi (http://archnet.org/library/images) and views from four facades of the building

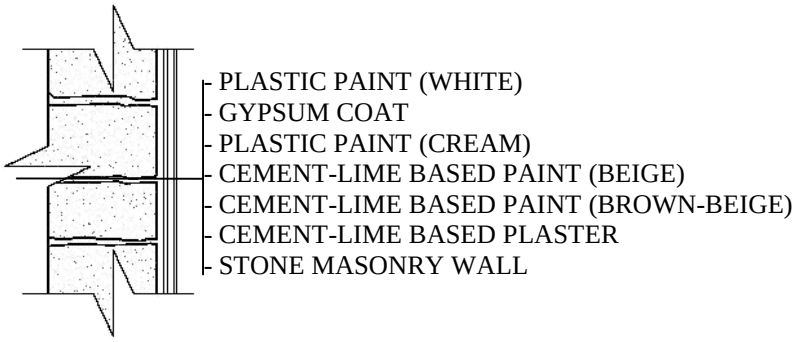

Figure 2.9 Geometric description of wall section showing the order of layers for plastic painted part (Kökdemir and Dirican, 2008: 11)

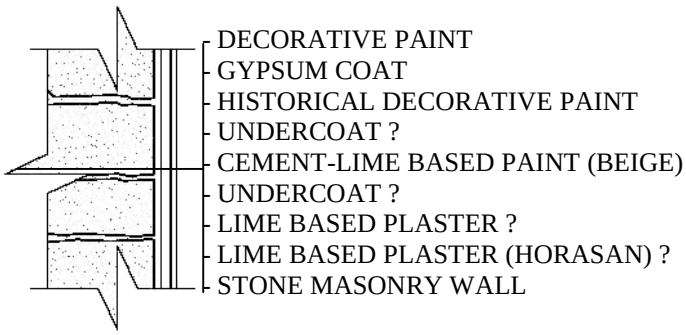

Figure 2.10 Geometric description of wall section showing the order of layers for the decoratively-painted part above the first layer window (Kökdemir and Dirican, 2008: 12)

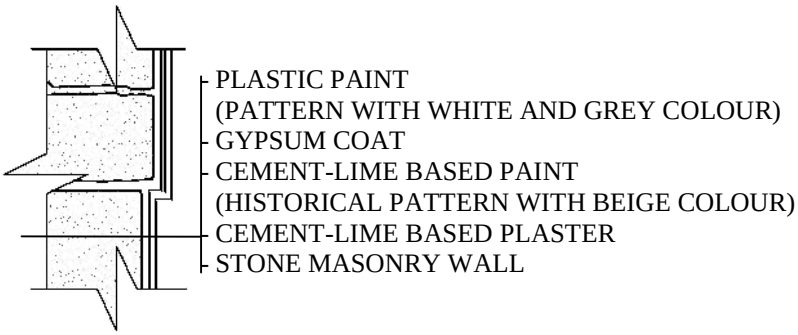

Figure 2.11 Geometric description of wall section showing the order of layers for the arch above the first layer window (Kökdemir and Dirican, 2008: 12)

One of the main problems of structure was the crack on east wall and it was wondered if the crack was derived from the foundation or not; because it could cause structural problems that needed some serious precautions (Çetin and Canbay, 2008). The research about the source of cracks was done by Çetin and Canbay and the results were reported. According to that report, the building was settled on the clayey ground. That clayey layer was deeper on the southeast of structure and because of high swelling capacity of clayey soil; differentiation was occurred in the settlement of structure. Especially after the hot and dry summers of last years, an increase on the width of crack was observed which supports that the crack is still active.

CHAPTER 3

MATERIAL AND METHOD

In this section, material of the study, Cenabi Ahmet Paşa Camisi, and the methods used during the *in-situ* survey which are mapping of visual decay forms, ultrasonic testing and infrared thermography are presented.

3.1 Material

Cenabi Ahmet Paşa Camisi is a 16th century Ottoman mosque in Ankara, which was built by the great architect 'Mimar Sinan'. The building walls were faced with ashlar blocks of tuff stone at outside while plastered at inside; the basement masonry walls, on the other hand, were faced with ashlar blocks of andesite stone (Figure 3.1). The thickness of building walls vary in the range of 1.72m and 2.08m (Archives of General Directorate of Pious Foundation, 2008). The building is heated with a floor heating system, which was recently added to the structure and functioning insufficiently in winter only at prayer times. Moreover, the entrance door was usually left open in summer, permitting air exchange between outside and inside.

Serious cracks were observed at the walls and dome of the structure in recent years. Especially the crack at east wall with an extension from basement to the dome was examined. As it is seen in Figure 3.2, it is possible to see the route of crack both from interior and exterior of the building. The crack was monitored and measured during the survey period and the progress of crack was observed.

Figure 3.1 General view (at the left) and the north façade (front façade) (at the right) of the Cenabi Ahmet Paşa Camisi

Figure 3.2 The exterior (at the left) and interior views (at the right) of crack on the east wall of structure.

When the structure was observed, it was possible to see signals of interventions. For instance, wall paintings had been partially repaired on the right side of minbar on

south wall. Half of this wall painting on right side was repainted while the other half part was left as it was (Figure 3.3). Furthermore, it was observed that tuff surfaces were repaired with cement-based coat at outside (Figure 3.3). Apart from interventions, deteriorations on ashlar blocks of tuff and andesite were observed. Especially material loss and damp areas were seen on the outside wall surfaces (Figure 3.4).

Figure 3.3 Interventions on wall paintings (at the left) and on exterior wall surfaces (at the right)

Figure 3.4 Partial view of deteriorations; material loss (at the left) and dampness problem (at the right)

3.2 Method

A non-destructive *in-situ* survey was conducted on the monument for the assessment of structural cracks, whether they were active or not, the presence of historic wall

painting/plaster layers hidden behind the fine coats recently done and their state of preservation in relation to the recent repairs and moisture problems. These studies were done by non-destructive methods explained under respective headings.

3.2.1 Mapping of visual decay forms

The maps of visual decay forms were produced according to the method developed by Fitzner as cited in literature review section. During the *in-situ* studies, some sketches were drawn and photographs were taken from the examined parts. By using these information, the maps were then drawn on 1/50 scaled elevation and section drawings obtained from the archives of General Administration of Pious Foundations.

Three types of mapping were used to identify the failures and distribution of different materials at structure. The first one showed the structural crack at the east wall of building with its route and extension. Secondly, mapping of material loss and discoloration and deposits on south wall of minaret and west elevation of structure were drawn partially. Lastly, repaired and original stones on south wall surface were determined on the last mapping type. Mappings were prepared by using architectural drawing software AutoCAD 2008 and the results were evaluated with other non-destructive methods.

3.2.2 *In-situ* infrared thermography

In-situ IRT studies of the structure were done by single and sequential IR imaging from interior and exterior surfaces of the structure. Those studies were performed for several times in the months of January, February, May, June and December in day time and at night when there existed a certain thermal gradient between inside and outside. Additional heating sources, such as halogen lamp, hair dryer and fan heater,

providing maximum outputs of 650 Watts, 1000 Watts and 2000 Watts respectively, were used to heat up interior surfaces under examination at varying rates and to contribute to the warming up the inside ambient temperature. The sequential IR imaging *in-situ* was carried out by taking infrared images successively at 2-10 seconds intervals for a period of 5-10 minutes during the heating and then cooling conditions. The view of experimental setup used for data collection *in-situ* was shown in Figure 3.5.

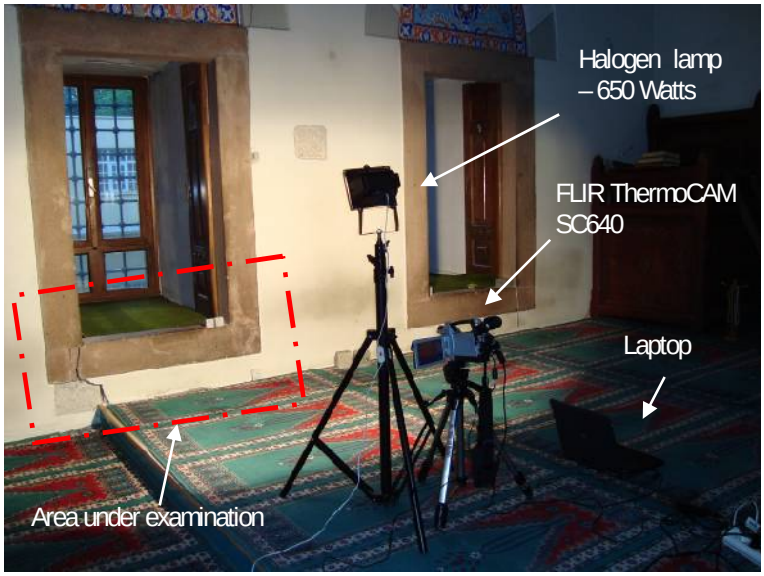

Figure 3.5 The experimental setup used for the sequential IR imaging of wall surfaces under the exposure of heating by halogen lamp: automatically-recording the IR images of target area at 2s intervals with the IR camera controlled by the laptop.

The temperature evolution in time during controlled heating and cooling processes was deployed for the cracks and the defects inspection. The two graphs showing surface temperature, T, as a function of square root of time and temperature difference, ΔT, as a function of square root of time were produced for the analyses of surface temperature data. The ΔT was the difference between the initial surface temperature of target area and the succeeding surface temperature of the same target area under exposure of heating/cooling. The slope of the linear regression presented the rate of warming up, R_W, or the rate of cooling down, R_C, for each target

area/crack. The ratio between the R_W (or R_C) of each crack/defect to the R_W (or R_C) of neighbouring sound surface was also calculated. The results revealed the thermal behaviour characteristics of structural cracks and defects in relation to depth, moisture content and exposure conditions.

The thermal response of *superficial cracks* neighbouring plaster detachments, *deep cracks* at masonry wall up to certain depths, and *the very deep cracks* passing through the entire masonry wall section was examined under the exposure of the heating and cooling conditions. The very deep cracks permitting air flow through their cavities were called in the text as *the deepest cracks* due to their depth covering the overall masonry wall section. A special care was given to add the reference area, such as visually-sound and dry tuff surface, into the field of IR image to compare the crack/defect with the sound one at the same boundary conditions. The depth of cracks was determined by means of *in-situ* ultrasonic testing in indirect transmission mode. The thermal behaviour of visually-sound stone and jointing surfaces as well as plaster covered masonry wall surfaces was also inspected for the comparisons.

Single and sequential IR imagings were used to assess the thermal behaviour of original and repainted wall paintings. Their temperatures were compared both with each other and also with the temperature of plastic painted wall surface to see whether it was possible to differentiate the original paintings by infrared survey or not.

Original and repaired tuff surfaces as well as different stone types like tuff and andesite at exterior walls were also examined in terms of their thermal inertia characteristics. The sun exposure was used as the natural heating source in order to monitor the rate of warming up/cooling down of the target surfaces. During the sequential analyses in heating period, it is significant not to forget to leave out the areas that shadow of trees fallen on.

The *in-situ* QIRT survey was done by using the long wave sensitive “FLIR ThermaCAM E65” and “FLIR ThermaCAM SC640” thermographic equipments.

The technical specifications of those instruments were summarized in Appendix A.1 and A.2. The analyses of IR images were done by using the softwares: “ThermaCAM Reporter 2000” and “ThermaCAM Researcher Professional” as well as the “M.S. Office Excel”. Supportive *in-situ* measurements were taken during the *in-situ* surveys in order to improve the accuracy of *in-situ* infrared data acquisition and the quantitative analyses of that data. Those measurements were based on the monitoring the microclimatic conditions of inside air and outside air, air movements through the cavity of cracks, the depth and width sizes of cracks. The results of those measurements were summarized in the Appendix B. The inside and outside climatic data were recorded by “HOBOware Pro” dataloggers. The air flow and air velocity measurements, V_{AIR}, were taken, especially from the fronts of cracks at masonry wall by means of “VELOCICALC 8346” anemometer. The technical specifications of anemometer were summarized in Appendix A.4. The width and depth measurements of cracks were taken by a vernier calliper providing a precision of 0.05mm. The presence of moisture content in the masonry wall section was determined by using a protimeter “Surveymaster”. The distance between the IR camera and target area was measured by the “BOSCH DLE 150 laser meter”.

3.2.3 *In-situ* ultrasonic pulse velocity (UPV) measurements

The *in-situ* ultrasonic testing was done to estimate the depth of crack/discontinuity. That knowledge was essential for complementing the *in-situ* QIRT analyses on visible cracks while their real depths were not possible to measure. The study was conducted on plastered masonry wall surfaces and fair-faced red tuff blocks where superficial and deep cracks were visually-observed, especially at surfaces where sequential IR imaging was performed.

The UPV measurements were done in indirect transmission mode (parallel to the surface) by using a portable PUNDIT PLUS CNS FARNELL instrument with 54kHz and 220kHz transmitters. The technical specifications of this instrument were

summarized in Appendix A.3. No coupling agent was used between the surfaces of stone and transducer not to introduce any foreign material and contamination on historic stone surfaces. The probes were used at the same surface: the transmitter was placed on a suitable point of the surface and the receiver was placed on the same surface at successive positions along a specific line (Figure 3.6). The position of the receiver was then moved forward at 30mm intervals, while the transmitter keeping its initial position. Twenty readings of transit time were recorded for each positioning and their mean was used as the transit time data. The data achieved were confirmed by the measurements taken from the same route for the second time. The transit time was plotted as a function of distance between the centers of transducers. Any change on the slope of regression line would exhibit the change in ultrasonic velocity in depth (Christaras, 1999). The weathered stone surface or any defect in stone, presenting inferior quality when compared with the sound one, was expected to exhibit larger slope of regression line (Christaras, 1999; Kahraman, *et al*., 2008; Lemoni and Christaras, 1999). The arrangement of transducers at the same surface when placed at the opposite sides of a crack/defect, made it possible to calculate its depth (Figure 3.7). The depth attained with the indirect UPV measurements was estimated using the following equation (Christaras, 1999: 135):

$$h = \frac{L}{2}\left(\frac{T_2}{T_1} - \frac{T_1}{T_2}\right) \tag{12}$$

where h is the crack depth (mm), L is the distance between the centers of transmitter and the crack (mm), T_n is the transit time (μs).

When there were successive cracks on the route of receiver, several measurements were taken from the same route for two cases: At the first case, the transmitter was located at the left side of the cracks and the receiver was moved from left to right (left-to-right direction). At the second case, the transmitter was located at the right side of the cracks and the receiver was moved from right to left (right-to-left direction). The fracture at jointing was the first crack on the route of left-to-right

measurement while the deep crack was the first crack on the route of right-to-left measurement.

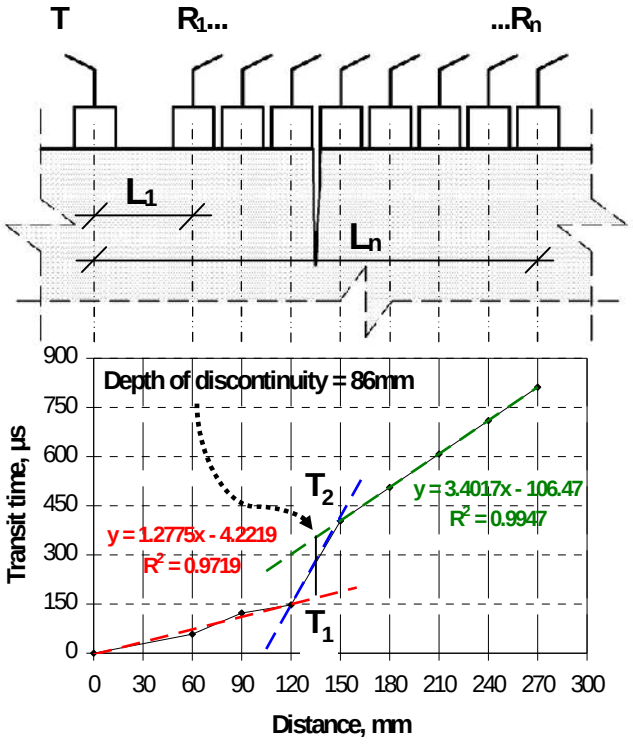

Figure 3.6 Schematic drawing of UPV measurements in indirect transmission mode showing the location of **T**ransmitter, **R**eceiver and the distance between those probes travelled by the ultrasonic wave, **L**, (at the top); the linear fitting of transit time readings as a function of distance between the centers of transducers (at the bottom).

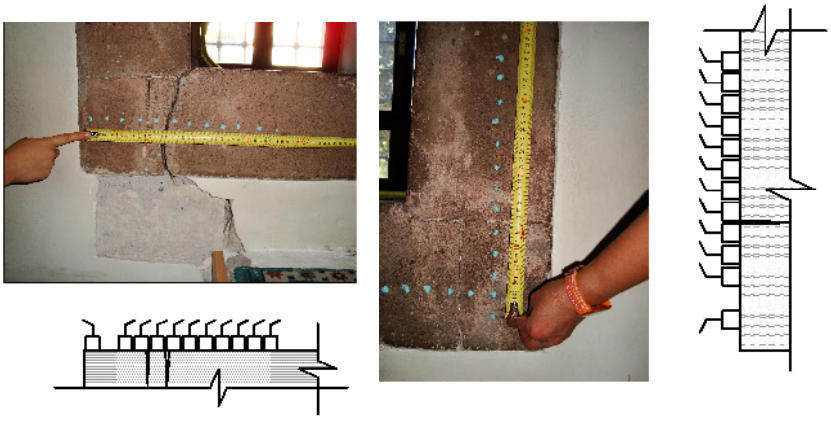

Figure 3.7 The arrangement of transducers on red tuff surfaces when placed at the opposite sides of a deep crack (at the left) and at the opposite sides of jointing between two red tuff blocks (at the right).

The *in-situ* NDT studies should be supported by some laboratory analyses in order to obtain reference data for the comparisons and correct interpretation of the *in-situ* data. However, due to the difficulty in collecting samples from the historic structures and in producing representative samples for the historic structure/fabric, there was a necessity to achieve reference data *in-situ*. A special care was therefore, given to find out the reference UPV and surface temperature data by including the reference area, such as sound and dry stone surface, into the field of study at the same boundary conditions.

CHAPTER 4

RESULTS

The results of the *in-situ* studies are given in this chapter under respective headings with related figures and tables.

4.1 Mapping of Visual Decay Forms

The results for the mapping of visual decay forms applied to the building facades were presented in this section. The maps were analysed to determine the route of structural crack, deteriorated areas, reasons of problems and distribution of different building materials at structure. In Figure 4.1, the route of the structural crack at the east wall was mapped on its exterior and interior elevation drawings.

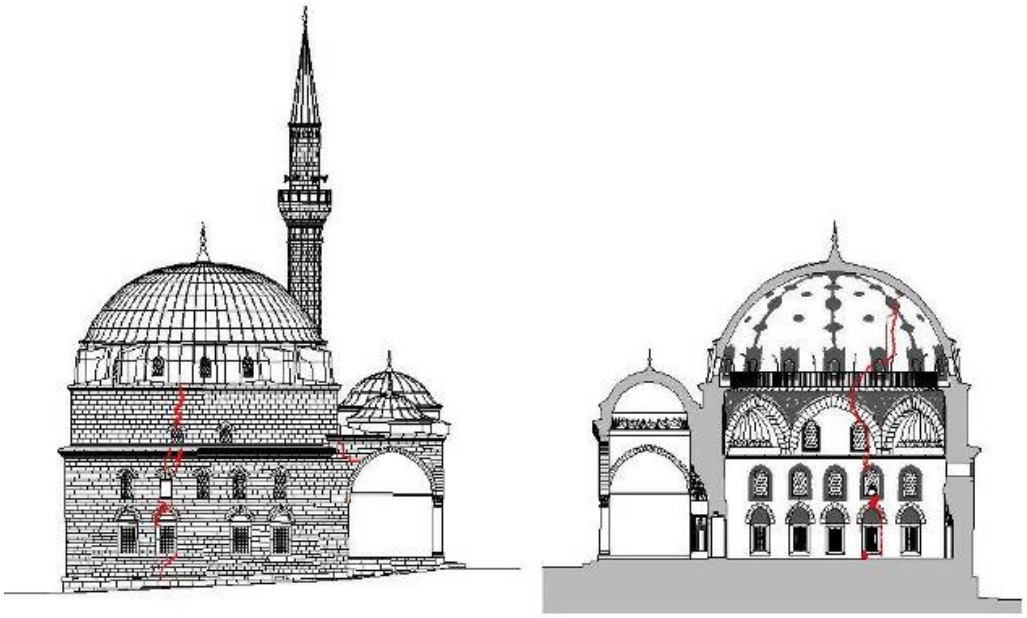

Figure 4.1 The exterior and interior elevations of the east façade, showing the route of the structural crack (in red) due to the differential settlement of the clayey ground.

Material loss of the structure was categorized in three types; slight, moderate and severe material loss. Lack of roof drainage system caused material loss in different damage categories both on the south elevation of minaret and west elevation of the building, as it was shown in Figures 4.2 and 4.3. Severe material loss, on the route of water coming from the dome at south side of minaret, was surrounded with moderate material loss and cement based repair coats. Slight material loss was observed on the first layer of minaret wall surface under the eave. Additionally, cement based repairs on the west wall of building was seen mostly around the moderate material loss.

The same wall surfaces were also mapped from the discoloration and deposit positioning at the locations of biological growths, yellow and black staining (Figure 4.3). Biological growths were encountered on the minaret wall surface and on the west wall surface of building where severe and moderate material losses were occurred on the route of water. Yellow staining was common under the eaves and location of slight material loss on south side of minaret wall was overlapped with the yellow and black staining.

Figure 4.2 Partial view of exterior wall surfaces; south elevation of minaret wall and west elevation of building wall; taken from different directions.

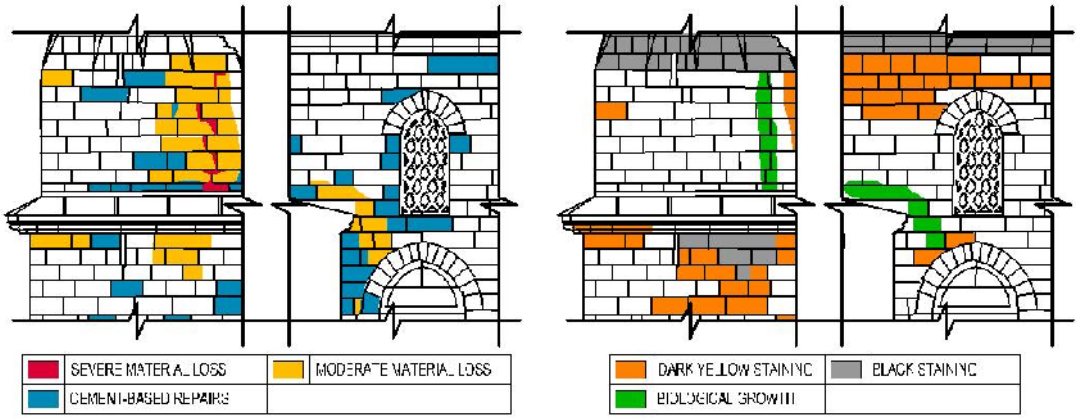

Figure 4.3 Partial elevation drawings for the exterior wall surfaces defined in Figure 4.2 showing the mappings of material loss and cement based repairs (at the left) and discoloration and deposits (at the right).

Distribution of stones on south elevation was mapped partially to specify the locations of stones in different types and cement-based repairs (Figure 4.4). Red and yellowish tuffs were used on arches above the windows. Wall surfaces, constructed with yellowish and white tuffs, were repaired with cement-based coats.

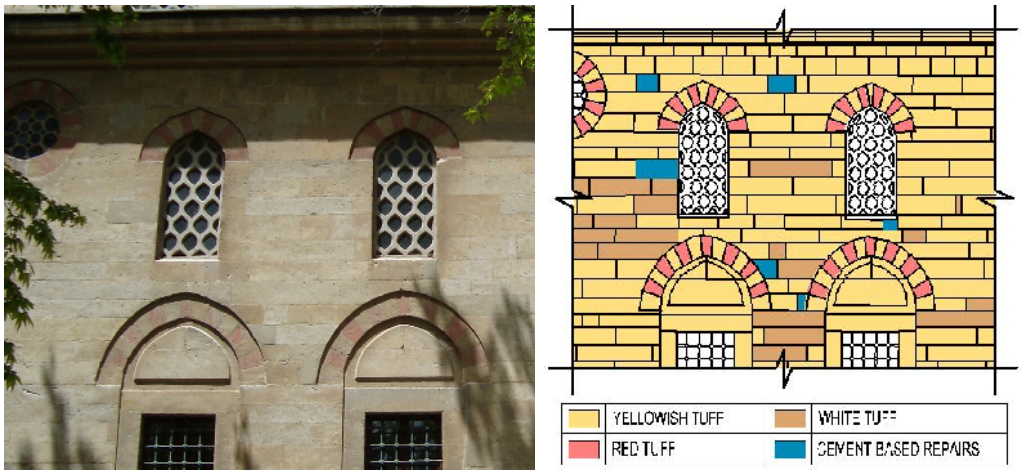

Figure 4.4 Partial view of exterior wall surface on south elevation (at the left) and mapping of selected region (at the right) showing the distribution of yellowish tuff, white tuff and red tuff on exterior wall surface together with the cement-based repairs.

4.2 Quantitative Analyses of *In-situ* Infrared Thermography Survey

The results of *in-situ* infrared thermography survey related to the analyses of structural cracks were summarized below:

- Structural crack at the east wall was monitored by infrared thermography. The crack passing through the transition element and dome was visible in the IR images as a warmer wide path. Its extent along the dome surface was also followed easily by IRT while that could not be visually well-noticed (Figure 4.5).

- IR images were taken from the cracks on first layer window arch at the east wall and detachments around the cracks when a certain thermal gradient was occurred between two sides of wall by functioning the interior heating system. IR image seen in Figure 4.6 was taken at the interior boundary conditions of 6.5°C and 53%RH while the exterior boundary conditions were 2.9°C and 61%RH. Detachments next to structural crack could easily be followed as warmer patches with heterogeneous temperature distribution in IR images while the cracks passing through the wall section were colder than other surfaces. When the same crack and its surrounding were observed eleven months later at the interior boundary conditions of 13.8°C and 36%RH while the exterior boundary conditions were -2.1°C and 63%RH (when a certain thermal gradient was achieved between inside and outside by functioning the interior heating system), it was seen that deteriorated surfaces were lost (Figure 4.7). Additionally, the deepest crack permitting air flow through its cavity (Figure B.1) was observed as the coldest path in the IR image (Figure 4.7). The next very cold path in the same IR image was belonging to non-visible crack, positioned parallel to that visible one. Its route was visually followed from outside while it was hidden behind the plaster layer(s).

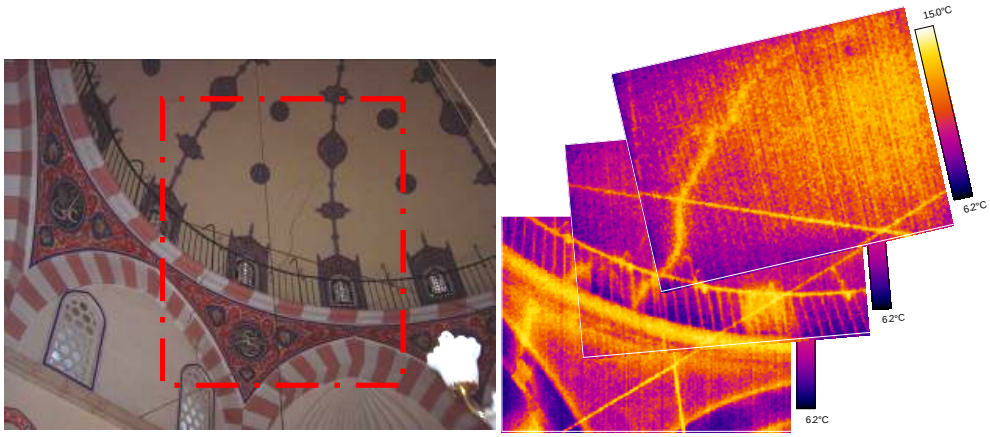

Figure 4.5 View of the structural crack passing through the transition elements and dome (at the left) and IR image of the selected region: The route of crack in IR images as a warmer wide path while it could not be followed clearly by eye.

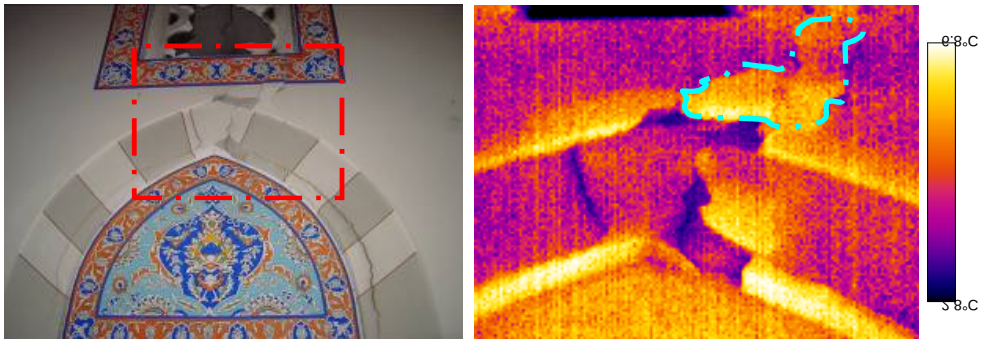

Figure 4.6 Partial view of the structural crack on the east wall (at the left) and the IR image of the selected region (at the right): The detached surfaces as warmer patches with heterogeneous temperature distribution while the deepest cracks were the coldest path in IR image.

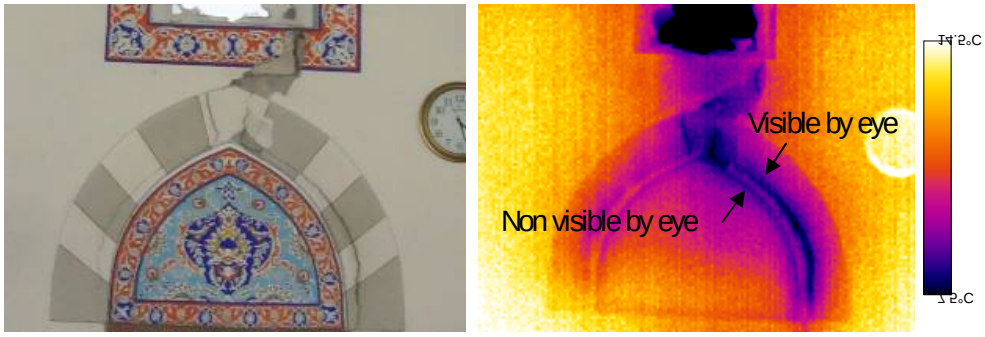

Figure 4.7 Partial view of the same region shown in Figure 4.6 taken eleven months later (at the left) and its IR image (at the right): The detached surfaces were lost (follow the blue circled area in Figure 4.6). The deepest crack following the arch was observed to have the coldest path. The non-visible deepest crack hidden behind the plaster layer was also detected in the IR image as the next colder path.

– The results of thermal monitoring for visually-sound masonry surfaces, such as fair faced red tuff blocks, vertical and horizontal jointings in between those blocks and wall surface coated with cement-lime based plaster and plastic paint, during the heating and cooling periods were summarized in Figures 4.8-4.10. IR sequences were taken at the ambient conditions of 23.7ºC and 46%RH during the heating period of 856s when the wall surface was uniformly heated with halogen lamp and then during the cooling period of 342s after the halogen lamp was turned off. The linear fitting of surface temperatures versus square root of time and temperature differences versus square root of time during the first 360s of heating period and during the first 324s of cooling period were given in Figures 4.9 and 4.10. The results showed that the red tuff surfaces at the bottom, vertical jointing mortar surfaces, horizontal jointing mortar surfaces and red tuff surfaces at the corner exhibited similar thermal response to the warming up conditions with the rates of 0.0243, 0.0232, 0.0231 and 0.022, respectively. They also exhibited similar thermal response to the cooling down conditions with the rates of -0.025, -0.0241, -0.0235 and -0.0234, respectively. These results signalled that tuff and its jointing mortar had similar thermo-physical properties establishing similar thermal inertia characteristics. The wall surfaces coated with cement-lime based plaster and plastic paint had the coldest surfaces with the slowest rates of warming up and cooling down among fair-faced red tuff and jointing mortar surfaces. These plaster surfaces were colder than the fair faced tuff surface with a temperature difference of -0.64ºC and had the warming up and cooling down rates of 0.0179 and -0.0193, respectively.

– Sequential IR imaging of the superficial crack, detached and non-detached surfaces on the south wall of the structure were taken during the heating and cooling conditions and the results were summarized in Figures 4.11-4.13. IR sequences were taken at the ambient conditions of 20.1ºC and 49%RH during the heating period of 616s when the wall surface was uniformly heated with halogen lamp and then during the cooling period of 580s after the halogen lamp was turned off. The linear fitting of surface temperatures versus square root of time and temperature differences versus square root of time during the 616s of heating

period and during the 580s of cooling period were given in Figures 4.12 and 4.13. It was found that the detached plaster surfaces associating with/neighbouring the crack and superficial crack were both warmed up and cooled down faster than the sound surfaces. The warming up rates of the detached plaster surface neighbouring the crack, superficial crack, non-detached plastic paint arch surface and non-detached plastic paint wall surface were 0.0407, 0.0309, 0.0274 and 0.0158, respectively while the cooling down rates of the detached plaster surface neighbouring the crack, superficial crack, non-detached plastic paint arch surface and non-detached plastic paint wall surface were -0.0359, -0.0272, -0.0207 and -0.0119, respectively. Superficial crack and detachment could be differentiated by slightly slower warming up and cooling down rates of superficial crack during the heating and cooling periods.

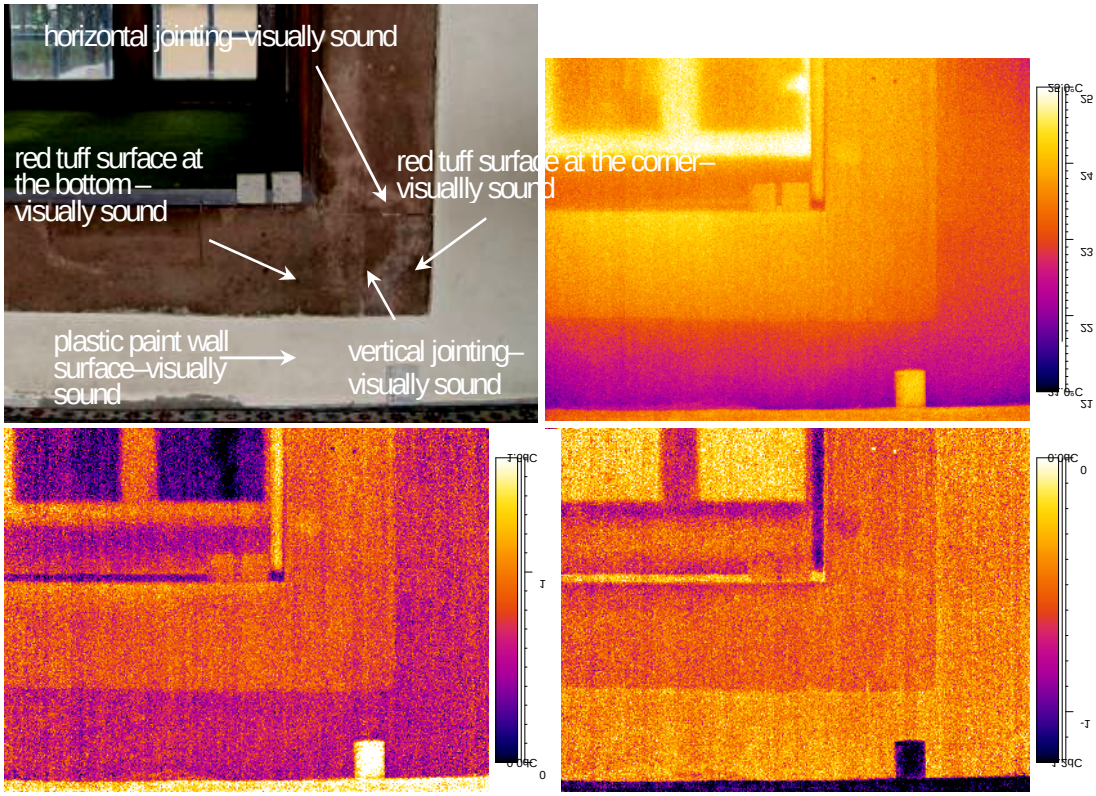

Figure 4.8 Partial view from the right bottom of window opening at the east side of the structure (at the top left), its IR image (at the top right); and the differential IR images of the heating period (at the left bottom) and the cooling period (at the right bottom).

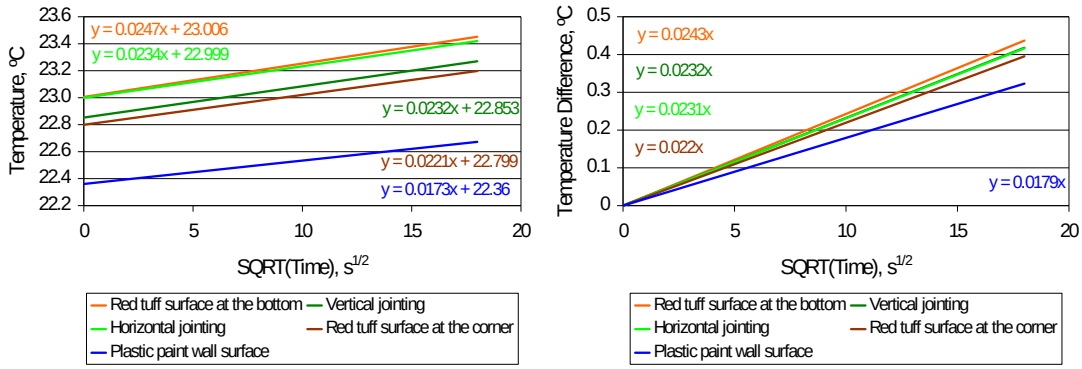

Figure 4.9 The linear fitting of surface temperatures and temperature differences versus square root of time during the heating period for the case defined in Figure 4.8: The visually-sound red tuff and jointing mortar surfaces exhibited similar warming up rates while the plastered masonry wall coated with plastic paint had the coldest surface temperature with the lowest rate of warming up.

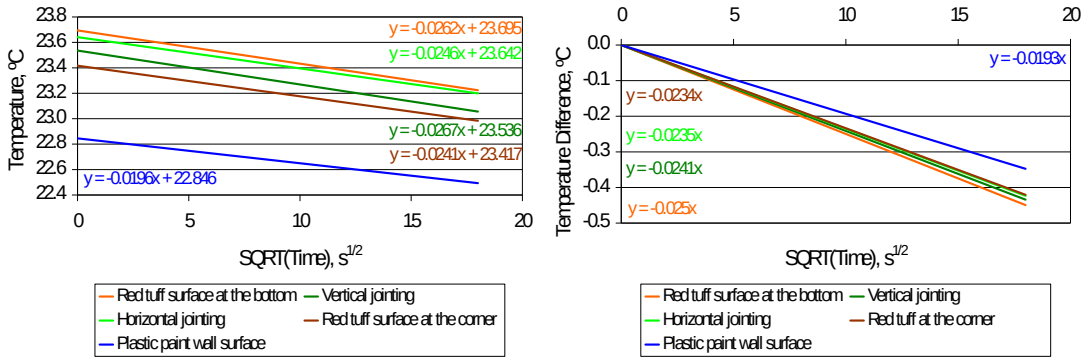

Figure 4.10 The linear fitting of surface temperatures and temperature differences versus square root of time during the cooling period for the case defined in Figure 4.8: The visually-sound red tuff and jointing mortar surfaces exhibited similar cooling down rates while the plastered masonry wall coated with plastic paint had the coldest surface temperature with the lowest rate of cooling down.

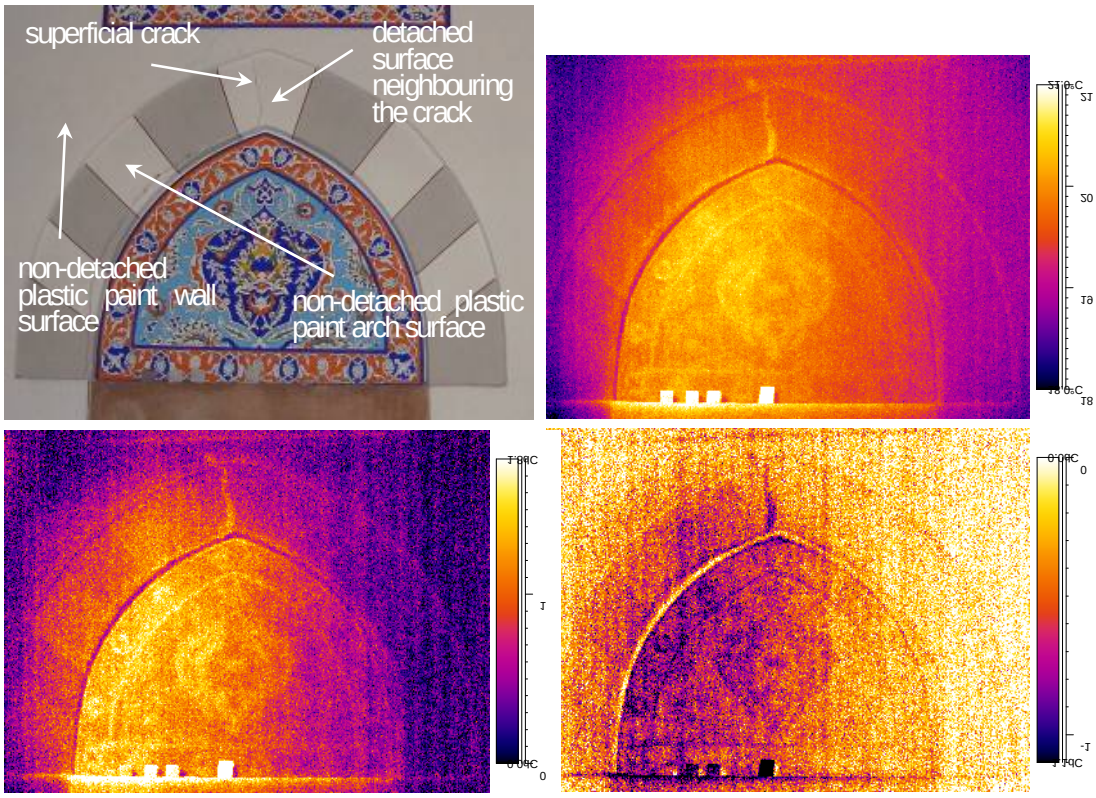

Figure 4.11 Partial view from a window arch located at the south of the structure (at the top left), its IR image (at the top right); and the differential IR images of the heating period (at the left bottom) and the cooling period (at the right bottom).

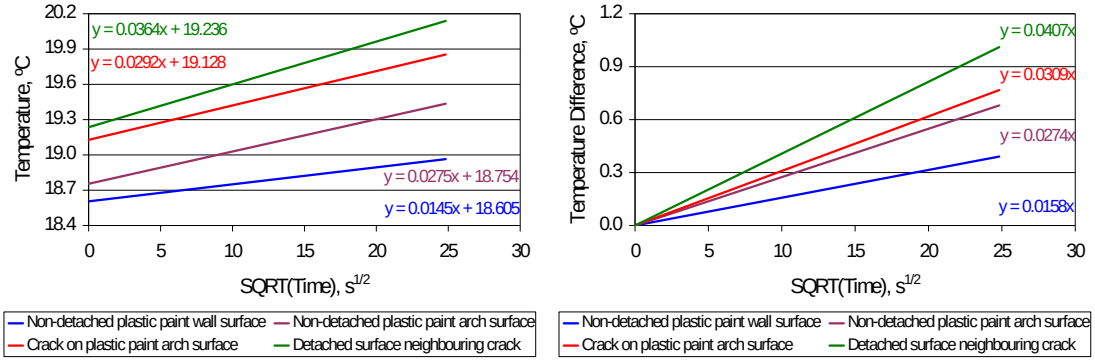

Figure 4.12 The linear fitting of surface temperatures and temperature difference versus square root of time during the heating period for the case defined in Figure 4.11: The detached surfaces warmed up the fastest while the non-detached wall surface coated with plastic paint had the coldest surface temperature with the lowest rate of warming up.

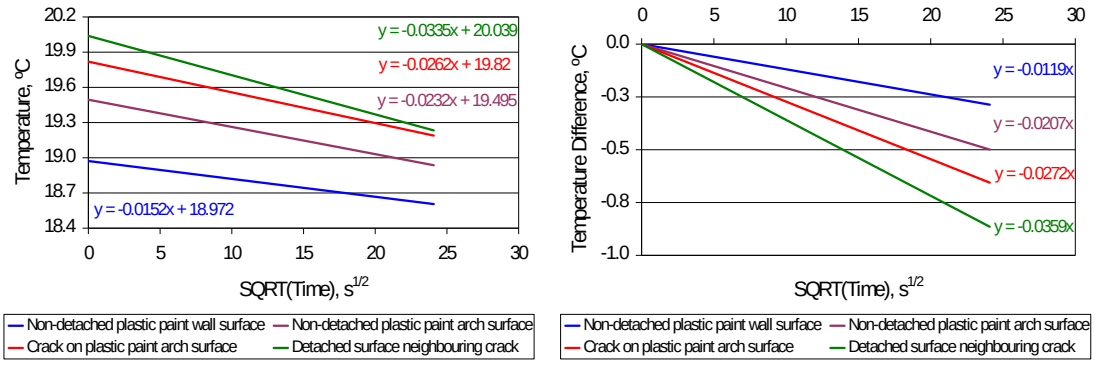

Figure 4.13 The linear fitting of surface temperatures and temperature difference versus square root of time during the cooling period for the case defined in Figure 4.11: The detached surfaces cooled down the fastest while the non-detached wall surface coated with plastic paint had the coldest surface temperature with the lowest rate of cooling down.

– The deepest crack, deep cracks, visually sound red tuff surfaces, detached and non-detached surfaces were monitored during the heating and cooling conditions. IR sequences were taken at the ambient conditions of 23.7ºC and 46%RH during the heating period of 886s when the wall surface was uniformly heated with halogen lamp and then during the cooling period of 430s after the halogen lamp was turned off. The linear fitting of surface temperatures versus square root of time and temperature differences versus square root of time during the first 400s and 282s of heating period, and during the first 120s of cooling period were given in Figures 4.15-4.18. The results showed that the deep cracks at masonry wall with the depths of 147mm and 88mm, presented noticeably slower warming up and cooling down rates than the sound surfaces (Figures 4.14-4.16). The deeper crack had also warmed up and cooled slower than the less deep one. The warming up rates of deep crack in 147mm depth, deep crack in 88mm depth and visually-sound tuff surfaces were 0.0029, 0.0076 and 0.0199, respectively while the cooling down rates of deep crack in 147mm depth, deep crack in 88mm depth and visually-sound tuff surfaces were -0.0109, -0.0119 and -0.0314, respectively. The deepest crack had the coldest surface temperature, being colder than the visually-sound tuff surface with a temperature difference of -0.93ºC and cooled down during the heating period with the rates of -0.0025 and -0.0035 for the cases defined in Figures 4.15 and 4.17, respectively. That signalled the presence

of entrapped moisture in the masonry and air flow through its gap/cavity, both encouraging evaporative cooling there. The deepest crack also presented the slowest rate of cooling down during the cooling period with the rate of -0.008 (Figures 4.14, 4.16 and 4.18). The deepest crack, even neighbouring detachments, had noticeably colder surface temperature than the deep cracks and sound surfaces.

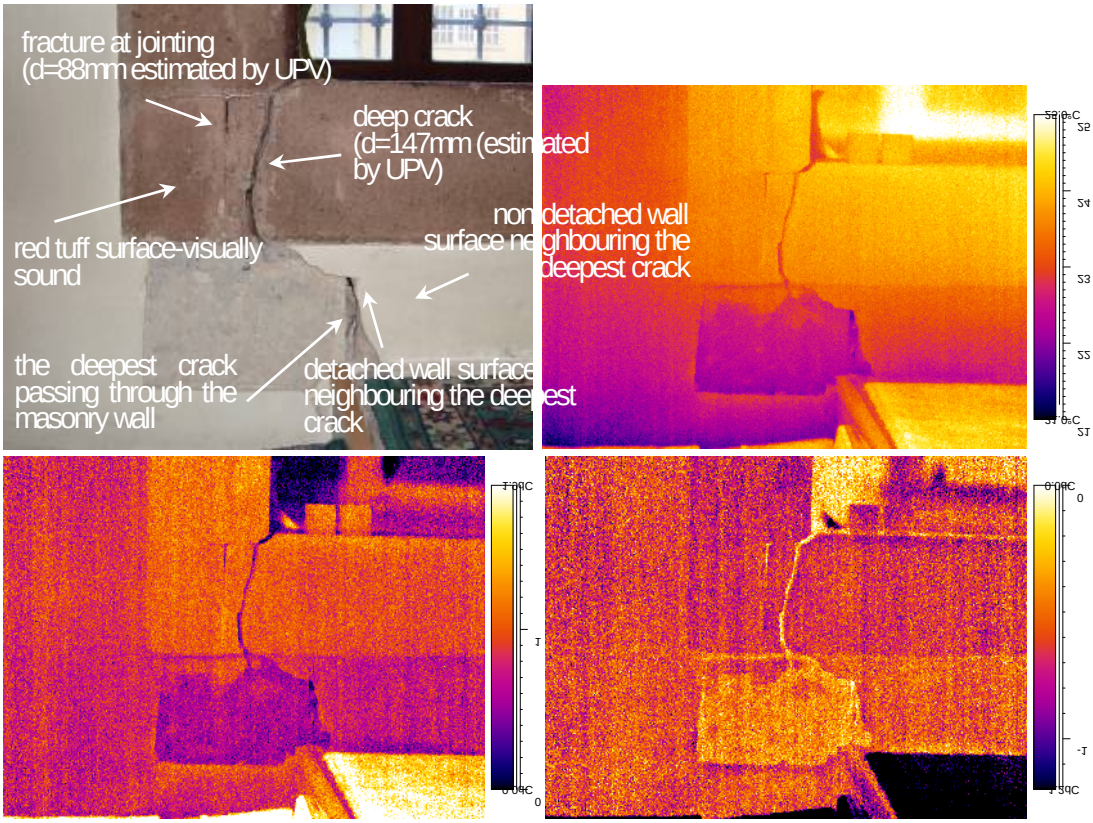

Figure 4.14 Partial view from the left bottom of window opening at the east side of the structure (at the top left); its IR image (at the top right); and the differential IR images of the heating period (at the left bottom) and the cooling period (at the right bottom).

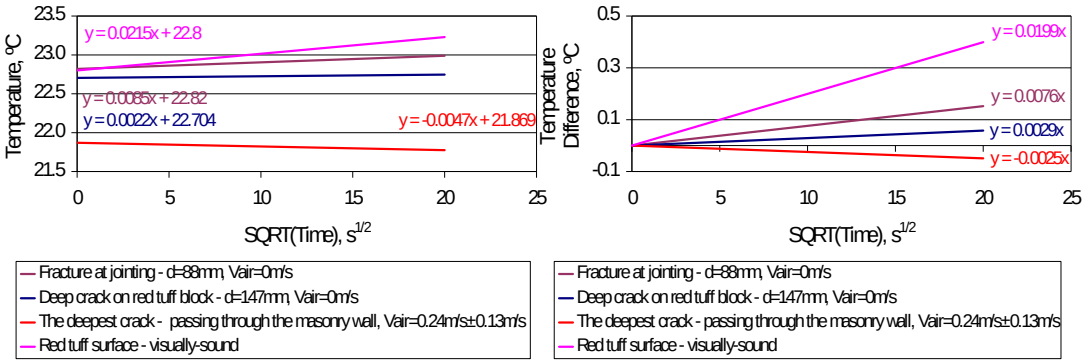

Figure 4.15 The linear fitting of surface temperatures and temperature difference versus square root of time during the heating period for the case defined in Figure 4.14: The deep cracks had noticeably slower rate of warming up than the sound red tuff while the deepest crack allowing air leakage through its cavity had the coldest surface temperature and cooled down under the exposure of heating up process.

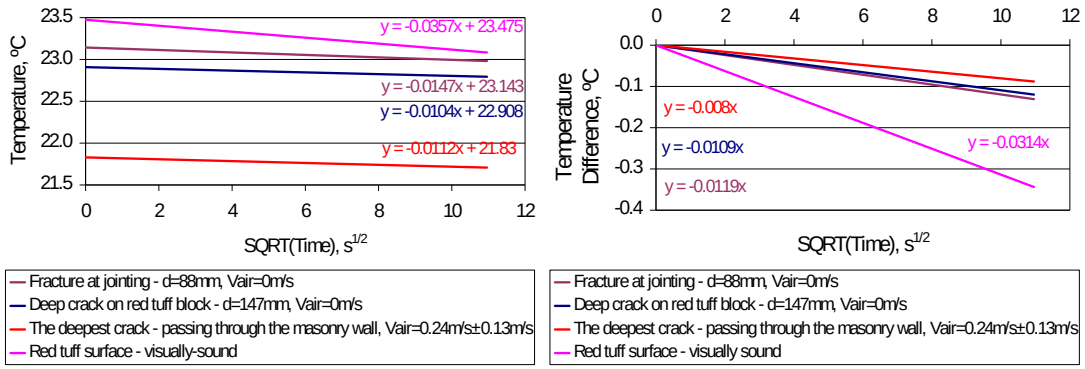

Figure 4. 16 The linear fitting of surface temperatures and temperature difference versus square root of time during the cooling period for the case defined in Figure 4.14: The deep cracks had noticeably slower rate of cooling down than the sound red tuff while the deepest crack allowing air leakage through its cavity had the coldest surface temperature and the slowest rate of cooling down.

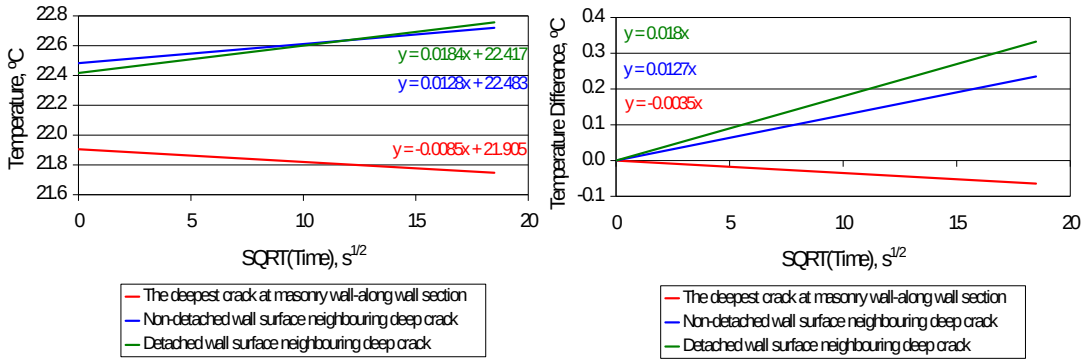

Figure 4.17 The linear fitting of surface temperatures and temperature difference versus square root of time during the heating period for the case defined in Figure 4.14: The thermal behaviour of the deepest crack at the masonry neighbouring detachments was in contrast to the superficial cracks neighbouring detachments (compare with Figure 4.12). The deepest crack had the coldest surface temperature and slightly cooled down under the exposure of heating.

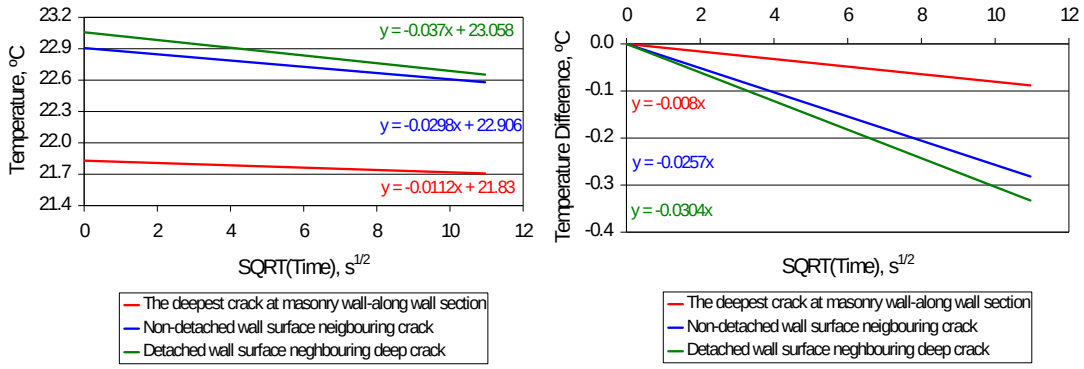

Figure 4.18 The linear fitting of surface temperatures and temperature difference versus square root of time during the cooling period for the case defined in Figure 4.14: The thermal behaviour of the deepest crack at the masonry neighbouring detachments was in contrast to the superficial cracks neighbouring detachments (compare with Figure 4.12). The deepest crack had the coldest surface temperature with the slowest rate of cooling down among neighbouring all wall surfaces.

– Thermal monitoring of the deepest crack, deep crack and detached surfaces together with non-detached surface were summarized in Figures 4.19-4.23. IR sequences were taken at the ambient conditions of 20.4ºC and 50%RH during the heating period of 463s when the wall surface was uniformly heated with halogen lamp and then during the cooling period of 524s after the halogen lamp was turned off. The linear fitting of surface temperatures versus square root of time

and temperature differences versus square root of time during the first 288s of heating period and during the first 362s of cooling period were given in Figures 4.20-4.23. The results showed that the deepest crack allowing air leakage through its cavity was slightly cooled down during the heating period with the rate of -0.0018. The deepest crack also presented the slowest rate of cooling down during the cooling period with the rate of -0.0098. The deep crack had slower warming up rates than the visually-sound plastic painted wall surface. The warming up rates of deep crack and visually-sound surfaces were 0.0326 and 0.0592, respectively while the cooling down rates of the same surfaces were -0.0374 and -0.0621, respectively. The detached surfaces were detected as the warmest parts of selected area with the fastest warming up and cooling down rates (Figures 4.20 and 4.21). These detached surfaces were warmer than the visually-sound plastic painted wall surface with a temperature difference of 0.73ºC and had the warming up and cooling down rates of 0.0658 and -0.069, respectively.

The area between the arch of first layer window and the decoratively painted wall surface above the first layer window was seen visually-sound although thermal analysis signalled the crack on the examined surface due to the similar thermal behaviours of the deepest crack and this examined surface under the exposure of warming up and cooling down conditions. This non-visible deepest crack behind plaster had slightly faster warming up and cooling down rates than those of the deepest crack. Non-visible deepest crack had the warming up and cooling down rates of 0.0133 and -0.0149, respectively (Figures 4.20 and 4.21).

The detached surfaces could be differentiated from each other as well (Figures 4.22 and 4.23). All detachments were warmer than the visually-sound plastic painted wall surface and had the faster warming up and cooling down rates than the visually-sound surface. Detached decoratively painted wall surface and detached plaster surface neighbouring non-visible crack exhibited similar thermal response to the warming up conditions with the rates of 0.0788 and 0.0672, respectively. They also exhibited similar thermal response to the cooling down

conditions with the rates of -0.0842 and -0.0674, respectively. Non-visible detachment behind the plaster, on the other hand, was the warmest surface with the fastest rates of warming up and cooling down. This non-visible detachment was warmer than the visually-sound plastic painted wall surface with a temperature difference of 1.26ºC and had the warming up and cooling down rates of 0.1551 and -0.1921, respectively.

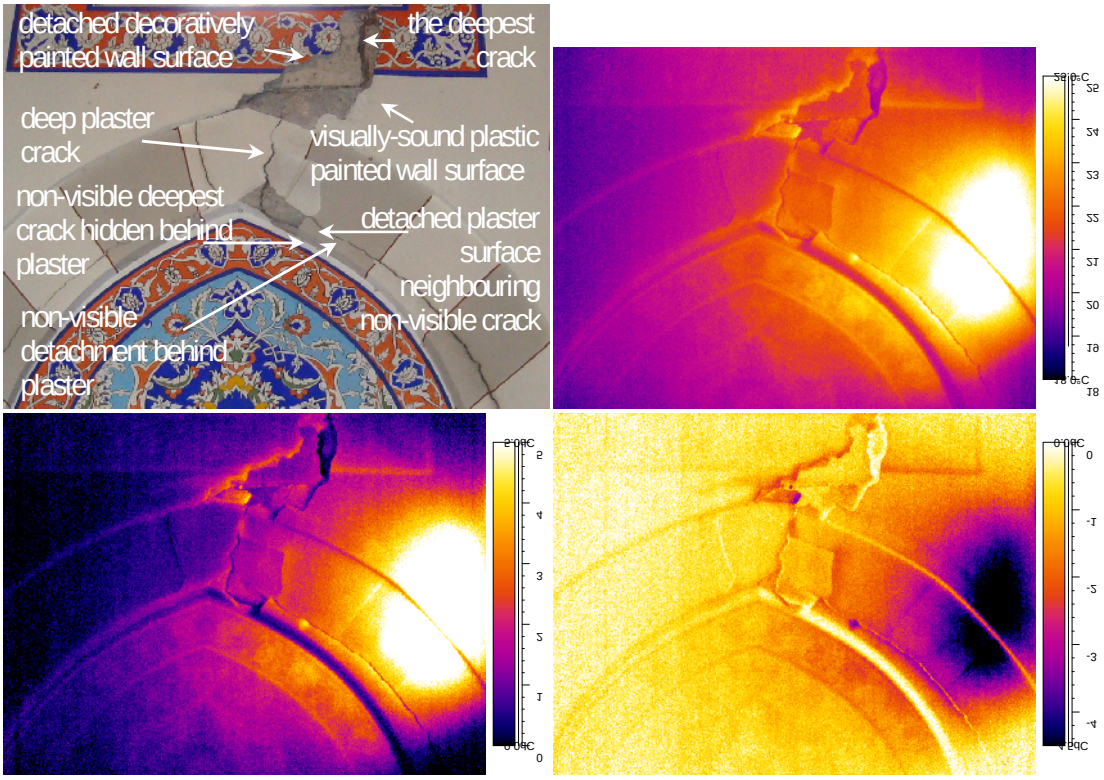

Figure 4.19 Partial view from a window arch located at the east of the structure (at the top left), its IR image (at the top right); and the differential IR images of the heating period (at the left bottom) and the cooling period (at the right bottom).

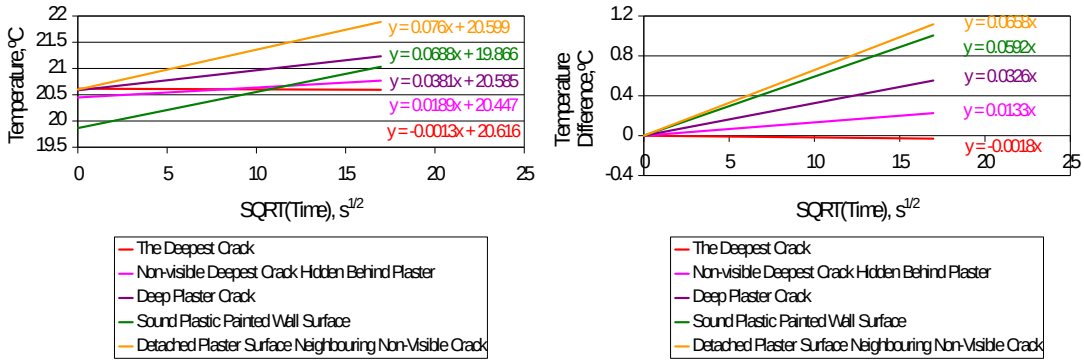

Figure 4.20 The linear fitting of surface temperatures and temperature difference versus square root of time during the heating period for the case defined in Figure 4.19: The detached surfaces warmed up the fastest while the warming rates of cracks were slower than the visually-sound surface. Deep plaster crack warmed up faster than the deepest cracks and the deepest crack slightly-cooled down under the exposure of heating up process.

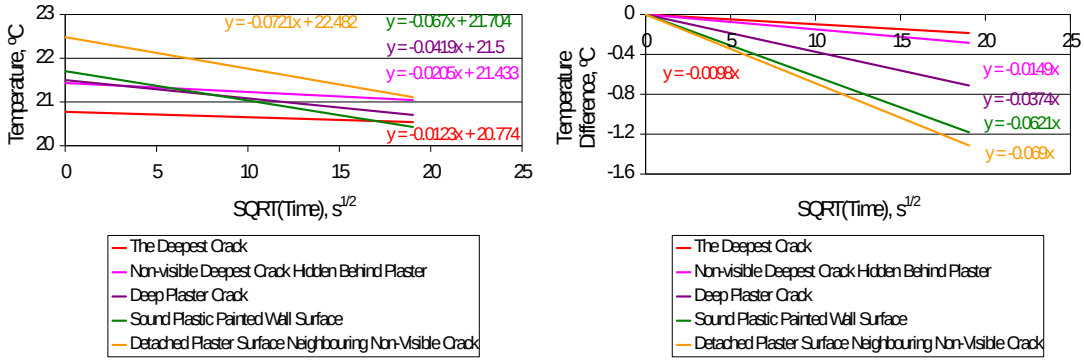

Figure 4.21 The linear fitting of surface temperatures and temperature difference versus square root of time during the cooling period for the case defined in Figure 4.19: The detached surfaces cooled down the fastest while the cooling down rates of cracks were slower than the visually-sound surface. Deep plaster crack cooled down faster than the deepest cracks while the deepest crack had the slowest cooled down rate.

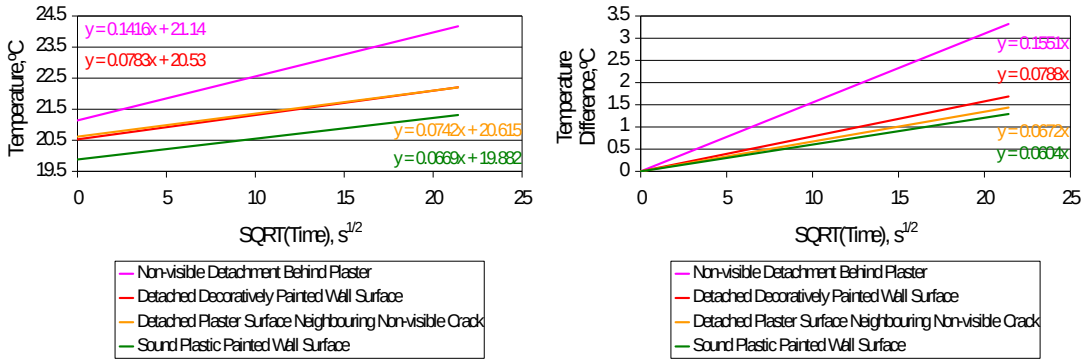

Figure 4.22 The linear fitting of surface temperatures and temperature difference versus square root of time during the heating period for the case defined in Figure 4.19: The initial temperatures and warming up rates of detached surfaces were higher than the visually-sound plastic painted wall surface. Non-visible detachment was the warmest surface with the fastest warming up rate.

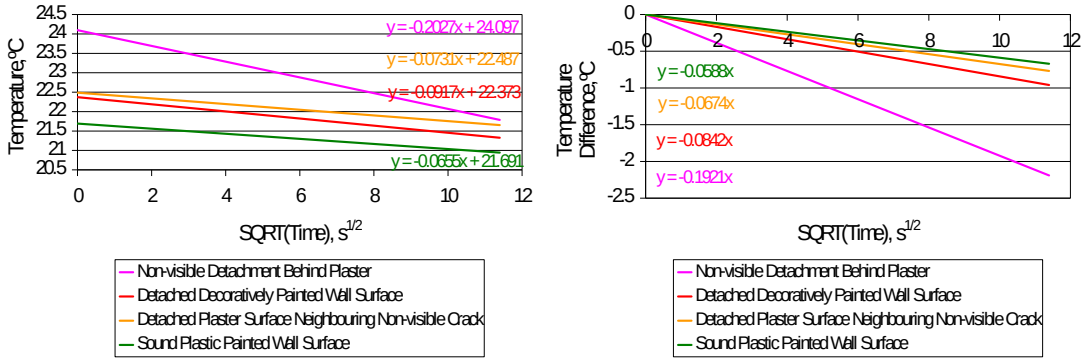

Figure 4.23 The linear fitting of surface temperatures and temperature difference versus square root of time during the cooling period for the case defined in Figure 4.19: The initial temperatures and cooling down rates of detached surfaces were higher than the visually-sound plastic painted wall surface. Non-visible detachment was the warmest surface with the fastest cooling down rate.

– The data on the warming up (R_W) and cooling down rates (R_C) for each crack/defect were summarized in Table 4.1, Figure 4.24 and 4.25. When the rates of defects were compared with the rates of visually-sound surfaces, it was found that plaster detachment had the highest ratio for warming up and cooling down conditions. The cracks, on the other hand, had the slowest ratios (Figure 4.24). Non-visible deepest crack hidden behind the plaster layer and the deepest crack presented exactly the same thermal responses under the exposure of cooling

condition and the ratio between the R_W of non-visible deepest crack hidden behind the plaster layer and the deepest crack to the R_W of sound surface were similar while the ratio between the R_W (or R_C) of plaster detachment to the R_W (or R_C) of sound surface was noticeably higher (Figure 4.25).

Table 4.1 The warming up and cooling down rates for the superficial and deep cracks and visually-sound jointing mortars as well as their comparison with the rates of the visually-sound red tuff surface.

Defect/Jointing	$\mathbf{R_{W\text{-}DEFECT}}$	$\mathbf{\frac{R_{W\text{-}DEFECT}}{R_{W\text{-}SOUND}}}$	$\mathbf{R_{C\text{-}DEFECT}}$	$\mathbf{\frac{R_{C\text{-}DEFECT}}{R_{C\text{-}SOUND}}}$
Superficial crack associating with plaster detachment	0.0292	1.0618	-0.0262	1.1293
Plaster detachment	0.0364	1.3236	-0.0335	1.4439
R_{SOUND} - Plaster covered masonry wall	0.0275		-0.0232	
Fracture at jointing - d=88mm	0.0085	0.3953	-0.0147	0.4117
Crack on red tuff - d=147mm	0.0022	0.1023	-0.0104	0.2913
Deepest crack with air flow	-0.0047	-0.2186	-0.0112	0.3137
R_{SOUND} – Red tuff	0.0215		-0.0357	
Vertical jointing between red tuff blocks	0.0232	0.9914	-0.0267	1.0595
Horizontal jointing between red tuff blocks	0.0234	1.0000	-0.0246	0.9761
R_{SOUND} – Red tuff	0.0234		-0.0252	
Non-visible deepest crack hidden behind plaster	0.0189	0.2747	-0.0205	0.3059
R_{SOUND} - Plaster covered masonry wall	0.0688		-0.067	

$R_{W\text{-}DEFECT}$ - **R**ate of **W**arming up for the **DEFECT; $R_{C\text{-}DEFECT}$** - **R**ate of **C**ooling down for the **DEFECT; R_{SOUND}** - Reference **R**ate for the **SOUND** surface

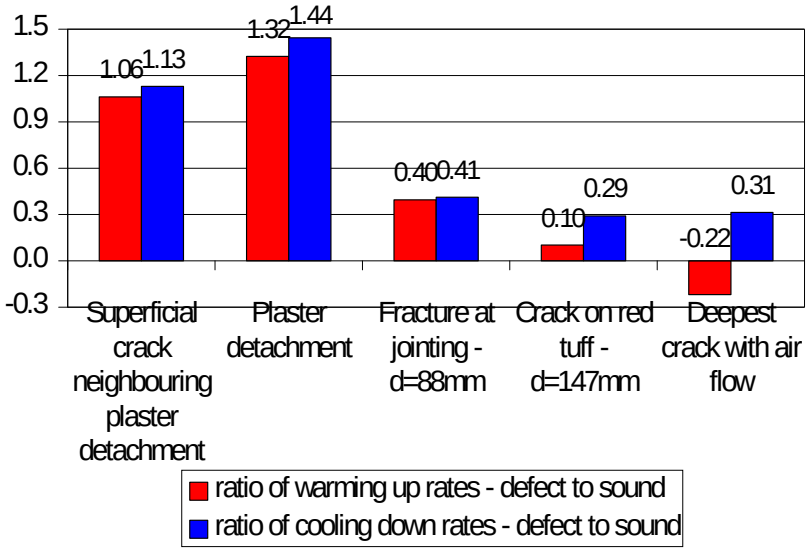

Figure 4.24 The ratios between the R_W (or R_C) of crack/defect to the R_W (or R_C) of sound surface: Superficial and deep cracks had different thermal responses to exposed conditions which made them distinguishable by QIRT analyses.

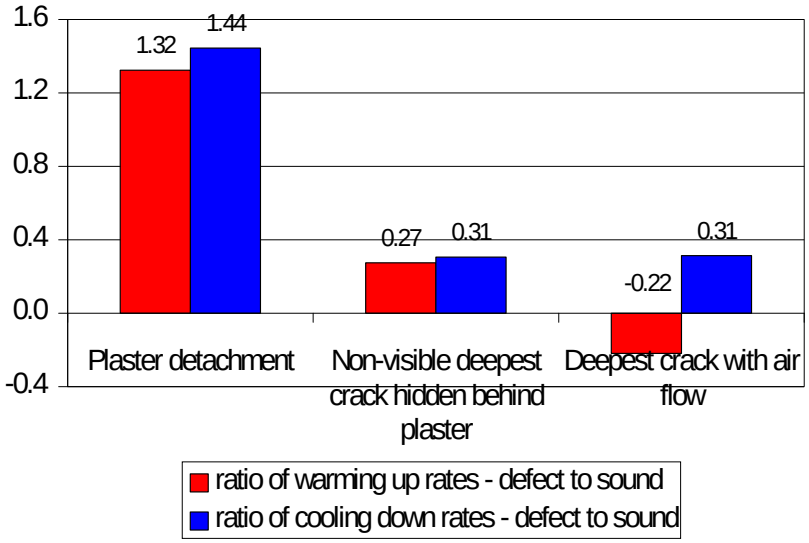

Figure 4.25 The ratios between the R_W (or R_C) of crack/defect to the R_W (or R_C) of sound surface: Non-visible deepest crack had similar thermal responses with the deepest one especially in cooling period, while thermal behaviour of superficial crack and deepest cracks were totally different.

The results of *in-situ* infrared thermography survey related to the analyses about the compatibility of recent plaster repairs were summarized below:

- The detachment on recent wall painting at the west side of building was examined during the cooling condition. IR sequences were taken at the ambient conditions of 5.7ºC and 49%RH during the cooling period of 283s after the wall surface was uniformly heated with a hair dryer. The linear fitting of surface temperatures versus time during the cooling period was given in Figure 4.26. The results exhibited that the detachment on renewed wall painting was easily detected in the IR image as a warmer patch which could not be visually observed. The detached surfaces seemed to get colder faster than the non-detached surfaces while the fastest cooling was observed at the edge of the detachment. The entire wall surfaces under examination were below the ambient temperature close to the wall surface while the wall surface coated with plastic paint having the coldest surface temperature distribution.

- The wall surface of second floor at the north side painted with recent plaster repairs was analysed during the heating and cooling conditions (Figure 4.27). IR sequences were taken at the ambient conditions of 20.6ºC and 55%RH during the heating period of 735s when the wall surface was uniformly heated with halogen lamp and then during the cooling period of 456s after the halogen lamp was turned off. The results showed that heterogeneous temperature distribution of wall surfaces coated with plastic painting was noticed easily in IR images. That signalled the incompatibility of recent repairs. Superficial cracks and the detached plaster surfaces were detected easily in IR image as warmer patches while it was not possible to notice all detaching parts clearly by eye. Temperature distributions of visually-sound and deteriorated wall surfaces coated with plastic paint were presented with the histograms which were taken from the differential IR image taken at 456. second of the cooling period (Figure 4.28). Histograms showed that deteriorated surfaces cooled down faster than the visually-sound wall surfaces.

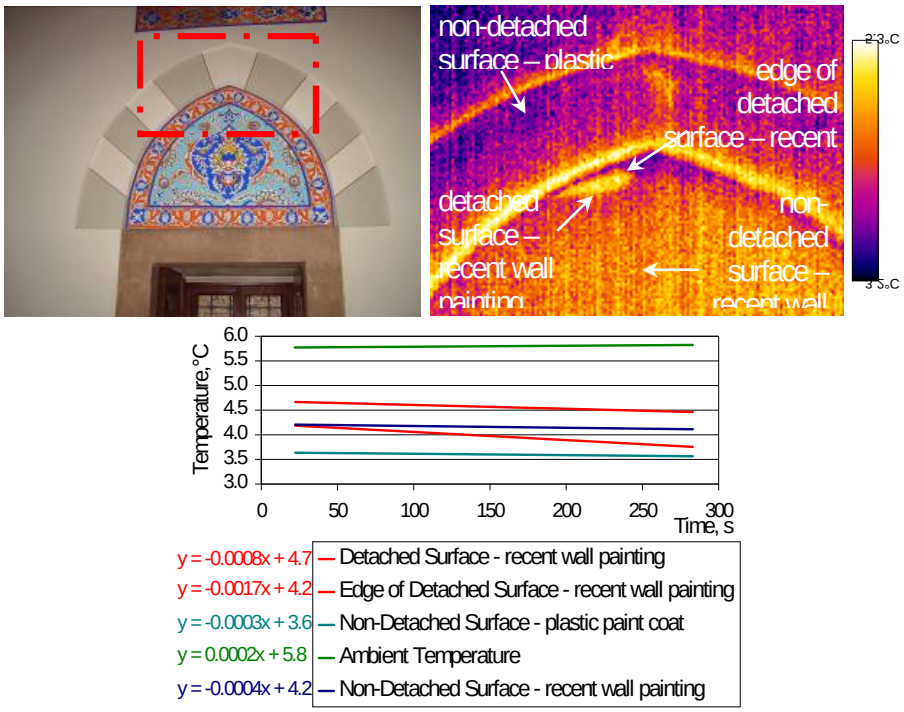

Figure 4.26 Partial view from a window at the west side of the structure (at the top left), the IR image of selected region (at the top right), and the surface temperature curves versus time during the cooling period (at the bottom): Non-visible detached surface, which was detected in the IR image as a warmer patch, cooled down faster than the non-detached surfaces while the fastest cooling was observed at the edge of the detachment. The wall surfaces were colder than the ambient temperature while the plastic paint coated surfaces were the coldest.

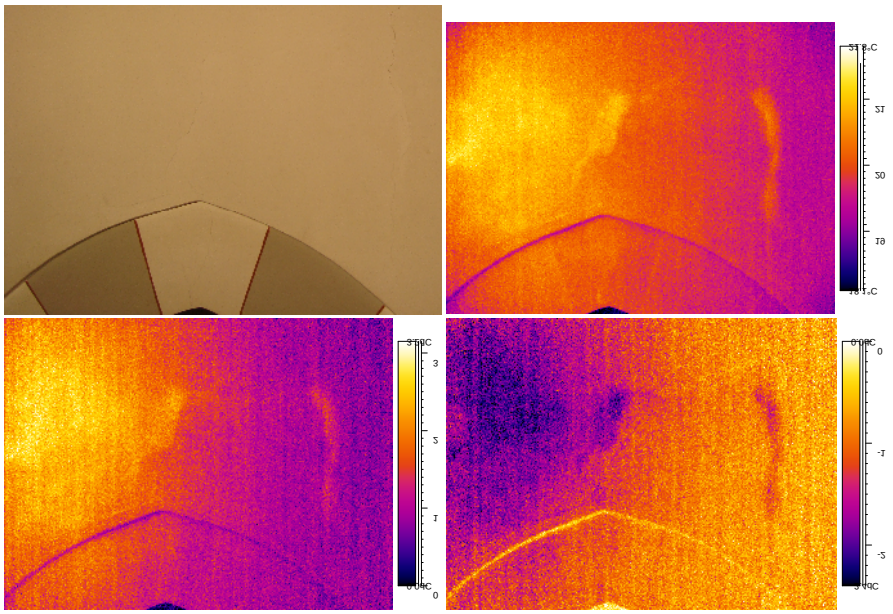

Figure 4.27 Partial view from the wall surface of second floor at the north side of the structure (at the top left), its IR image (at the top right); and the differential IR images of the heating period (at the left bottom) and the cooling period (at the right bottom).

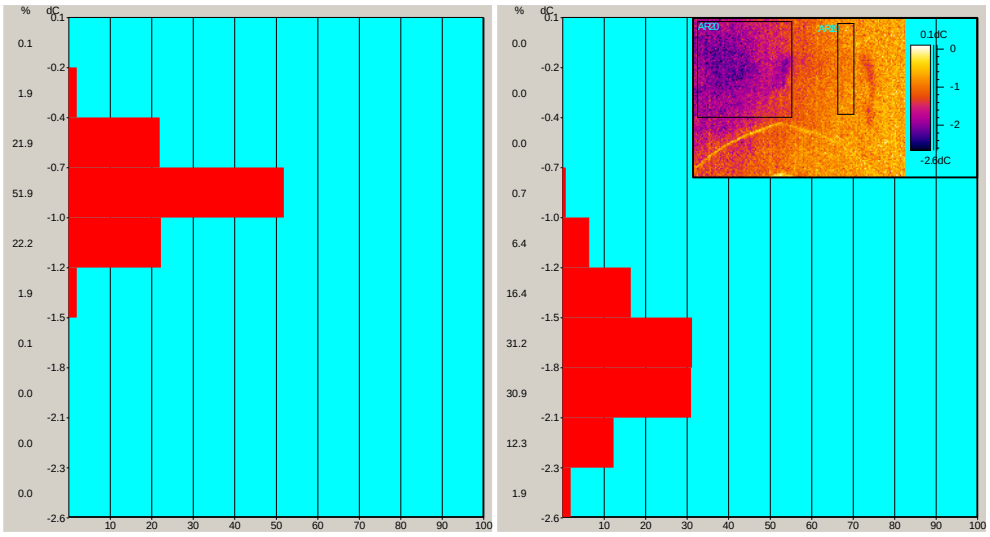

Figure 4.28 Histogram views of visually-sound wall surface (at the left) and deteriorated surface (at the right) taken from the differential IR image of cooling period for the case defined in Figure 4.27: Heterogeneous temperature distribution of deteriorated surface was easily observed in IR images. Deteriorated wall surfaces cooled down faster than the visually-sound wall surfaces.

The results of *in-situ* infrared thermography survey related to the analyses of historic wall painting layer and historic plaster layer(s) hidden behind the wall painting recently done were summarized below:

– Single IR images were taken from the decoratively painted wall surfaces above the first layer windows at north wall at the interior climatic conditions of 7.2°C and 51%RH and outside climatic conditions of 2.5°C and 62.5%RH (Figures 4.29 and 4.30). It was found that decoratively painted wall surfaces were warmer than the surfaces coated with plastic paint with +0.6°C temperature difference. In Figure 4.30, the surface temperature data for the fair-faced red tuff, decoratively-painted and plastic paint wall surfaces together with the inside air temperature close to the surface were extracted from several IR images scanning the north wall entirely. According to the results of that scanning, all north wall was colder than the ambient temperature. Wall surfaces coated with plastic paint were the coldest surfaces, having -2.6°C temperature difference with the ambient temperature close to wall surface. Red tuff surfaces, on the other hand, were the warmest areas, with a temperature difference of -1.5°C.

– The sequential IR imaging of the old and recent wall painting surfaces on the south wall were taken during the cooling period of 245s in order to determine the thermal responses of old and recent wall paintings. It was found that the old wall painting surface cooled down faster than the recent wall painting surface (Figure 4.31).

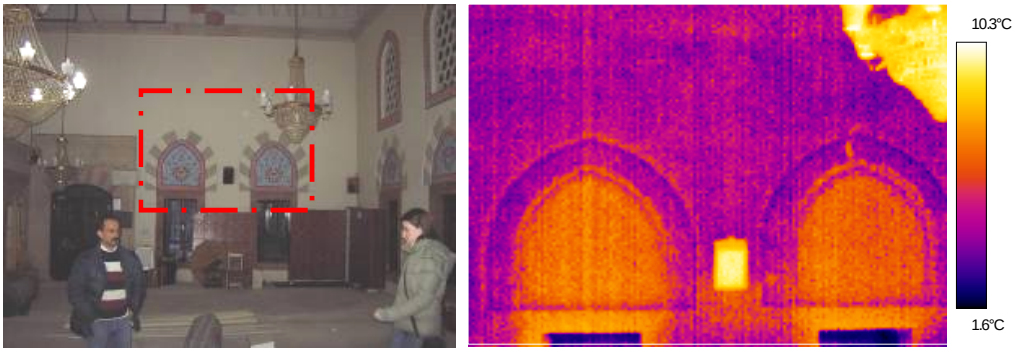

Figure 4.29 Partial view from the north wall of the structure (at the left) and the IR image of the selected region: The decoratively-painted wall surfaces were slightly warmer than the plastered wall surfaces coated with white plastic paint

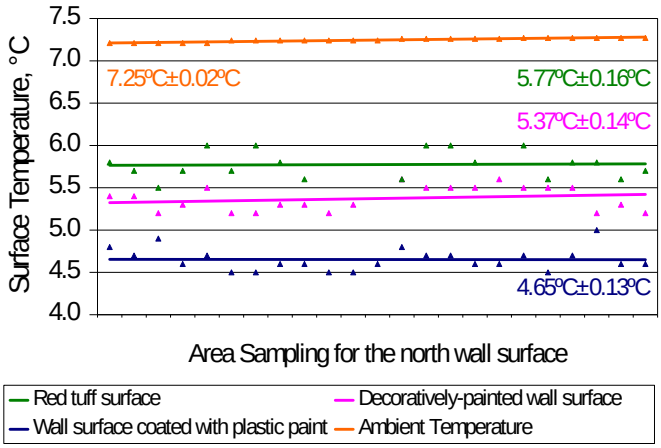

Figure 4.30 The surface temperature plot of north wall showing that the overall wall surfaces were colder than the inside ambient temperature while the ones coated with plastic paint were the coldest areas while the red tuff surfaces were the warmest areas.

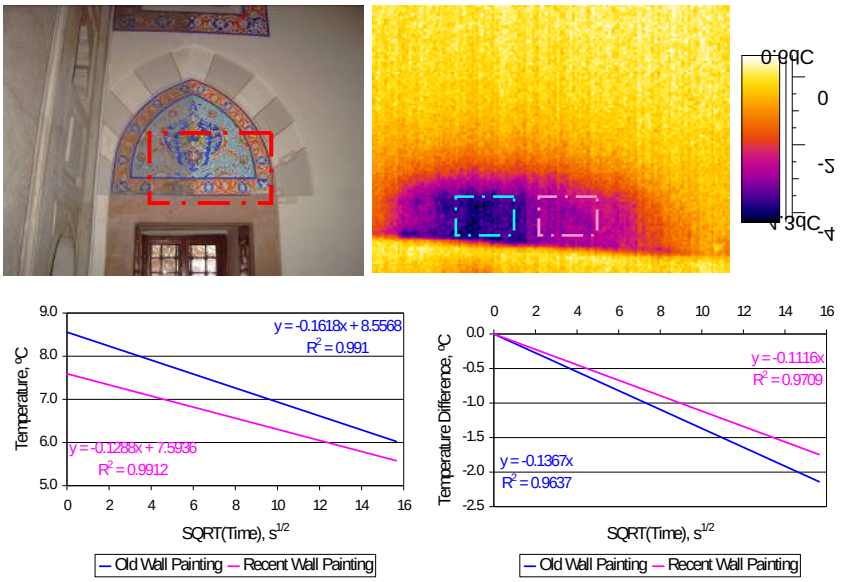

Figure 4.31 Partial view of old and recent wall paintings on the south wall (at the top left), the differential IR image of the selected region during the cooling period (at the top right), the linear fitting of surface temperatures and temperature difference versus square root of time during the cooling period (at the bottom): the old wall painting surfaces cooled down faster than the recent wall painting surfaces.

The results of *in-situ* infrared thermography survey related to the analyses of thermal inertia characteristics for stones were summarized below:

– Thermal behaviours of yellowish, white and red tuff blocks used at exterior wall and arch surfaces were determined by the sequential IR imaging under exposure of solar radiation in damp condition (Figures 4.32 and 4.34). Sequential IR images were taken at the ambient conditions of 28.6 ºC and 28%RH during the heating period of 271s when the wall surface was uniformly heated by solar radiation for the case defined in Figure 4.32. Sequential IR images for the case defined in Figure 4.34, on the other hand, were taken at the ambient conditions of 29.4 ºC and 27%RH during the heating period of 291s when the wall surface was uniformly heated by solar radiation. The results exhibited that the red tuff blocks at arches had the warmest surface temperatures and they were determined to warm up faster than the yellowish and white tuffs. The yellowish tuff of masonry wall had similar warming up rates with the ones on arches (Figures 4.33 and 4.35). White tuffs, on the other hand, had the coldest surface temperatures. They

were colder than the ambient temperature with the warming up rate being slower than those of yellowish and red tuffs. That might be due to the presence of moisture in tuffs in different ranges. The repaired tuff with cement-based coat presented different thermal response to the warming up condition than the tuffs. Although the initial real surface temperatures of repaired tuff and yellowish one were similar, the repaired tuff with cement-based coat warmed up faster than the yellowish tuff (Figure 4.35).

– Visually sound and deteriorated andesite stones at the basement of structure were examined under exposure of solar radiation when the ambient conditions were 28.9 ºC and 28%RH. The results were given in the form of histogram views, showing the visually sound and deteriorated andesite stones in the first and second courses above ground level (Figure 4.36 and 4.37). For the first course above the ground level, an even distribution of surface temperatures was observed on the visually-sound andesite, having the surface temperature in the range of 30.9°C and 32.0°C with an average of 31.3°C±0.2°C. On the other hand, andesite which was deteriorated in the forms of material loss and detachments in the first course above ground level showed heterogeneous temperature distribution with the surface temperature in the range of 29.0°C and 34.7°C with an average of 30.9°C±0.7°C (Figure 4.36). For the second course above the ground level, an even distribution of surface temperatures was observed on the visually-sound andesite, having the surface temperature in the range of 31.8ºC and 33.4ºC with an average of 32.6ºC±0.2ºC. On the other hand, andesite which was deteriorated in the forms of material loss and detachments in the second course above ground level showed heterogeneous temperature distribution with the surface temperature in the range of 30.5ºC and 38.5ºC with an average of 33.5ºC±1.3ºC (Figure 4.37). the results showed that andesite stone which was deteriorated in the form of material loss and detachment had heterogeneous temperature distribution. Additionally, visually-sound and deteriorated andesites in the second course were warmer than the andesite stones in the first course above ground level.

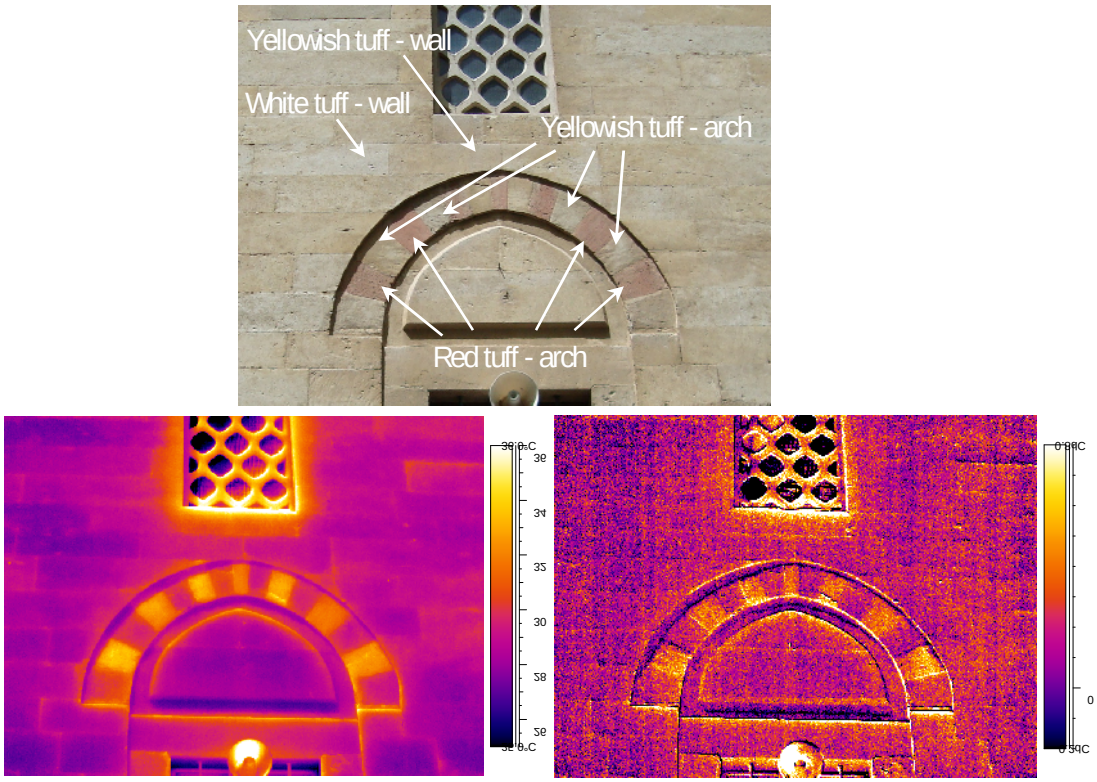

Figure 4.32 Partial view of exterior wall surfaces at south side (at the top), its IR image (at the left bottom); and the differential IR image of the heating period (at the right bottom).

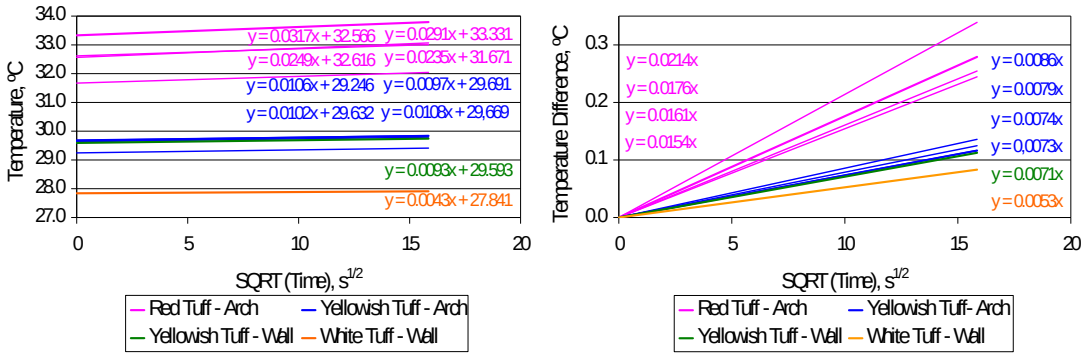

Figure 4.33 The linear fitting of surface temperatures and temperature differences versus square root of time during the heating period for the case defined in Figure 4.32: The red tuffs had the warmest surfaces with the fastest warming up rates. The white tuff had coldest surface with the slowest heating up rate. Yellowish tuffs used on wall surfaces and on arches exhibited similar warming up rates.

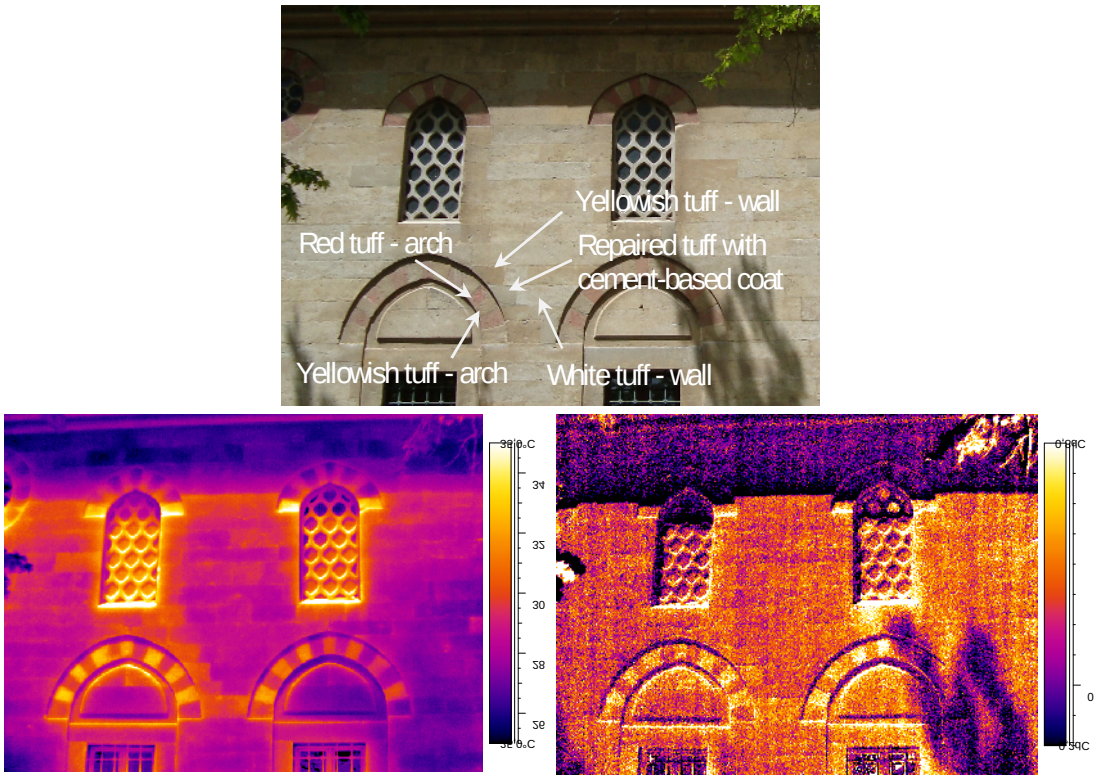

Figure 4.34 Partial view of exterior wall surfaces at south side (at the top), its IR image (at the left bottom); and the differential IR image of the heating period (at the right bottom).

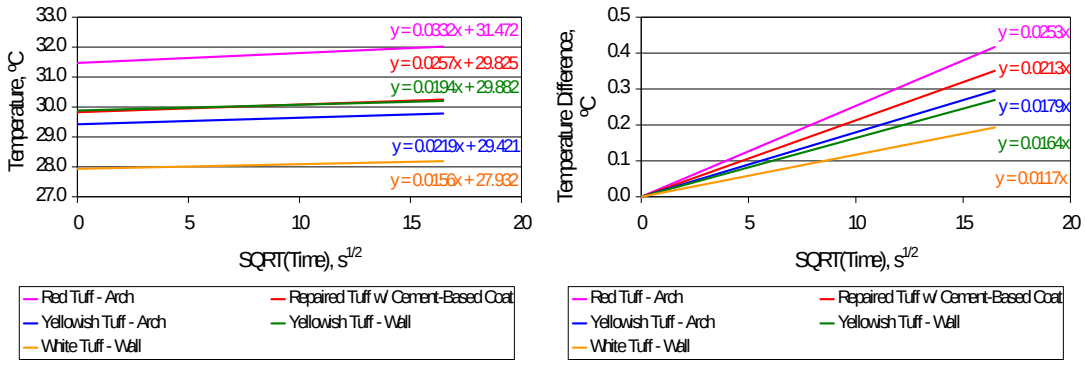

Figure 4.35 The linear fitting of surface temperatures and temperature differences versus square root of time during the heating period for the case defined in Figure 4.32: The red tuff had the warmest surface with the fastest warming up rate. The white tuff had coldest surface with the slowest heating up rate. Repaired tuff with cement-based coat had faster warming up rate than the yellowish and white tuffs.

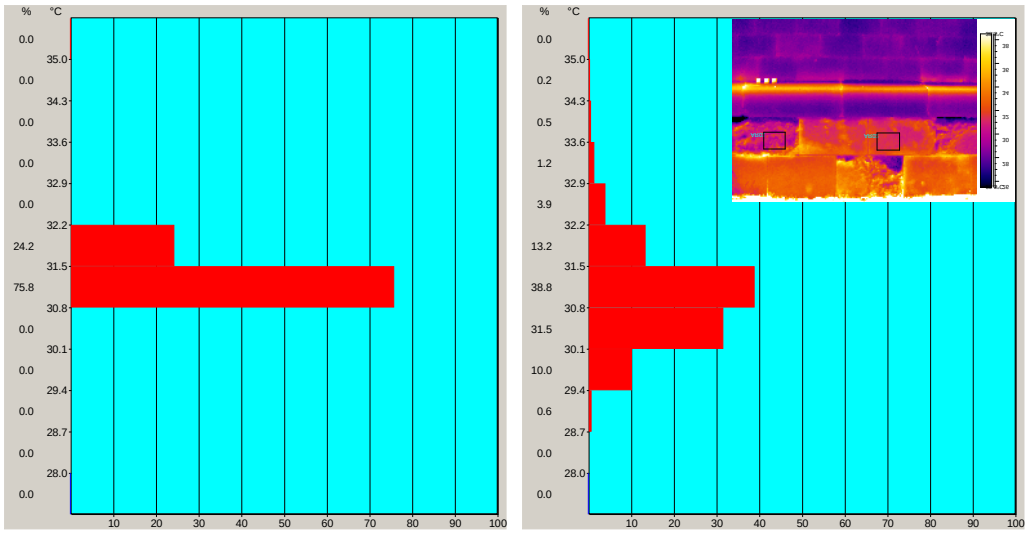

Figure 4.36 Histogram views of visually-sound andesite masonry located in the first course above ground level (at the left) and deteriorated surface in the first course (at the right): Deteriorated surface had heterogeneous temperature distribution.

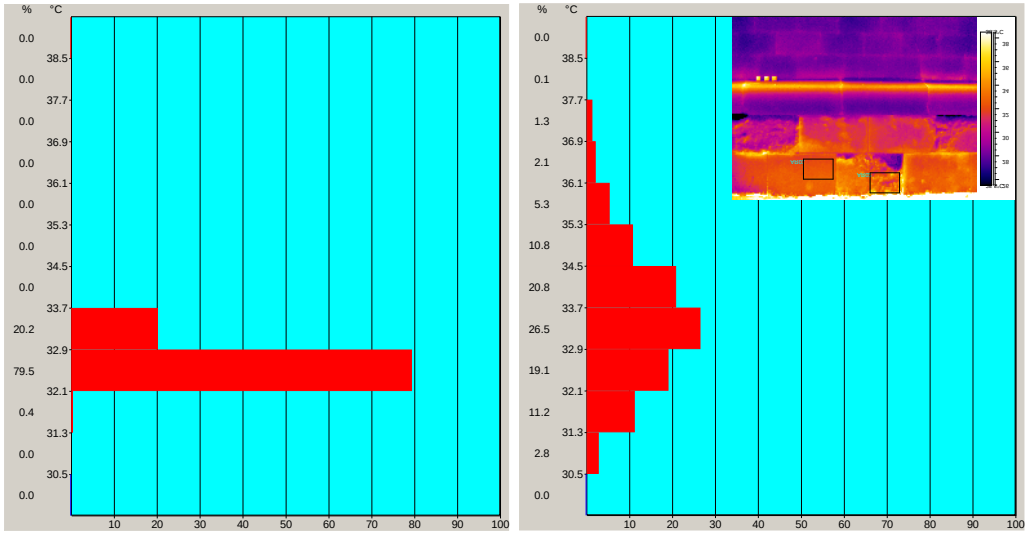

Figure 4.37 Histogram views of visually-sound andesite masonry located in the second course above ground level (at the left) and deteriorated surface in the second course (at the right): Deteriorated surface had heterogeneous temperature distribution.

– Surface temperatures of yellowish tuff on wall, red tuff at the arch and repaired tuff with cement-based coat were examined in individual IR images taken during the warming period of daytime at the ambient conditions of 12.4 ºC and 48%RH (Figure 4.38). It was found that repaired tuffs with cement-based coat were

warmer than the ambient temperature and visually-sound yellowish tuff wall surfaces with temperature differences of +6.65ºC and +2.5ºC, respectively, that made the detached surfaces clearly visible in IR images although it was not easy to differentiate the repaired tuff surfaces visually by eye. Yellowish and red tuffs could also be distinguished easily due to their different thermal behaviours. Red tuff surface was warmer than ambient temperature with +7.6ºC temperature difference while yellowish tuff on wall was +4.15ºC warmer than the ambient temperature.

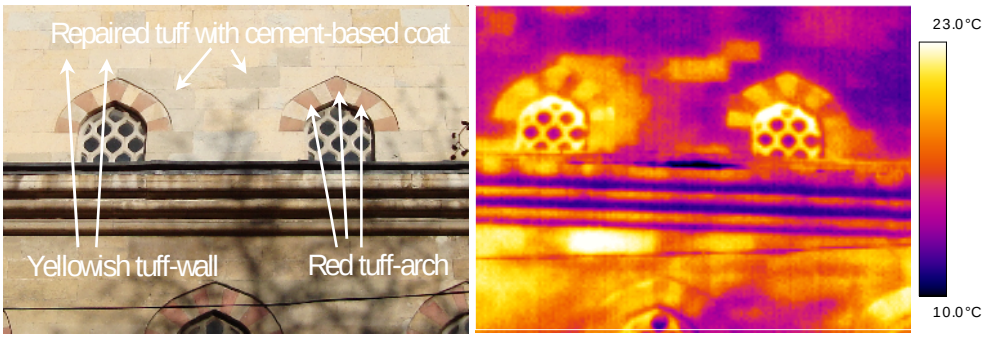

Figure 4.38 Partial view of exterior wall surfaces at west side (at the left) and its IR image (at left bottom): Different stone types were easily detected in IR images. Red tuff at the arch and repaired tuff with cement-based coat were warmer than the yellowish tuff used on wall surfaces when all surface temperatures were above the ambient temperature.

– Thermal responses of minaret wall surface on south façade were detected in IR image after the preliminary wetting by light summer rainfall (Figure 4.39). IR image was taken at the exterior boundary conditions of 30ºC and 21%RH. It was found that the visually sound yellowish tuff wall surfaces were -1.18ºC±0.34ºC colder than the ambient temperature due to the slightly damp tuff surfaces. The wall surfaces washed by the rainwater discharged directly from the gutters were the coldest surfaces in the IR images, being colder than the ambient temperature with a temperature difference of -6.75ºC±2.04ºC while these damp surfaces covered with biological growth were observed to be warmer than visually-sound tuff surfaces with a temperature difference of +0.7ºC while being still colder than the ambient temperature.

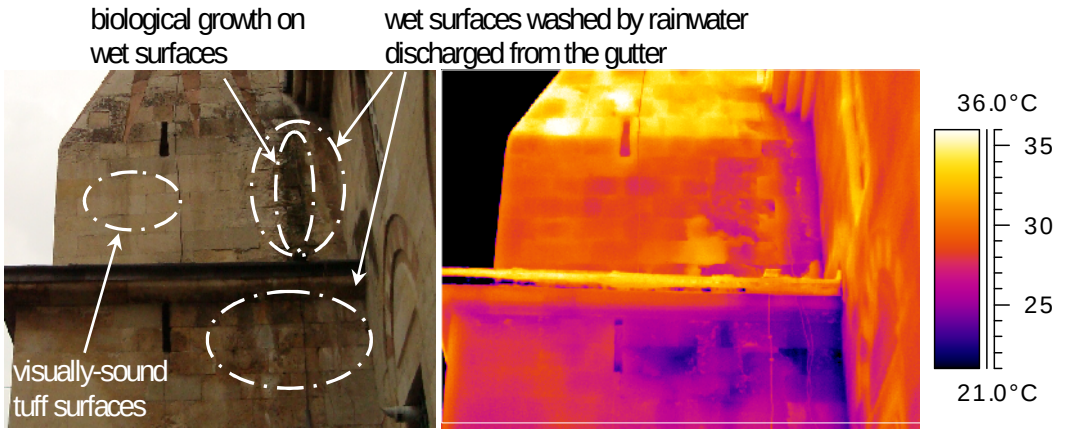

Figure 4.39 Partial view of exterior wall surface at the south facade of minaret (at the left) and its IR image (at the right): The visually-sound tuff surfaces were colder than the ambient temperature. The damp surfaces washed by rainwater were the coldest areas while biological growths on these damp zones were warmer than visually-sound tuff surfaces.

4.3 Quantitative Analyses of *In-situ* Ultrasonic Testing

The results of ultrasonic testing were summarized in Table 4.2 and Figure 4.40, together with the close views of cracks/jointings examined. For the visually-sound red tuffs, the indirect ultrasonic velocity (UPV_{IND-T}) was determined to be in the range of 826m/s and 1026m/s with an average of 944m/s±83m/s and slope of the regression line (S_T) was determined to be in the range 0.98 and 1.23 with an average of 1.08±0.13 (Table 4.2). The jointing detail between the red tuff blocks decreased the indirect ultrasonic velocity (UPV_{IND-TM}) to 374m/s±23m/s and increased the slope of regression line (S_{TM}) to 3.38±0.23 (Table 4.2). Those values were accepted as the reference UPV data in indirect transmission mode for the sound red tuff individually and together with jointing mortar.

According to the spot readings by vernier calliper, the depths of fracture at jointing and deep crack on red tuff were measured in the range of 25.8mm-42.6mm and 32.5mm-75.7mm, respectively. However, the depths were calculated to be 88mm for fracture at jointing and 147mm for deep crack on red tuff by using UPV data (Table 4.2). Those results exhibited that cracks were deeper than depth measurements taken

by the vernier calliper and the UPV measurements in indirect mode were more accurate for depth assessment of cracks.

Table 4.2 The results of *in-situ* ultrasonic testing conducted on red tuff and jointing mortar surfaces in terms of ultrasonic velocity, slope of regression line and depth of discontinuity/crack in stone.

Definition of defect	UPV_{IND-T} m s^{-1}	S_T	UPV_{IND-TM} m s^{-1}	S_{TM}	S_D	D_{UPV} mm	$D_{CALIPER}$ mm
Proper adhesion through jointing	1026	0.98	387	3.60	-	-	-
Non-visible discontinuity through the jointing	860	1.23	348	3.40	8.97	86	-
Deep crack on red tuff block	826	1.19	335	4.42	6.30	147	32.5-75.7
Fracture at jointing	946	1.03	387	3.14	6.55	88	25.8-42.6

UPV_{IND-T} -The **IND**irect **UPV** measurement for the red **T**uff; **UPV_{IND-TM}** -The **IND**irect **UPV** measurement for the red **T**uff and **M**ortar; **S_T** -The **S**lope of regression line for RED **T**uff; **S_{TM}** -The **S**lope of regression line for red **T**uff and **M**ortar; **S_D** -The **S**lope of regression line for **D**efect; **D_{UPV}** - The **D**epth of crack/discontinuity calculated by using **UPV** measurements; **$D_{CALIPER}$** -The **D**epth of crack/discontinuity measured by vernier **CALIPER**

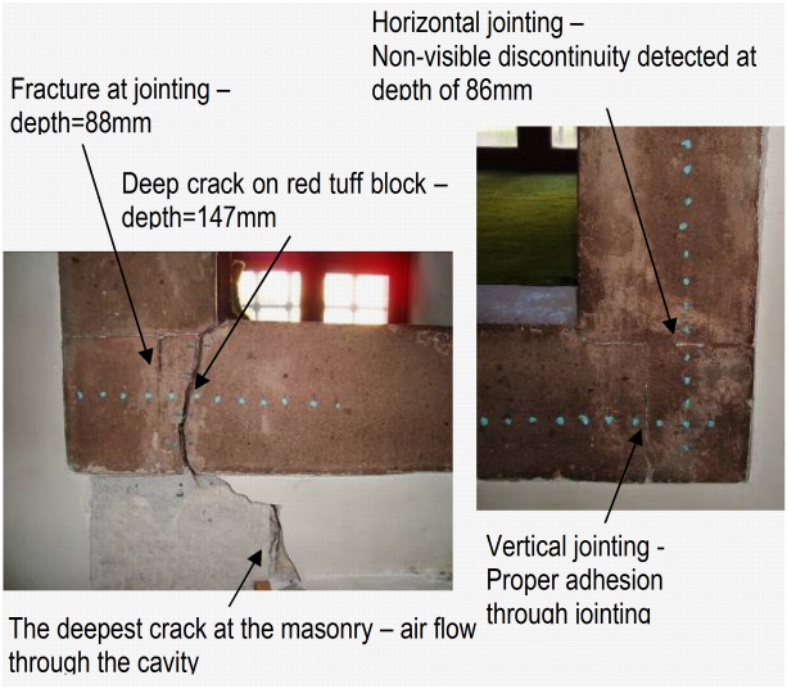

Figure 4.40 The close views of structural cracks and jointings on red tuff blocks at the left and right bottom corners of window niche examined *in-situ* by using QIRT and ultrasonic testing.

The transit time readings taken on the route of deeper crack and vertical jointing between the red tuff blocks were presented in Figure 4.41. For the case of deeper crack on red tuff block, cavity depth was found 147mm with the with the correlation coefficients (R^2) in the range of 0.995-1.00. 147mm depth meant that it extended along the cross section of red tuff block, having the dimensions of 15cmx94cmx20cm (width x length x height). The crack having almost 15cm depth showed that the block was separated entirely into two. It was not expected to achieve transit time readings in such a case when transmitter and receiver were placed at both sides of the crack. However, a reliable UPV data was obtained when the transducers placed at the opposite sides of crack, presenting a constant slope of 4.42 and indirect UPV value of 335m/s±24m/s (Figure 4.41). It meant that broken tuff block was still well-fastened on the backing masonry with a proper adhesion.

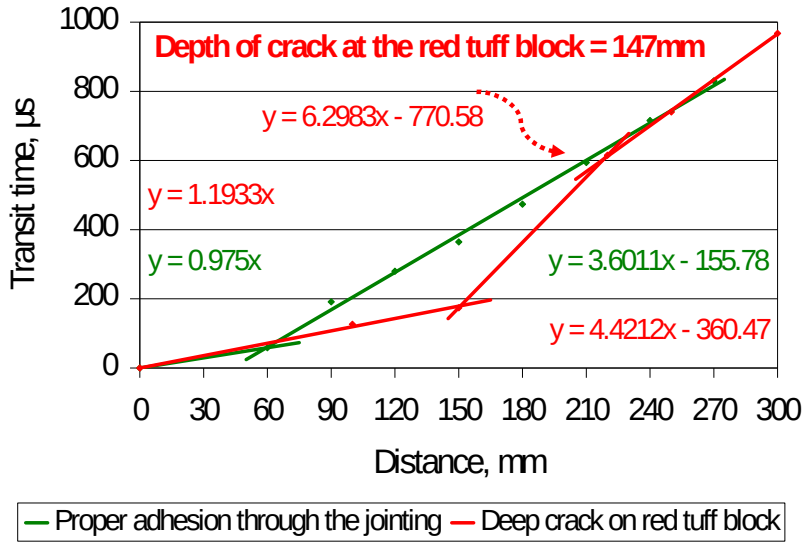

Figure 4.41 The slope of regression lines for the tuff followed by proper jointing (line in green) and the change in the regression slope corresponding to the depth of crack which had separated the red tuff block into two (line in red).

The results of indirect transit time readings taken on the route where there were two succeeding cracks being close to each other were summarized in Figure 4.42. Those cracks were “the fracture at jointing” followed by “the deep crack” on the red tuff

blocks surrounding the left bottom of window niche, as shown in Figure 4.40. The line in blue presented the UPV data taken on left-to-right direction when the fracture at jointing was the first crack on the route of measurement. The line in red presented the data taken at the opposite direction when the deep crack was the first crack on the route of measurement. When there were two successive cracks on the route of receiver, the displacement of regression line belonging to the first crack (fracture at jointing) seemed to dominate and conceal the signals for the following crack. The blue line in Figure 4.42 showed the sharp displacement of regression line for the fracture at jointing with the correlation coefficients (R^2) in the range of 0.75-1.00. (being the first crack on the route of transit time readings) while the red line in Figure 4.42 presented the displacement of regression line for the deep crack with the R^2 of 1.00 (being the first crack on the route of transit time readings).

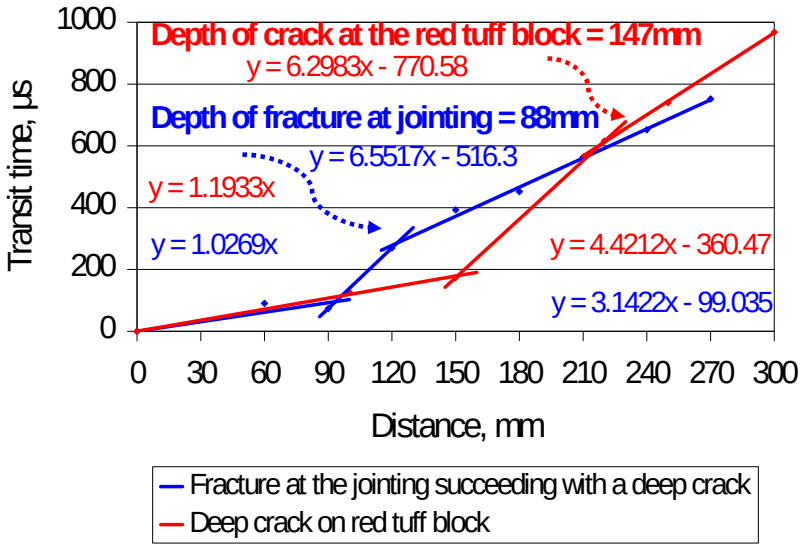

Figure 4.42 The changes in the slope of regression lines for the tuff corresponding to the depth of crack (line in red) and the depth of fracture at jointing (line in blue).

The results obtained from the transit time readings taken for the analyses of vertical and horizontal jointings between the red tuff blocks surrounding the right bottom of window niche were presented in the graph, as shown in Figure 4.43. Here, the red tuff presented a constant slope of regression line while the increase in the slope of

following regression line was due to the presence of jointing detail between neighbouring red tuff blocks (follow the line in green in Figure 4.43). The constant slope of 3.60 with the UPV value of 387m/s without any displacement in transit time readings demonstrated the sound/proper adhesion between the mortar and red tuff at the vertical jointing. On the other hand, the displacement in transit time measured immediately after the jointing with the correlation coefficients (R^2) in the range of 0.97-1.00 signalled the presence of a discontinuity/detachment which could not be observed visually (follow the line in orange in Figure 4.43). Here, the horizontal jointing at the right bottom of red tuff blocks was calculated to have a discontinuity at the depth of 86mm.

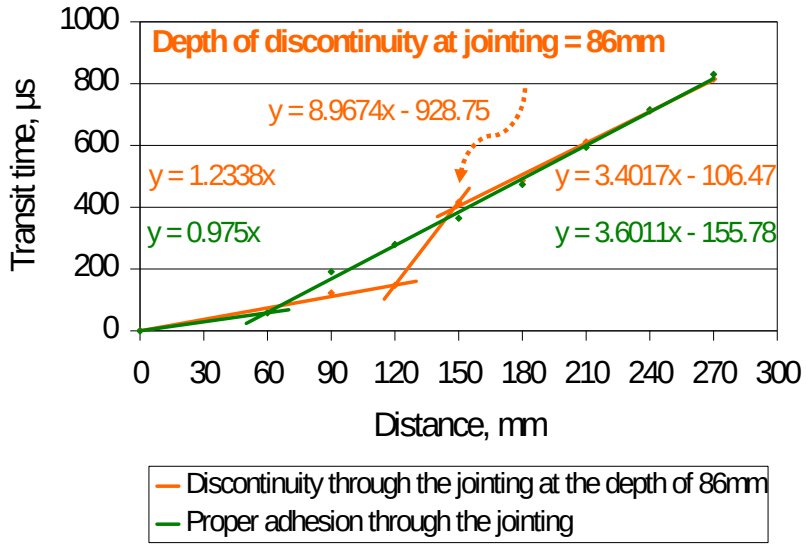

Figure 4.43 The slope of regression lines for the tuff followed by proper jointing (line in green) and the change in the regression slope corresponding to the depth of discontinuity at jointing (line in orange).

Although the transit time readings allowed to estimate the depth of deep cracks, no transit time readings were achieved on site for the deepest structural cracks at stone masonry where an air flow through the cavity was determined. No signal was the evidence of the deepest cracks separating the masonry entirely. On the other hand, the indirect transit time readings were failed to assess the superficial cracks associating/neighbouring with plaster detachments.

CHAPTER 5

DISCUSSION AND CONCLUSIONS

In this chapter, the results of *in-situ* studies were interpreted together in order to assess the structural cracks in terms of depth and activeness, the compatibility of recent repairs, the presence of historic sublayers hidden behind the recent repairs and to identify the different building stones in terms of thermal inertia characteristics. The impressions during the *in-situ* studies of QIRT and ultrasonic testing were evaluated for the improvement of those methods and the accuracy of *in-situ* data. At the end were given the conclusions followed by the suggestions for further studies.

5.1 Assessment of Structural Cracks

The results of ultrasonic testing and QIRT were evaluated together to define the depth of structural cracks and then to assess the thermal characteristics of those cracks in terms of activeness and depth for diagnostic purposes.

5.1.1 The depth assessment of structural cracks by ultrasonic testing

The UPV data obtained were analysed for the depth assessment of visible cracks on fair-faced red tuff blocks and for the soundness assessment of jointings in terms of proper adhesion between tuff and jointing mortar surfaces and presence of any failure/discontinuity through the jointing.

The indirect ultrasonic velocity (UPV_{IND-T}) and slope of the regression line (S_T) for the visually-sound red tuffs were determined to be $944ms^{-1}\pm83m\ s^{-1}$ and 1.08 ± 0.13,

respectively (Table 4.2). The jointing detail between the red tuff blocks decreased the indirect ultrasonic velocity (UPV_{IND-TM}) to 374ms^{-1}±23ms^{-1} and increased the slope of regression line (S_{TM}) to 3.38±0.23 (Table 4.2). Those values were accepted as the reference UPV data in indirect transmission mode for the sound red tuff individually and together with jointing mortar.

The measurements taken by the vernier calliper were failed to measure the real extent/depth of fractures and deep cracks at stone masonry while reliable transit time readings were achieved for the estimation of their real depths (Table 4.2). It was obvious that the depth probe cannot enter into tiny parts and/or curvilinear/devious parts of crack cavity while UPV measurements in indirect transmission mode were good at data acquisition for unattainable deeper cavities. The transit time readings could not be achieved on site for the deepest cracks at stone masonry permitting air flow through the cavity. That result proved that the deepest crack separated the block entirely into two.

When there were succeeding cracks/vertical discontinuities being close to each other on the same route of indirect UPV measurements, a special care should be given to the location of transmitter and the arrangement of the route for indirect UPV measurements, especially in the presence of successive defects. This meant that the direction of transit time readings became important for such cases. The sharp displacement of regression line, belonging to the first crack/discontinuity, seemed to hide the signs for the second/following crack(s), as shown in Figure 4.42. In order to improve the accuracy of the UPV analyses, the transit time readings should be taken by starting from both sides of cracks and repeating the measurements for several times.

The ultrasonic testing method in indirect transmission mode were found to be promising to examine the soundness of adhesion between mortar and stone surfaces at jointing details as well as the non-visible defects/discontinuities at deeper parts. For instance, a sound/proper adhesion between mortar and red tuff blocks was determined at the vertical jointing (Figure 4.40) with the constant slope of 3.60 with

the UPV value of 387m/s without any displacement in transit time readings (follow the line in green in Figure 4.43). On the other hand, the displacement in transit time measured immediately after the horizontal jointing signalled the presence of a discontinuity at the depth of 86mm which could not be observed visually (follow the line in orange in Figure 4.43). Those jointings, both vertical and horizontal ones, where no visual defect/failure noticed on their surfaces, were found to be sound as well up to a certain depth according to the QIRT analyses. Similar thermal inertia characteristics were determined for the visually-sound jointing mortar and red tuff blocks according to their similar thermal response during the heating period of 15 minutes by halogen lamp (Table 4.1). Considering all, the defect at horizontal jointing should be a local detachment at depth about 86mm, behind which proper adhesion was again achieved.

No transit time readings were achieved on site for the deepest structural cracks at stone masonry where an air flow through the cavity was determined. It was an expected situation for the case when transmitter and receiver were placed at both sides of a structural crack separating the masonry entirely into two.

5.1.2 Thermal characteristics for diagnostic purposes

The surface temperature data obtained by QIRT were analysed for the assessment of structural cracks in terms of activeness and depth.

The active cracks were observed to cause detachments of plaster layer at interiors followed by their loss in a short period of time. That impact of active cracks could easily be followed by QIRT. The route of the structural crack at the east wall, shown in Figure 4.1 and its extent along the dome surface was followed easily in the IR images as a warmer wide path while that could not be well-noticed visually (Figure 4.5). The warmer path indicated the plaster layer(s) detached from the backing

masonry where cracking occurred at. This was due to the tension stresses at the interface between the plaster and the masonry.

During the *in-situ* monitoring of structural cracks at the east walls, an increase in their width was determined by the vernier calliper with a difference, ΔW, of +0.61mm±0.31mm per 27days (see Table B.2). That movement signalled the instability of structure, which might be depending on the subsoil expansion due to the wet clayey ground. Those active cracks were observed to cause detachments of plaster layer at interiors followed by their loss in a short period of time (Figures 4.6 and 4.7). That impact of active cracks, such as growth of detached areas around the cracks, could easily be followed as enlargement of warmer patches with heterogeneous temperature distribution in IR images (Figure 4.6).

The visible crack following the arch above the window, shown in Figure 4.7, was determined to permit air flow through its cavity. It was observed to be the coldest path in the IR image. Here, there was another deepest crack, positioned parallel to that visible one (Figures 4.7 and 4.19). Its route was visually followed from outside while it was out of sight from inside since it was hidden behind the plaster layer(s). However, that non-visible crack at the backing masonry was detected in the same IR image as the next very cold path, acting like a thermal bridge (Figures 4.7 and 4.19-4.21). Its thermal behaviour was similar to the visible deepest crack permitting air flow through their cavities.

The quantitative analyses of thermal monitoring for visually sound masonry and joint mortar surfaces exhibited that red tuff and jointing mortar surfaces had similar rates of warming up and cooling down during the heating period of 856s and cooling period of 342s, respectively (Figures 4.8-4.10). That signalled that tuff and its jointing mortar had similar thermo-physical properties establishing similar thermal inertia characteristics. The wall surfaces coated with cement-lime based plaster and plastic paint had the coldest surfaces with the slowest rates of warming up and cooling down. The reason(s) of that different thermal inertia characteristic were

discussed in the following Section 5.2 in terms of compatibility of recent plaster repairs in relation to entrapped moisture problem.

The superficial cracks exhibited similar thermal response with the detached plaster surfaces associating with/neighbouring them, both presenting faster rates of warming up and cooling down than the sound surfaces (Figures 4.11-4.13). The superficial cracks, on the other hand, could be differentiated from detachments since those cracks had warming up and cooling down rates slightly slower than the neighbouring detachments during the heating and cooling periods, respectively.

On the other hand, the deep cracks at masonry wall with the depths of 88mm and 147mm, presented noticeably slower warming up and cooling down rates than the sound surfaces (Figures 4.14-4.16). The deeper crack seemed to have presented lower warming up rate than the less deep one, in other words, slower thermal response to the heating up conditions. In contrast to deep and superficial cracks, the deepest crack allowing air leakage through the wall section (Figure B.1) had the coldest surface temperature and cooled down during the heating period (Figures 4.14, 4.15, 4.17, 4.19 and 4.20). That was due to the entrapped moisture in the masonry and air flow through the gap/cavity of crack, both accelerating the evaporative cooling.

In brief, it was not possible to differentiate which crack was deeper than the other one visually. However, the preliminary results showed that *in-situ* QIRT survey could make it possible to distinguish them from each other relatively according to their depth. The data on the warming up (R_W) and cooling down rates (R_C) for each crack/defect were summarized in Table 4.1, Figures 4.24 and 4.25. Each crack with different depths presented warming up (R_W) and cooling down rates (R_C) in varying amounts. Those rates for each crack/defect when compared with the warming up/cooling down rates of visually-sound surfaces showed that there was a relationship between the thermal response of each crack/defect and its depth. For the analysis of deep cracks, the thermal monitoring during the exposure of heating conditions seemed to be more effective than the thermal monitoring during the

cooling conditions; in other words, more noticeable differences between the thermal responses of deep cracks was determined during the heating period, especially for the deepest crack permitting air flow through its cavity. However, more noisy data achieved during the heating period should be considered during the analyses.

The cooling down rates of the non-visible deepest crack hidden behind the plaster layer and the visible deepest crack were exactly the same during the cooling period (Figure 4.25). On the other hand, the presence of plaster layer still covering/hiding the deepest crack at the interior side of the wall seemed to prevent the evaporating cooling from the exposed surface during the heating period (Figure 4.19 and 4.20). Even in that case, the thermal response of the non-visible deepest crack behind the plaster layer seemed to dominate and its surface temperatures presented the next coldest pattern in the IR images, while the coldest surfaces belonging to the visible deepest cracks. That made the paths of deepest cracks clearly observed in the infrared images as the coldest surfaces, even for the non-visible ones hidden by a plaster layer.

Slight fluctuations of ambient temperature and air flow during the interior investigations were inevitable due to the entrance door left open. Although that inconvenient situation, the correlation coefficients (R^2) of linear regression between the surface temperature/temperature difference and square root of time during thermal monitoring were satisfactory, being in the range of 0.88 and 0.98. However, the surface temperature data of deep cracks, especially the deepest ones collected during the heating period were noticeably noisy while being more consistent during the cooling period. The heating process should have accelerated the evaporative cooling at cracks in varying ranges depending on their depth/amount of exposed surface area, the moisture content in the masonry wall, and air flow through the cavity.

5.2 Compatibility Assessment of Recent Plaster Repairs

The tuff stone masonry was determined to have good thermal insulation characteristics due to its low thermal transmittance value. The *U* value of tuff masonry wall examined in Cenabi Ahmet Paşa Camisi was calculated over assumptions which were given in Appendix C in detail. In the calculations, the thermal conductivity of welded tuffs was taken in the range of 0.40 W $m^{-1}K^{-1}$ and 0.73 W $m^{-1}K^{-1}$ (Erdoğan, 1986; Özkahraman, *et al*., 2006), and the thermal conductivity of masonry mortar was assumed 0.71 W $m^{-1}K^{-1}$ (Tavukçuoğlu, *et al*., 2008), the thermal transmittance through the 1.80m-thick tuff wall section, U_{TW}, was calculated to be in the range of 0.25W $m^{-2}K^{-1}$ and 0.38W $m^{-2}K^{-1}$. Those U_{TW} values were lower than the *U* value of 0.50 W $m^{-2}K^{-1}$ required for the walls of energy efficient houses at the same climatic region (TS 825, 2008). Those U_{TW} values confirmed the good thermal insulation characteristics of the tuff masonry structure. However, most interior wall surfaces were colder than the ambient temperature in varying ranges while the wall surfaces coated with cement-lime based plaster and plastic paint were the coldest areas having the slowest rates of warming up and cooling down. That signalled the decrease in the overall thermal resistance of masonry wall section, causing extensive heat loss from those colder wall surfaces (Figures 4.8-4.13, 4.26, 4.30, 4.31).

The entrapped moisture in the wall section due to the wrong repair with water vapour impermeable plastic paint should be the reason of that thermal failure. The rainwater penetration through the structural cracks should also have contributed to the increase in moisture content, which should be examined in detail by further QIRT analyses.

5.3 Identification of Historic Wall Painting Layer and Assessment of Historic Plaster Layer(s) Hidden Behind the Wall Paintings Recently Done

The IR scanning of the overall interior surfaces by utilizing the through-wall natural thermal gradient made it possible to differentiate the different sublayer compositions behind the recently repaired surfaces. The probability of still keeping the porous historical plaster layer(s) underneath the recently repaired surfaces, which was reported by Kökdemir and Dirican (2008) only for a spot area, seemed to be approved by the QIRT analyses. The presence of porous sublayer(s) was expected to lead the warmer surface temperature distribution at interior surfaces due to the increase in thermal resistivity of masonry wall at the warm side. The decoratively-painted wall surfaces above the first-layer windows were determined to have warmer surface temperatures with an even distribution than the painted wall surfaces remained (Figures 4.30 and 4.31). The analysis of surface temperature data together with the inside air temperature close to the surface under examination, presented the differences in wall configuration quantitatively (Figure 4.31). In brief, IRT scanning of the whole structure allowed us to locate the different wall configurations, such as the surfaces which might still keep their original plaster/paint sublayers hidden behind the renewed plaster and paint layers.

The remains of old wall painting were also examined in order to see whether those surfaces could be distinguished from the recent ones by QIRT or not. The sequential IR imaging of the old and recent wall painting surfaces during the heating up (by using fan heater) and cooling down periods was found to be promising. A preliminary knowledge on their thermal response characteristics was achieved that the old wall painting surface was determined to warm up and cool down slightly faster than the recent wall painting surface (Figure 4.32). However, further analyses, such as thin section and scanning electron microscopy analyses, are needed to well-define the paint layer, its complementary sublayer(s) and to reveal the reason(s) of their different thermal characteristics.

5.4 Detection of Stone Types and Stone Decays

The method of IR thermography was highly-capable of detecting the damp zones and detached surfaces at stone masonry walls:-

- The damp/wet zones of the structure washed by the rainwater discharged from the gutters were determined to be the coldest surfaces in IR images, due to the evaporative cooling accelerated at the exposed conditions (Figure 4.39). The damp zones together with biological growth, on the contrary was detected as the warm patches in the IR images due to the temperature of living organisms (Figure 4.39), while still being slightly below the ambient temperature. This meant that the temperature of living organisms seemed to be dominant on damp surfaces which made biological growths visible in IR images on damp surfaces.

- The repaired tuff surfaces plastered with the cement-based coats were determined to have detached which could not be observed by eye (Figure 4.34). The detached surfaces detected as warm patches in the individual IR images and presented faster warming up rate than the visually-sound tuff masonry during the slight heating period of daytime (Figures 4.34, 4.35 and 4.38). That was due to the lower thermal inertia characteristics of detached parts.

In brief, the IR scanning allowed to locate the failure of detachment and to map its distribution on masonry wall surfaces.

The analyses of individual and sequential IR imaging have shown up the thermal inertia characteristics of red and yellowish tuffs on quantitative basis. When exposed to solar radiation, red tuff arch stone warmed up faster than the yellowish one (Figure 4.35). That signalled lower thermal inertia characteristics of red tuff when compared to the yellowish one. Corresponding to those thermal inertia characteristics, the red tuff presented warmer surface temperatures than the yellowish tuff in the individual IR images during the warming up periods of daytime (Figure 4.38).

5.5 Evaluation of Non-Destructive Investigation Methods Used *In-Situ*

The study clearly exhibited that the *in-situ* UPV measurements provided a precise knowledge on depth of cracks at stone masonry and proved its potential for detecting non-visible failure(s) at deeper layers. Due to its achievements, *in-situ* ultrasonic testing was complementary to *in-situ* QIRT survey for the assessment of structural cracks in stone masonry while its use was more reasonable for representative sampling instead of its extensive use in the structure. It was experienced that the use of that method *in-situ* was really demanding. The study required long working hours at site and repetition of UPV measurements for several times to achieve reliable data. It was not easy to control the environmental background noise destroying the UPV data considerably, such as vibration(s) due to the heavy traffic, heavy vehicles and their horns, especially when studied at outside. Data acquisition was also restricted to the levels available for human body.

The QIRT survey, on the other hand, was easier and more practical method to achieve reliable and precise data in a short period of time in case the method of data acquisition at site has been carefully-thought and well-organized beforehand. Here, the selection of sensitive thermographic equipment with high image quality enhanced the accuracy of data collection and allowed its extensive use in the structure, especially for imaging the unattainable regions and tiny/small regions having small amount of surface area such as cracks. The changes in microclimatic conditions, such as air flow, temperature and humidity fluctuations as well as precipitation, mostly could not be controlled on site, increased the noisy data extremely.

The joint interpretation of QIRT and ultrasonic testing results enhance the accuracy of soundness assessment for the jointing details. For instance, no visual defect/failure noticed on the surfaces of vertical and horizontal jointings between the red tuff blocks (Figure 4.40). Those jointings were found to be sound up to a certain depth due to the similar thermal inertia characteristics determined for both red tuff and jointing mortar surfaces (follow the charts given in Figures 4.9, 4.10, and Table 4.1).

The soundness of vertical jointing was approved by the ultrasonic analyses. However, the UPV results have shown up a non-visible local discontinuity/detachment at the horizontal jointing at the depth of 86mm, behind which proper adhesion was again achieved.

The *in-situ* NDT studies, in fact, should be supported by some laboratory analyses in order to obtain reference data for the comparisons and correct interpretation of the *in-situ* data. However, due to the difficulty in collecting samples from the stone masonry historic structures and in producing representative samples for the historic structure/fabric, there was a necessity to achieve reference data *in-situ*. A special care was therefore, given to find out the reference UPV and surface temperature data by including the reference area, such as sound and dry stone surface, into the field of study at the same boundary conditions.

The environmental conditions before and during the sequential IR imaging had significant importance for achieving accurate data on the real surface temperatures of wall surfaces which present their real thermal inertia characteristics. For instance, the sequential IR imaging six hours later than the preliminary wetting by the light summer rain was a complicated and misleading situation to compare the thermal inertia characteristics of tuffs. If the masonry wall is dry, the surface temperatures of the exposed wall surfaces are expected to be warmer than the outside air temperature. Here, the visually-sound tuff surfaces were determined to be slightly-below the ambient temperature. This showed that the masonry wall was still damp in varying ranges. The moisture content in tuffs should have affected their thermal inertia characteristics due to its presence in varying ranges. Further studies, therefore, are required for the correct analyses of these in-situ data obtained in such conditions for establishing the reference/control data and for the comparison of data achieved on site and laboratory.

5.6 Conclusion

The IR scanning, without doubt, was necessary and a practical way for the check-up the overall structure. However, during the *in-situ* examination of an historic masonry structure, sequential IR imaging from representative areas was obligatory for the correct interpretation of single IR images and enhanced the effectiveness of *in-situ* survey.

The active cracks were observed to cause detachments of plaster layer at interiors followed by their loss in a short period of time. That impact of active cracks could easily be followed by QIRT. The study has also shown up the thermal behaviour characteristics of cracks, such as:-

- The superficial cracks associating with/neighbouring plaster detachments had thermal response similar to detached surfaces, having faster warming up and cooling down rates than the sound surfaces.
- The deeper cracks at masonry wall, on the other hand, presented noticeably slower warming up and cooling down rates than the sound surfaces.
- The deepest cracks allowing air leakage through the wall section had the coldest initial surface temperature and slightly cooled down during the heating period due to the accelerated evaporative cooling in the crack cavity.

That knowledge made it possible to distinguish the cracks easily from each other according to their depth by using QIRT while it was not possible to differentiate them visually. Those results were encouraging for diagnostic and monitoring purposes that gave the hints/signs to develop *in-situ* methods for quantitative assessment of crack depth, only by using temperature measurements. The thermal monitoring of cracks, particularly during the exposure of heating conditions, was promising for the depth assessment of deep cracks in masonry.

The ultrasonic testing in indirect transmission mode provided data on estimating the depth of a visible crack at masonry wall, detecting non-visible failure/discontinuity at

deeper layers and assessing the proper adhesion between mortar and stone surfaces at jointing detail. Those achievements made it a necessary tool for the *in-situ* QIRT survey, particularly to achieve a quantitative data on depth of cracks. The collaborative use of QIRT and ultrasonic testing allowed to define the thermal inertia characteristics of cracks in relation to their depth and enhanced the accuracy of the non-destructive *in-situ* survey.

The results obtained from IR scanning of wall surfaces and sequential IR imaging taken from representative regions of wall surfaces showed that:-

- The tuff masonry wall with 1.80m width was expected to have good thermal performance in regard to the low thermal transmittance values calculated by using heat transfer calculations and by taking into consideration the wall configurations and thermal conductivity values of tuff stone (Appendix C). The walls having sufficient thermal insulation characteristics were expected to have warmer surfaces at interior side of exterior wall. However, the interior surface of historic masonry wall was determined to be the coldest surfaces, being considerably below the ambient temperature and having the slowest rates of warming up and cooling down. This signalled the decrease in the overall thermal resistance of masonry wall section, causing extensive heat loss from those colder wall surfaces. In brief, inherently good thermal resistivity of that historic wall structure has failed due to the entrapped moisture resulting from incompatible recent repairs with water vapour impermeable plaster and plastic paint.
- The IRT scanning of the overall interior surfaces made it possible to locate the different wall configurations, such as the historical plaster sublayer(s) backing the recent wall painting surfaces, when a certain thermal gradient was achieved through the wall section. The presence of porous sublayer(s) led to the warmer and evenly distributed surface temperature pattern at interior surfaces due to the increase in thermal resistivity of masonry structure at the warm side of wall section.
- Thermal monitoring of stone surfaces during heating and cooling exposure conditions allowed to differentiate the different types of stones used at stone

masonry wall. That was due to the different thermo-physical properties of stones leading to different thermal inertia characteristics.

– The method of IR thermography was highly-capable of detecting the damp zones and detached surfaces at stone masonry walls. This allowed to locate the failures of moisture and detachment clearly and to map the distribution of these failures on masonry wall surfaces.

After the preliminary slight rainfall, the surface temperature measurements may be misleading for some hours to determine the real thermal inertia characteristics of wall surfaces. The analyses of in-situ data obtained in such conditions require further studies including the laboratory analyses to produce the reference/control data. The comparison of in-situ data and control data will be useful to better understand the thermal inertia characaterics of tuffs having moisture content in varying ranges.

Some further studies are suggested here which seemed to be necessary to improve the quantitative analyses of stone masonry historic structures *in-situ* by using QIRT. For instance, the thermal inertia characteristics of masonry wall sections in the presence of entrapped moisture problem should be examined in detail by means of *in-situ* and laboratory QIRT analyses in order to discover the thermal responses of their surfaces covered with water vapour permeable and impermeable plaster layers

The different thermal responses defined for the deep cracks might be due to the thermal behaviour of microclimates created in their own cavities, which should be examined in detail by further analyses with an emphasis on depth, moisture content in the masonry and boundary conditions. Thermal responses of different stone types in dry and damp conditions should be examined in detail by further QIRT analyses in laboratory in order to interpret the *in-situ* infrared data correctly.

In the study, reliable transit time data for the depth estimation was achieved while a systematic decrease seemed to be observed at the indirect ultrasonic velocities. The indirect UPV values are expected to be lower than direct UPV values, depending on the material (Turgut, *et al*., 2006; Lemoni, *et al*., 1999). In this study, decrease in

indirect UPV values was more than the expected rate depending on no use of coupling agent. Further laboratory researches, therefore, are needed to achieve reference/control data on indirect and direct ultrasonic velocities for tuffs with and without using any coupling agent for comparisons and for confirmation.

REFERENCES

ANDOLSUN, S. 2006. A Study on Material Properties of Autoclaved Aerated Concrete (AAC) and its Complementary Wall Elements: Their Compatibility in Contemporary and Historical Wall Sections, *Unpublished MSc Thesis*, Department of Architecture, Building Science Graduate Program, METU, Ankara, Supervisor: Ayse Tavukcuoğlu.

Archives of General Directorate of Pious Foundation. 2008. *1/50-measured drawings of Cenabi Ahmet Paşa Camisi*, in: Folder of Cenabi Ahmet Paşa Camisi.

ATKINSON, R.H., J.L. Noland and G.R. Kingsley. 1998. Application of NDE to Masonry Structures – Current Technology and Future Needs, in: *Conservation of Historic Brick Structures* (p. 85-93). N. S. Baer, S. Fitz and R. A. Livingston, eds. Donhead. UK.

AVDELIDIS, N.P., E.T. Delegouc, D.P. Almondb and A. Moropoulou. 2004. Surface roughness evaluation of marble by 3D laser profilometry and pulsed thermography, in: *NDT&E International* (p. 571-575, v. 37).

AVDELIDIS, N.P., A. Moropoulou and P. Theoulakis. 2003a. Detection of water deposits and movement in porous materials by infrared imaging, in: *Infrared Physics & Technology* (p. 183-190, v. 44).

AVDELIDIS, N.P. and A. Moropoulou. 2003b. Emissivity Considerations in building thermography, in: *Energy and Buildings* (p. 663-667, v. 35).

BAGGIO, P., C. Bonacina, E. Grinzato, P. Bison and C. Bressan. 1993. Non-destructive tests for measurement of moisture content in porous building materials. Theoretical and experimental approach. *Conservation of Stone and Other Materials*. Ed. M.-J. Thiel. E&FN Spon, London (p. 351-358, v. 1).

BALARAS, C.A. and A.A. Argiriou. 2002. Infrared thermography for building diagnostics, in: *Energy and Buildings* (p. 171-183, v. 34).

BAŞKAN, S. 1993. *Ankara Cenabi Ahmet Paşa Camii*. Kültür Bakanlığı Yayınları. Ankara.

BISON, P.G., S. Marinetti, A. Mazzoldi, and C. Bressan. 2002. Cross-comparison of thermal diffusivity measurements by thermal methods, in: *Infrared Physics & Technology* (p. 127-132, v. 43).

BOZTEPE, M. 1987. A Microclimatic Investigation In Relation to the State of Preservation of Wall Paintings in Cenabi Ahmet Paşa Mosque, *Unpublished MS Thesis*, Middle East Technical University, Department of Architecture, Graduate Program in Restoration, Ankara, Supervisor: Emine N. Caner Saltık.

BRAY, D. E. and D. McBride. 1992. *Nondestructive Testing Techniques*. Wiley. New York.

CANER SALTIK, E. N., A. Tavukçuoğlu, G. Akoğlu and A. Güney. 2005. The Material Analyses of Yalınayak Bath, *Unpublished Analyses Report in the context of REST 555 Course*, METU, Ankara.

CANER SALTIK, E. N., S. Demirci, A. Güney, G. K. Akoğlu and E. Caner. 2003. Material Research Fund Project BAP-2003.02.01.02: Technological properties of some plasters used as roof covering material in historic structures, *Unpublished Final Research Report*, METU Faculty of Architecture, Ankara, 25 pages.

CHENG, C., T. Cheng and C. Chiang. 2008. Defect detection of concrete structures using both infrared thermography and elastic waves, in: *Automation in Construction* (p. 87-92, v. 18).

CHRISTARAS, B. 1999. Effectiveness of in situ P-wave measurements in monuments, in: *Proceedings of the 9th Eurocare Euromarble EU496 Workshop* (p. 133-137). 8-10 October, 1998. Munich.

CHRISTARAS, B., F. Auger and E. Mosse. 1994. Determination of the moduli of elasticity of rocks. Comparison of the ultrasonic velocity and mechanical resonance frequency methods with direct static methods, in: *Materials and Structures* (p. 222-228, v. 27).

ÇETİN, Ö. and E. Canbay. 2008. Cenabi Ahmet Paşa Camii temel zeminleri geoteknik değerlendirme raporu. *Unpublished report*, Department of Civil Engineering, Middle East Technical University, Ankara.

ÇİÇEK (KIRMIZIDAĞ), P. 2009. Thermal Performance Assessment of Historical Turkish Baths, *Unpublished MSc Thesis*, Middle East Technical University, Department of Architecture, Building Science Graduate Program, Ankara, Supervisor: Ayşe Tavukçuoğlu.

DEFER, D., J. Shen, S. Lassue and B. Duthoit. 2002. Non-destructive testing of a building wall by studying natural thermal signals, in: *Energy and Buildings* (p. 63-69, v. 34).

DİŞLİ, G. 2008. An Investigation on the Water Supply and Drainage Systems of Historical Turkish Baths, *Unpublished MSc Thesis*, Middle East Technical University, Department of Architecture, Building Science Graduate Program, Ankara, Supervisor: Ayşe Tavukçuoğlu.

ELDRIDGE, H.J. 1976. *Common defects in buildings*. Building Research Establishment.

ERDOĞAN, M. 1986. Nevşehir-Ürgüp Yöresi Tüflerinin Malzeme Jeolojisi Açısından Araştırılması. *Unpublished Phd Thesis*. Istanbul Technical University. Maden Fakültesi.

ESEN, S. Y. 2008. Ankara ili, Altındağ ilçesi Ulucanlar Yeni Cami (Cenabi Ahmet Paşa Camii) restitüsyon projesinin hazırlanması işi. *Unpublished research report*, submitted to General Pious Foundation.

ESEN, S., N. Tunç, S. Telatar, A. Tavukçuoğlu, E. N. Caner Saltık and S. Demirci. 2004. Manisa Çukur Hamam'ın Onarımına Yönelik Malzeme Çalışmaları, in: *Proceedings of 2nd National Congress and Exhibition on Building Materials*, İstanbul, Turkey, 6-8 October 2004, TMMOB Chamber of Architects – İstanbul Branch, p. 494-505.

FITZNER, B. 2004. Documentation and evaluation of stone damage on monuments. *10th International Congress on Deterioration and Conservation of* Stone. Stockholm. Accessed by www.stone.rwth_aachen.de/stockholm2004.pdf.

FITZNER, B., K. Heinrichs and R. Kownatzki. 1995. Weathering Forms – Classification and Mapping. *Denkmalpflege und Naturwissenschaft Natursteinkonservierung I*. Ernst& Sohn, Berlin (p. 41-88).

FITZNER, B., K. Heinrichs and R. Kownatzki. 1992. Classification and mapping of weathering forms. *7th International Congress on Deterioration and Conservation of Stone, Proceedings*. Ed. J. D. Rodrigues, F. Henriques, F. T. Jeremies. LNEC, Lisbon (p. 957-967).

GALAN, E., M. I. Carretero and E. Mayoral. 1999. A methodology for locating the original quarries used for constructing historical buildings: application to Malaga Cathedral, Spain, in: *Engineering Geology* (p. 287–298, v. 54).

GALAN, E. 1991. The influence of temperature changes on stone decay, in : *Proceedings of the C.U.M. 1st Course "Weathering and Air Pollution"*. Ed. M. Adda. C.U.M. University School of Monument Conservation, Bari, Italy (p. 119-129).

GIOVANNI M. C. and C. Meola. 2002. Comparison between thermographic techniques for frescoes NDT, in: *NDT&E International* (p. 559-565, v. 35).

GOULART S.V.G. 2004. Thermal Inertia and Natural Ventilation – Optimisation of Thermal Storage as a Cooling Technique for Residential Buildings in Southern Brazil. *Unpublished Phd. Thesis*, Architectural Association School of Architecture, Graduate School.

GRINZATO, E., P. Bison and A. Tavukcuoglu. 2009. Caratterizzazione di materiali edili, con il metodo integrato termografico-ultrasonico-analitico, in: *La Conferenza AIPnD (Associazione Italiana Prove non Distruttive Monitoraggio Diagnostica) - PnD Roma 2009 Innovazione e Professionalita', sessioni: Ingegneria Civile*. 15-17 October 2009. Rome: AIPnD, Italy.
(http://www.ndt.net/article/aipnd2009/files/orig/13.pdf)

GRINZATO, E., G. Cadelano, P. G. Bison and A. Petracca. 2009. Seismic risk evaluation aided by IR thermography, in: *Proceedings SPIE, Thermosense XXXI*. Orlando, USA.

GRINZATO, E., S. Marinetti, P. G. Bison and M. Concas. 2004. Comparison of ultrasonic velocity and IR thermography for the characterisation of stones, in: *Journal of Infrared Physic and Technology* (p. 63-68, v. 46).

GRINZATO, E., P. G. Bison and S. Marinetti. 2002a. Monitoring of ancient buildings by the thermal method, in: *Journal of Cultural Heritage* (p. 21-29, v. 3).

GRINZATO, E., C. Bressan, S. Marinetti, P. G. Bison and C. Bonacina. 2002b. Monitoring of the Scrovegni Chapel by IR thermography: Giotto at infrared, in: *Infrared Physics & Technology* (p. 165-169, v. 43).

GRINZATO, E., V. Vavilov and T. Kauppinen. 1998. Quantitative infrared thermography in buildings, in: *Energy and Buildings* (p. 1-9, v. 29).

GRINZATO, E., P. G. Bison, S. Marinetti and V. Vavilov. 1994. Thermal/Infrared non-destructive evaluation of moisture content in building: theory and experiment, in: International symposium *Dealing with defects in building*, Proceedings, p. 345-357, Varenna, Italy.

HALL, F. 1994. *Building Services & Equipment*, v.1, chapter 4 Heat Losses. 3rd edition, Longman Group UK Limited.

HALL, F. 1994. *Building Services & Equipment*, v.1, chapter 7 Heating. 3rd edition, Longman Group UK Limited.

HENS, H. 2007. *Building Physics-Heat, Air and Moisture*. Ernst&Sohn A Wiley Company. Berlin, Germany.

INCROPERA, F. P. and D. P. Dewitt. 1990. *Fundamentals of Heat and Mass Transfer*. Wiley, NewYork.

KAHRAMAN, S., M. Soylemez and M. Fener. 2008. Determination of fracture depth of rock blocks from P-wave velocity. *Bull Eng Geol Environ*. (p. 11-16, v. 67).

KANDEMIR YUCEL, A., A. Tavukçuoğlu and E.N. Saltık. 2007. In situ assessment of structural timber elements of a historic building by infrared thermography and ultrasonic velocity, in: *Infrared Physics* & Technology (p. 243-248, v. 49).

KÖKDEMIR, E. and T. Dirican. 2008. Cenab-i Ahmet Paşa Camii, Boya ve Sıva Katmanı Araştırmaları. *Unpublished research report*, submitted to General Pious Foundation.

LEMONI, H. and B. Christaras. 1999. Classification of soils using in situ ultrasonic velocity techniques, in: *The 12th European Conference on Soil Mechanics and Geotechnical Engineering* (p. 393-400). June 7-10, 1999. Amsterdam, Netherlands.

MAGNANI, F.S. and R.N.T. Silva. 2007. Infrared thermography applied to the quantitative determination of spatial and thermophysical parameters of hidden included objects, in: *Applied Thermal Engineering* (p. 2378–2384, v. 27).

MALDAGUE, X.P.V. 2001. *Theory and practice of infrared technology for non-destructive testing*. John Wiley & Sons, Inc. New York.

MAIERHOFER, Ch., A. Brink, M. Röllig and H. Wiggenhauser. 2002. Transient thermography for structural investigation of concrete and composites in the near surface region, in: *Infrared Physics & Technology* (p. 271–278, v. 43).

MATSUKURA, Y. and T. Hirose. 1999. Five year measurements of rock tablet weathering on a forested hillslope in a humid temperate region, in: *Engineering Geology* (p. 69-76, v. 55).

MEOLA, C. 2007a. A new approach for estimation of defects detection with infrared thermography, in: *Materials Letters* (p. 447-450, v. 61).

MEOLA, C. 2007b. Infrared thermography of masonry structures, in: *Infrared Physics & Technology* (p. 228-233, v. 49).

MEOLA, C., R.D. Maio, N. Roberti and G.M. Carlomagno. 2005. Application of infrared thermography and geophysical methods for defect detection in architectural structures, in: *Engineering Failure Analysis* (p. 875-892, v. 12).

MEOLA, C., G.M. Carlomagno and L. Giorleo. 2004. The use of infrared thermography for materials characterization, in: *Journal of Materials Processing Technology* (p. 1132-1137, v. 155-156).

MOROPOULOU, A., K. Polikreti, V. Ruf and G. Deodatis. 2003. San Francisco Monastery, Quito, Equador: Characterisation of building materials, damage assessment and conservation considerations, in: *Journal of Cultural Heritage* (p. 101-108, v. 4).

MOROPOULOU, A., N.P. Avdelidis, E.T. Delegou and M. Koui. 2001. Infrared thermography in the evaluation of cleaning interventions on architectural surfaces, in: *Proceedings of InfraMation 2001*.

OCANA, S.M., I.C. Guerrero and I.G. Requena. 2004. Thermographic survey of two rural buildings in Spain, in: *Energy and Buildings* (p. 515-523, v. 36).

ÖZKAHRAMAN, H. T. and A. Bolattürk. 2006. The use of tuff stone cladding in buildings for energy conservation, in: *Construction and Building Materials* (p. 435–440, v. 20).

ÖZKAHRAMAN, H. T., R. Selver and E.C. Işık. 2004. Determination of the thermal conductivity of rock from P-wave velocity, in: *International Journal of Rock Mechanics and Mining Sciences* (p. 703-708, v. 41).

PAIK, J., C.P. Lee and M.A. Abidi. 2002. Image processing-based mine detection techniques: a review, in: *Subsurface Sensing Technologies and Applications* (p. 153-202, v. 3, No. 3).

ROPELEWSKI L. and R. D. Neufeld. 1999. Thermal inertia properties of autoclaved aerated concrete, in: *Journal of Energy Engineering* (p. 59-75, v. 125).

SAKAGAMI, T. and S. Kubo. 2002. Applications of pulse heating thermography and lock-in thermography to quantitative nondestructive evaluations, in: *Infrared Physics & Technology* (p. 211-218, v. 43).

SINGH, T.N., S. Sinha and V.K. Singh. 2007. Prediction of thermal conductivity of rock through physic-mechanical properties, in: *Building and Environment* (p. 146-155, v. 42).

SNETHLAGE, R. and H. Ettl. 1996. Ultrasonic measurements on in-situ consolidated marble reliefs at the victory gate in Munich, in: *Proceedings of the 7th Eurocare Euromarble EU496 Workshop* (p. 66-73). 21-23 October, 1996. Patras.

SOUSA, L.M.O., L.M.S. Rio, L. Calleja, V.G.R. Argandona and A.R. Rey. 2005. Influence of microfractures and porosity on the physico-mechanical properties and weathering of ornamental granites, in: *Engineering Geology* (p. 153-168, v. 77).

SOWDEN, A.M. 1990. *The maintenance of brick and stone masonry structures*. E.&F.N. Spon: London. Chapter 5 - Inspection and recording (Ed. A.M. Sowden).

STROTHER, E.F. and W.C. Turner. 1990. *Thermal Insulation Building Guide*. Robert E. Krieger Publishing Company. Malabar, Florida.

TAVUKÇUOĞLU, A., P. Cicek and E. Grinzato. 2008. Thermal analysis of an historical Turkish bath by quantitaive IR thermography, in: *Quantitative Infrared Thermography Journal* (p. 151-173, v. 5(2)).

TAVUKÇUOĞLU, A., A. Düzgüneş¸ E.N. Caner-Saltık and S. Demirci. 2005. Use of IR thermography for the assessment of surface-water drainage problems in a historical building, Ağzıkarahan (Aksaray), Turkey, in: *NDT&E International* (p. 402–410, v. 38).

TAVUKÇUOĞLU, A. 2001. A study on the maintenance of stone monuments in relation to dampness problems, *Unpublished Ph.D. Thesis*, Middle East Technical University, Department of Architecture, Building Science Graduate Program, Ankara, Supervisor: Emine N. Caner Saltık.

TAVUKÇUOĞLU, A. and E.N. Caner Saltık. 1999. Mapping of visual decay forms and infrared imaging of stone structures for the maintenance and monitoring studies. *Durability of Building Materials and Components 8*. Ed. M. A. Lacasse. D. J. Vanier. NRC Research Press, Canada (p. 613-623, v. 1).

TITMAN, D.J. 2001. Applications of thermography in non-destructive testing of structures, in: *NDT&E International* (p. 149–154, v. 34).

TS 825. 2008. *Rules of Thermal Insulation in Buildings*, May 2008. Turkish Standards Institution, Ankara.

TS EN 1745. 2004. *Masonry and masonry products - Methods for determining design thermal values*, April 2004. Turkish Standards Institution, Ankara.

TS EN ISO 6946. 2007. *Building components and building elements – Thermal resistance and thermal transmittance – Calculation method*, April 2007. Turkish Standards Institution, Ankara.

TURGUT, P. and O. F. Kucuk. 2006. Comparative relationships of direct, indirect, and semi-direct ultrasonic pulse velocity measurements in concrete, in: *Russian Journal of Nondestructive Testing* (p. 745-751, v. 42).

UĞUR, I., S. Demirdağ and H. Yavuz. 2010. Effect of rock properties on the Los Angles abrasion and impact test characteristics of the aggregates, in: *Material Characterization* (p. 90-96, v. 61).

WIGGENHAUSER, H. 2002. Active IR-applications in civil engineering, in: *Infrared Physics & Technology* (p. 233–238, v. 43).

Webster's online dictionary home page, http://www.websters-online-dictionary.org/definition, accessed: February 2010.

Wikipedia home page, http://en.wikipedia.org/wiki, accessed: February 2010.

APPENDIX A

TECHNICAL SPECIFICATIONS OF INSTRUMENTS USED IN THE STUDY

A.1 FLIR ThermaCAM SC640 Infrared Camera

Figure A.1 Views of FLIR ThermaCAM SC640 Infrared Camera from different angles (www.flir.com.hk and www.grimas.hu) (at the left) and experimental set-up for IR imaging controlled by laptop (at the right)

Imaging Performance

Thermal:	
Field of view/min focus distance	24ºx18º /0.3 m
Spatial resolution (IFOV)	0.65 mrad
Thermal sensitivity	60mK at 30°C
Image frequency	30 Hz non-interlaced
Focus	Automatic or manual
Electronic zoom / pan function	1 - 8 x continuous, including pan function

Detector type	Focal Plane Array (FPA), uncooled microbolometer 640 x 480 pixels
Spectral range	7.5 to 13µm
Digital image enhancement	Normal and enhanced
Visual:	
Built-in digital video	1.3 Mpixel, full color / built-in Target Illuminator / exchangeble lens
Standard lens performance	f=8 mm / FOV 32°

Image Presentation

Video output	RS170 EIA/NTSC or CCIR/PAL composite video, IEEE-1394 FireWire, USB
Viewfinder	Built-in, tiltable, high-resolution color viewfinder (800 x 480 pixels)
External display	Built-in 5.6” LCD (1024 x 600 pixels)

Measurement

Temperature range	-40°C to +1,500°C, in 3 ranges; up to + 2000°C, optional
Accuracy	±2°C, ±2% of reading
Measurement mode	Spots/Areas (Boxes, Circles), Isotherms (above, below, interval), Delta T
Menu controls	Palettes , load custom palletes, auto adjust (manual/continuous/based on histogram equilazation), on screen live and reference image (PoP), image gallery, sequence storage, programmable storage
Alarm Functions	Automatic alarm on any selected measurement function, audible/visible alarm above/below,
Set-up controls	Date/time, Temperature °C/°F, language
Atmospheric transmission correction	Automatic, based on inputs for distance, atmospheric temperature and relative humidity
Optics transmission correction	Automatic, based on signals from internal sensors
Emissivity correction	Variable from 0.01 to 1.0 or select from listings in pre-defined materials list

Reflected ambient temperature correction	Automatic, based on input of reflected temperature
External optics/window correction	Automatic, based on input of optics/window transmission and temperature

Image Storage

Type	Removable SD-card (1 GB) Built-in RAM memory for radiometric real-time sequence storage
File formats – Thermal	Standard JPEG, 14 bit measurement data included
File formats – Visual	Standard JPEG, automaticly associated with corresponding thermal image / possibility for visual marker
Voice annotation of images	30 sec. of digital voice “clip” stored together with the image wired headset;
Text annotation of images	Predefined text selected and stored together with the image

Video Storage

Type	Recording of fully radiometric IR-video clips in camera, transferable to SD-card Recording of MPEG-4 non-radiometric video to SD-card

Video Streaming

Type	Fully radiometric real-time 14-bit digital IR-video using FireWire MPEG-4, IP-link using FireWire or USB

Lenses (Optional)

Field of view/min focus distance	12° x 9° / 0.9m telelens 45° x 34° / 0.1m wide angle lens Close-up 50µm 32 mm x 24 mm / 75 mm
Lens identification	Automatic

Laser Pointer

Classification	Class 2
Type	Semiconductor AlGaInP Diode Laser: 1mW/635 nm red

Battery System

Type	Li-Ion, rechargeable, field replaceable
Operating time	3 hours continuous operation
Charging system	in camera (AC adapter or 12 V from car) or 2 bay intelligent charger
External power operation	AC adapter 110/220 V AC, 50/60 Hz or 12 V from car (cable with Std plug: optional)
Power saving	Automatic shutdown and sleep mode (user selectable)

Environmental Specification

Operating temperature range	-15°C to +50°C
Storage temperature range	-40°C to +70°C
Humidity	Operating and storage 10% to 95%, non-condensing
Encapsulation	IP 54 IEC 529
Shock	Operational: 25G, IEC 68-2-29
Vibration	Operational: 2G, IEC 68-2-6

Physical Characteristics

Weight	1.7 kg incl. battery
Size	120 mm x 145 mm x 220 mm
Tripod mounting	1/4” – 20

Interfaces

FireWire	IEEE-1394 FireWire output (real-time radiometric or non-radiometric video / filetransfer to PC)
USB	Image (thermal and visual), measurement, voice and text transfer to PC
IrDA	Wireless communication
SD-card (2)	I/O slot; storage slot

A.2 FLIR ThermaCAM E65 Infrared Camera

Figure A.2 Views of FLIR ThermaCAM E65 Infrared Camera from different angles (www.bis.fm and www.thermalimages.com.cn)

Imaging Performance

Field of view/min focus distance	Interchangeable; 25° x 19° / 0.3 m, 12° x 9°/1.2m or 45° x 36° / 0.1m
Thermal sensitivity	0.10° C at 30° C
Detector type	Focal plane array (FPA) uncooled vanadium oxide microbolometer, 160x120 pixels, 50/60 Hz
Spectral range	7.5 to 13µm

Image Presentation

Display	2.5” color LCD, 320 x 240 pixels in IR image
Image Controls	Palettes (Iron, Rainbow, B/W, B/W inv), Level, Span, Auto adjust (continuous/ manual)

Measurement

Temperature ranges	-20°C to +250°C (-4°F to +482°F) (standard)
Accuracy (optional)	+250°C to +900°C (+482°F to +1,652°F)
	± 2°C or ± 2% of absolute temperature in °C

Measurement modes	3 movable spots, area max, area min, area average, temp difference, color alarm above or below
Set-up controls	Date/time,Temperature units °C/°F, Language (English, Spanish), Scale, Info field, LCD intensity (high/normal/low)
Measurement corrections	Reflected ambient. Automatic, based on user-input

Image Storage

Digital storage functions	Freeze, Standard Calibrated JPEG images, Delete all images, Delete image, Open
Image storage capacity	Approx. 200 Calibrated JPEG Images with image gallery
Text annotation of images	Predefined text selected and stored together with image

Laser LocatIR TM

Classification	Class 2
Type	Semiconductor A1GaInP Diode Laser: 1mW/635 nm (red)

Power Source

Battery type	Li-Ion; rechargeable, field replaceable
Battery operating time	2 hours. Display shows battery status
Battery charging	In camera (AC adapter or 12V from car) or 2 bay intelligent charger
AC operation	In camera, AC adapter or 12V from car with optional 12V cable. 2 bay intelligent charger included.
Voltage	11-16VDC
Power saving	Automatic shutdown and sleep mode (user-selectable)

Environmental

Operating temperature range	-15°C to +45°C (+5°F to 113°F)
Storage temperature range	-40°C to +70°C (-40°F to 158°F)
Humidity	Operating and storage 20% to 80%, non-condensing, IEC 359

Water and dust resistant (encapsulation)	IP 54, IEC 359
Shock	25G, IEC 68-2-29
Vibration	2G, IEC 68-2-6

Physical Characteristics

Weight	< 1.5 lbs. (0.7 kg) including battery (with standard lens)
Size (L x W x H)	265mm x 80mm x 105mm (10.4"x3.2"x4.1")
Color	Titanium grey
Tripod mounting	Standard, 1/4" - 20
Cover case	Plastic and rubber

Camera includes:
IR camera, ruggedized transport case, power supply and cord, hand strap, lens cap, ThermaCAM® QuickViewTM software, USB cable, video-out cable, user manual, battery (2), 2-bay battery charger, training CD.

Interchangeable lenses (optional)

2X Telescope (12° X 9°/1.2m)
0.5X Wide angle (45° X 34°/0.1m)

Interfaces

IrDA	Two-way data transfer from laptop, PDA

A.3 PUNDIT PLUS PC1006 CNS FARNELL

Figure A.3 View of PUNDIT PLUS PC1006 CNS FARNELL (www.proceq.com) (at the left) and experimental set-up of ultrasonic testing in indirect transmission mode (at the right).

Measurement Ranges	Frequency range: 24kHz to 1MHz
Logging	Pulse rate: 1 to 100 per second, adjustable. Pulse modes: 3 pulse mode (continuous/delay/one-shot). Memory: With continuous and manual modes to store up to 112 readings. Output: RS232C (9 pin serial connector). Data: easily imported into MS Excel for analysis and graph plotting.
Transmitter	Energising pulse: Nominal 1.2kV, 500V or 250V. 1.5μs duration.
Receiver	Bandwidth: 20kHz to 1MHz. Sensitivity: 250μv.
Operating voltages	250V, 500V and 1200V
Display options	Transit time, path length, velocity, limits and elastic modulus
Measurement units	Metric or imperial

Button on receiving transducer	Facilitates manual memory log function
Remote input	Enables Pundit Plus to be controlled by external systems
Downloaded function	Enables stored readings to be transferred to a PC
Oscilloscope Output	Syncronisation pulse: 3.5V positive, rise time 2µs. Signal: True facsimile of receiving transducer output for outputs up to 0.4V.
Display	128 x 128 dot LCD with backlight.
Power Supply	Mains: 100/240V AC input 50/60Hz. 20V DC output. Battery: Internal rechargeable NiMH Batteries 8 x 1.2V / 1.8Ah.
Environmental	Operating Temperature Range: 0°C to 40°C Dimensions: 250 x 160 x 100mm Weight: 2.3kg (electronics unit only) 5.0kg (complete kit)

A.4 VELOCICALC 8346 Anemometer

Figure A.4 View of VELOCICALC 8346 anemometer (www.bis.fm)

Velocity

Range	0 to 30 m/s (0 to 6,000 ft/min)
Accuracy1&2	3.0% of reading or ±0.15 m/s (±3 ft/min) whichever is greater

Temperature

Range	-17.8 to 93.3°C (0 to 200°F)
Resolution	0.1°C (0.1°F)
Accuracy3	±0.3°C (±0.5°F)

Instrument Temperature Range

Operating (Electronics)	5 to 45°C (40 to 113°F)
Operating (Probe)	-17.8 to 93.3°C (0 to 200°F)
Storage	-30 to 90°C (-22 to 194°F)

Volumetric Flowrate

Range4	0.1 to 195,000 l/s, 0.0424 to 702,000 m3/hr, 0.2 to 2,700,000 ft3/min

Duct Size

Range	1 to 100 cm in increments of 0.5 cm, 100 to 255 cm in increments of 1 cm

Averaging Capability

Range	Up to 255 values each of velocity, temperature

Time Constant

Range	Adjustable from 1 to 20 seconds

Response Time

To velocity	200 msec
To temperature	8 seconds

Printer Interface

Type	Serial
Baud Rate	1200

APPENDIX B

SUPPORTIVE *IN-SITU* MEASUREMENTS RELATED TO THE ASSESSMENT OF CRACKS

B.1 Air Velocity Measurements through the Cavity of Cracks

The presence of air flow through the cavity of cracks was measured by using anemometer "VELOCICALC 8364". Recorded V_{AIR} values for a period of 30seconds were given in Figure B.1. The V_{AIR} values were found to be in the range of 0.04m/s and 0.45m/s for the crack at the masonry wall located at the left bottom of window niche. Air flow passing through the cavity of the same crack was measured to be 0.04*l*/s±0.04*l*/s for a period of 30 seconds when the sizes of airflow were accepted to be 1cmx6.5cm in width and length. The V_{AIR} values for the crack following the arch above the window were found varying in the range of 0.67m/s and 1.22m/s. Air flow passing through the cavity of the same crack was measured to be 0.41*l*/s±0.17*l*/s for a period of 30 seconds when the sizes of airflow were accepted to be 1cmx5cm in width and length. No airflow was measured for the other cracks.

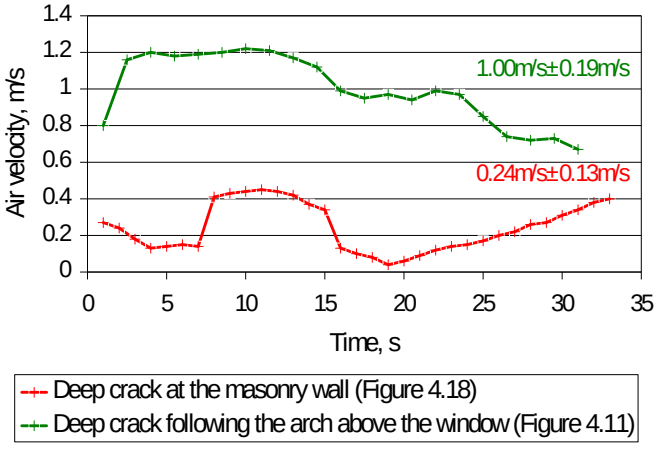

Figure B.1 The V_{AIR} values measured at the cavities of deep cracks at the east side of the structure for a period of 30 seconds, proving the presence of air flow between outside and inside through the cracks.

B.2 The Depth and Width Measurements of Cracks

Table B.1 The depth measurements taken by the vernier calliper for the structural crack at the east wall.

Definition of defect	$\mathbf{D_{CALIPER}}$ mm
Proper adhesion through jointing	-
Non-visible discontinuity through the jointing	-
Deep crack on red tuff block	32.5-75.7
Fracture at jointing	25.8-42.6

$\mathbf{D_{CALIPER}}$: The **D**epth of crack/discontinuity measured by vernier **CALIPER**

Table B.2 The width measurements taken by the vernier calliper for the structural crack at the east wall.

Location of measurement points on the route of crack at the east side of the structure		W_{FIRST} mm	W_{LAST} mm
Crack on red **T**uff at the left bottom of window opening	T1	8.6	8.8
	T2	8.6	9.0
	T3	5.9	6.4
	T4	10.9	11.0
Crack following the **A**rch	A1	3.7	4.5
	A2	3.8	4.3
	A3	5.9	6.7
	A4	6.3	7.2
Crack passing through the **C**eiling of window niche	C1	16.7	17.6
	C2	16.3	17.3

W_{FIRST}: The initial reading for the **W**idth of crack measured by vernier calliper.
W_{LAST}: The last reading for the **W**idth of crack measured by vernier calliper after 27 days.

APPENDIX C

SUPPORTIVE HEAT TRANSFER CALCULATIONS: THERMAL TRANSMITTANCE VALUE, *U*, FOR THE HISTORIC TUFF MASONRY WALL

In this section, thermal transmittance, *U* value for the wall sections at steady state conditions were calculated to estimate the thermal insulation characteristic of tuff masonry wall for Cenabi Ahmet Paşa Camisi.

The calculation was based on basically two configurations ASSUMED for the masonry wall section of Cenabi Ahmet Paşa Camisi. The former one was assumed to be constructed with tuff ashlar stone and mortar while the latter was assumed to be constructed with tuff stone facings at both sides with rubble tuff stone infill. The geometric descriptions of both cases were given in Figure C.1.

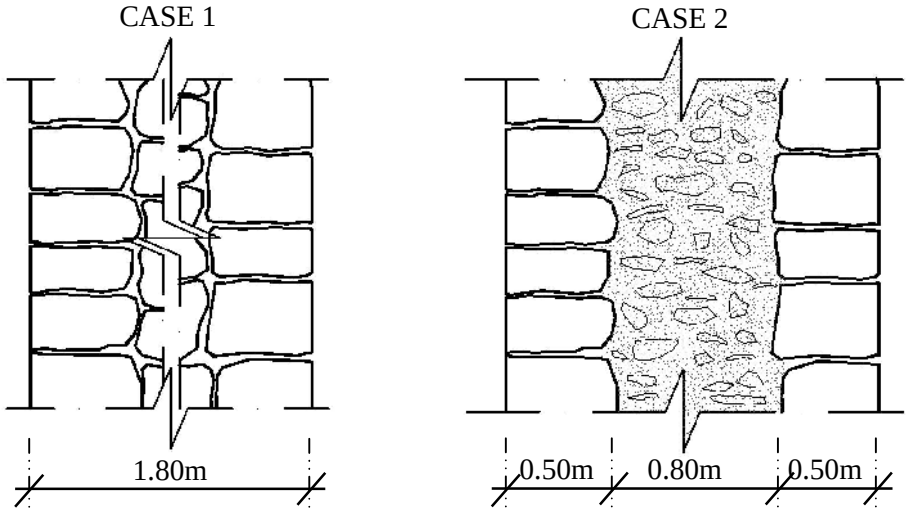

Figure C.1 Geometric description of masonry wall sections ASSUMED for the calculation of overall thermal transmittance, *U* value and overall thermal resistance, *R* value showing the order and thickness of layers for the Case 1 (at the left) and for the Case 2 (at the right).

CASE 1:

Assumption 1 for Case 1:

- Width of wall section, l = 1.80m
- Thermal conductivity of tuff, k_T = 0.73 $Wm^{-1}K^{-1}$ (Erdoğan, 1986)
  Thermal conductivity of mortar, k_M = 0.71 $Wm^{-1}K^{-1}$ (Tavukçuoğlu, *et al*., 2008)
- Thermal conductivity of cut stone tuff wall for the case of 80% tuff and 20% mortar,

$$k = \frac{(0.73 \times 80) + (0.71 \times 20)}{100} = 0.73 \ Wm^{-1}K^{-1}$$

- Inside surface thermal resistance, R_{si} = 0.13 m^2KW^{-1}
- Outside surface thermal resistance, R_{so} = 0.04 m^2KW^{-1}
- Thermal transmittance of tuff wall,

$$U_{TW} = \frac{1}{0.13 + \frac{1.80}{0.73} + 0.04} = 0.34 \, Wm^{-2}K^{-1}$$

Assumption 2 for Case 1:

- Width of wall section, l = 1.80m
- Thermal conductivity of tuff, k_T = 0.40 $Wm^{-1}K^{-1}$ (Özkahraman, *et al*., 2006)
  Thermal conductivity of mortar, k_M = 0.71 $Wm^{-1}K^{-1}$ (Tavukçuoğlu, *et al*., 2008)
- Thermal conductivity of cut stone tuff wall for the case of 80% tuff and 20% mortar,

$$k = \frac{(0.40 \times 80) + (0.71 \times 20)}{100} = 0.46 \ Wm^{-1}K^{-1}$$

- Inside surface thermal resistance, R_{si} = 0.13 m^2KW^{-1}
- Outside surface thermal resistance, R_{so} = 0.04 m^2KW^{-1}
- Thermal transmittance of tuff wall,

$$U_{TW} = \frac{1}{0.13 + \frac{1.80}{0.46} + 0.04} = 0.25 \ Wm^{-2}K^{-1}$$

CASE 2:

Assumption 1 for Case 2:

- Width of wall section, l = 1.80m (0.5m tuff+0.8m rubble stone infill+0.5m tuff),
- Thermal conductivity of tuff, k_T = 0.73 $Wm^{-1}K^{-1}$ (Erdoğan, 1986)
  Thermal conductivity of mortar, k_M = 0.71 $Wm^{-1}K^{-1}$ (Tavukçuoğlu, *et al*., 2008)
- Thermal conductivity of cut stone tuff wall for the case of 80% tuff and 20% mortar,

$$k = \frac{(0.73 \times 80) + (0.71 \times 20)}{100} = 0.73 \ Wm^{-1}K^{-1}$$

- Thermal conductivity of rubble stone infill for the case of 50% tuff and 50% mortar,

$$k = \frac{(0.73 \times 50) + (0.71 \times 50)}{100} = 0.72 \ Wm^{-1}K^{-1}$$

- Inside surface thermal resistance, R_{si} = 0.13 m^2KW^{-1}
- Outside surface thermal resistance, R_{so} = 0.04 m^2KW^{-1}
- Thermal transmittance of tuff wall,

$$U_{TW} = \frac{1}{0.13 + \frac{0.50}{0.73} + \frac{0.80}{0.72} + \frac{0.50}{0.73} + 0.04} = 0.38 \ Wm^{-2}K^{-1}$$

Assumption 2 for Case2:

- Width of wall section, l = 1.80m (0.5m tuff+0.8m rubble stone infill+0.5m tuff),
- Thermal conductivity of tuff, k_T = 0.40 $Wm^{-1}K^{-1}$ (Özkahraman, *et al*., 2006)
  Thermal conductivity of mortar, k_M = 0.71 $Wm^{-1}K^{-1}$ (Tavukçuoğlu, *et al*., 2008)
- Thermal conductivity of cut stone tuff wall for the case of 80% tuff and 20% mortar,

$$k = \frac{(0.40 \times 80) + (0.71 \times 20)}{100} = 0.46 \ Wm^{-1}K^{-1}$$

- Thermal conductivity of rubble stone infill for the case of 50% tuff and 50% mortar,

$$k = \frac{(0.40 \times 50) + (0.71 \times 50)}{100} = 0.56 \ Wm^{-1}K^{-1}$$

- Inside surface thermal resistance, R_{si} = 0.13 m^2KW^{-1}

- Outside surface thermal resistance, R_{so} = 0.04 m^2KW^{-1}
- Thermal transmittance of tuff wall,

$$U_{TW} = \frac{1}{0.13 + \frac{0.50}{0.46} + \frac{0.80}{0.56} + \frac{0.50}{0.46} + 0.04} = 0.26 \ Wm^{-2}K^{-1}$$